2011

The feasibility of a surface-based neutron spectrometer for detecting water on the moon

Andre Souza

THE FEASIBILITY OF A SURFACE-BASED NEUTRON SPECTROMETER FOR DETECTING WATER ON THE MOON

by

ANDRE SOUZA

A THESIS

Submitted in partial fulfillment of the requirements
for the degree of Master of Science
in
The Department of Physics
to
The School of Graduate Studies
of
The University of Alabama in Huntsville

HUNTSVILLE, ALABAMA

2011

In presenting this thesis in partial fulfillment of the requirements for a master's degree from The University of Alabama in Huntsville, I agree that the Library of this University shall make it freely available for inspection. I further agree that permission for extensive copying for scholarly purposes may be granted by my advisor or, in his/her absence, by the Chair of the Department or the Dean of the School of Graduate Studies. It is also understood that due recognition shall be given to me and to The University of Alabama in Huntsville in any scholarly use which may be made of any material in this thesis.

Andre Souza

6/08/2011
(date)

THESIS APPROVAL FORM

Submitted by Andre Souza in partial fulfillment of the requirements for the degree of Master of Science in Physics and accepted on behalf of the Faculty of the School of Graduate Studies by the thesis committee.

We, the undersigned members of the Graduate Faculty of The University of Alabama in Huntsville, certify that we have advised and/or supervised the candidate of the work described in this thesis. We further certify that we have reviewed the thesis manuscript and approve it in partial fulfillment of the requirements for the degree of Master of Science in Physics.

Richard S. Miller	5/24/11 (Date)	Committee Chair
David J. Lawrence	5/24/11 (Date)	
Don A. Gregory	6/9/11 (Date)	
Gary Zank (for Dr. Zank)	6/9/11 (Date)	Department Chair
Jack Fix	6/9/11 (Date)	College Dean
Rhonda Kay Gaede	7/28/11 (Date)	Graduate Dean

ABSTRACT

School of Graduate Studies
The University of Alabama in Huntsville

Degree Master of Science College/Dept. Science/Physics

Name of Candidate Andre Souza

Title The Feasibility of a Surface-Based Neutron Spectrometer for Detecting Water on the Moon

One of the major science and exploration objectives of future lunar studies is to determine the distribution and compositional state of hydrogen on meter-sized spatial scales. This is particularly true for the lunar polar regions where substantial deposits are anticipated within permanently shadowed craters. The morphology of these hydrogen deposits will enable a deeper understanding of the sources of lunar polar volatiles, and provide critical information into transport processes operating at the poles.

Results from multiple missions show strong evidence for hydrogen deposits at the lunar poles. Unfortunately, the lateral distribution information provided by these missions is limited to very large areas (1-10 km^2), with limited knowledge of composition or depth.

A straightforward and robust way to make detailed hydrogen composition and distribution measurements may be via surface-based neutron spectroscopy. This thesis presents a model to address the trends, capabilities, and survey strategies relevant to a surface-based neutron spectrometer.

Abstract Approval: Committee Chair

Dr. Richard S. Miller

Department Chair

Dr. Gary Zank

Graduate Dean

Dr. Rhonda Gaede

ACKNOWLEDGMENTS

First and foremost, I would like to thank my advisor, Dr. Richard Miller. Your guidance throughout the whole research process was invaluable, and it is no exaggeration to say that I could not have finished this work without you. I appreciate everything that you have done for me.

I would also like to thank my committee members, Dr. David Lawrence and Dr. Don Gregory. The advice that both of you have given me was extremely helpful and greatly improved the quality of my thesis. Dr. Lawrence, your inquiries and suggestions, motivated by your expertise in the field, have set me on the right path. Dr. Gregory, I am extremely grateful that I had an optics guru on my committee. I will never forget your consultations.

Jane Stormer and Chantell Marsh deserve a special mention for their help during the final stages of the writing of this work.

Lastly, I would like to thank all of my friends. All of you were also instrumental in keeping me from "burning out" while undergoing the thesis writing process.

TABLE OF CONTENTS

LIST OF FIGURES

FIGURE PAGE

LIST OF TABLES

LIST OF SYMBOLS

SYMBOL	DEFINITION
(x_1, x_2, x_3)	Cartesian coordinates of a point in the crater
(θ, ϕ)	Spherical coordinates of a point in the crater
ϑ_o	Opening Angle
(p_1, p_2, p_3)	Cartesian coordinates of a detector
h	Detector height above surface along the x_3 axis
(x'_1, x'_2, x'_3)	Cartesian coordinates of a point in the detector's field of view
R	The rotation matrix
R_{ij}	The ij component of the rotation matrix
(ϕ_d, θ_d)	Spherical coordinates of a detector's pointing direction with respect to its axis
A_g	The area of the footprint
$\mathcal{S}$	The area bounded by the footprint
A_s	The sampled area of the footprint
N	Number of neutrons "detected"
P	Geometric probability
$\vec{r}$	Vector from the aperture center to the neutron emission point

$\mathcal{A}$	The aperture area
$\vec{n}$	Detector pointing direction vector
Φ	Neutron Flux
n	Number of neutrons
Φ_i	Neutron Flux corresponding to a weight fraction of water
$\mathcal{P}(x, \mu)$	Poisson distribution with mean μ
χ^2_1	Chi-squared distribution with one degree of freedom
λ	Likelihood ratio statistic
T	Time (seconds)
N_i	Number of neutrons "detected" corresponding to a weight fraction of water
N_0	Number of neutrons detected under the null hypothesis
ΔN	Deviation in neutron counts from null hypothesis
T_i	The dwell time of the detector (seconds)
$N_{0,i}$	The number of neutrons expected from the null hypothesis with a that meets the specified threshold criteria for a given weight fraction of water
N_F	Neutrons coming from the field of view
N_B	Neutrons coming from background
ξ	Background neutrons to field of view neutrons ratio

$N_{0,i}^{(\xi)}$	The number of neutrons expected from the null hypothesis with a background of ξ that meets the specified threshold criteria for a given weight fraction of water
$T_i^{(\xi)}$	The amount of time it takes to detect $N_{0,i}^{(\xi)}$ neutrons
$\mathcal{T}_i$	The time ratio
A_{crater}	The area of the crater
τ	The crater survey time
$\mathcal{N}_{model}$	Count rate derived from the model
$\mathcal{N}_{observed}$	The Average LPNS epitherma neutronl count rate
ϵ	The scaling factor
$\mathcal{N}_\epsilon$	The count rate that takes into account the scaling factor
$\mathcal{R}_M$	Approximate radius of the Moon

To my parents

CHAPTER 1

INTRODUCTION

1.1 Motivation

Human beings have been fascinated by the Moon since ancient times. Our closest celestial neighbor has inspired a multitude of questions: Is it possible to live there? What is on the Moon? How similar is it to Earth? Until recently, these questions were nothing more than philosophical quandaries. Now that man has walked on the surface of the Moon and placed several satellites in orbit, questions such as these may finally be addressed with scientific rigor. In particular, the question "What is the distribution of water on the Moon?" still has no definite answer.

A theory for the creation and retention of lunar water may be traced back to the 1960s, where it was suggested that any water in regions of the Moon at temperatures below approximately 120 kelvin would be stable for much of the Moon's lifetime [1]. We now know that such regions exist at the lunar poles in the Permanently Shadowed Regions (PSRs) of craters. Perhaps the best evidence comes from the Diviner instrument on the *Lunar Reconnaissance Orbiter* (Figure 1.1).

Four possible production mechanisms and two major destruction mechanisms for lunar water were identified in another study [2]. The production mechanisms

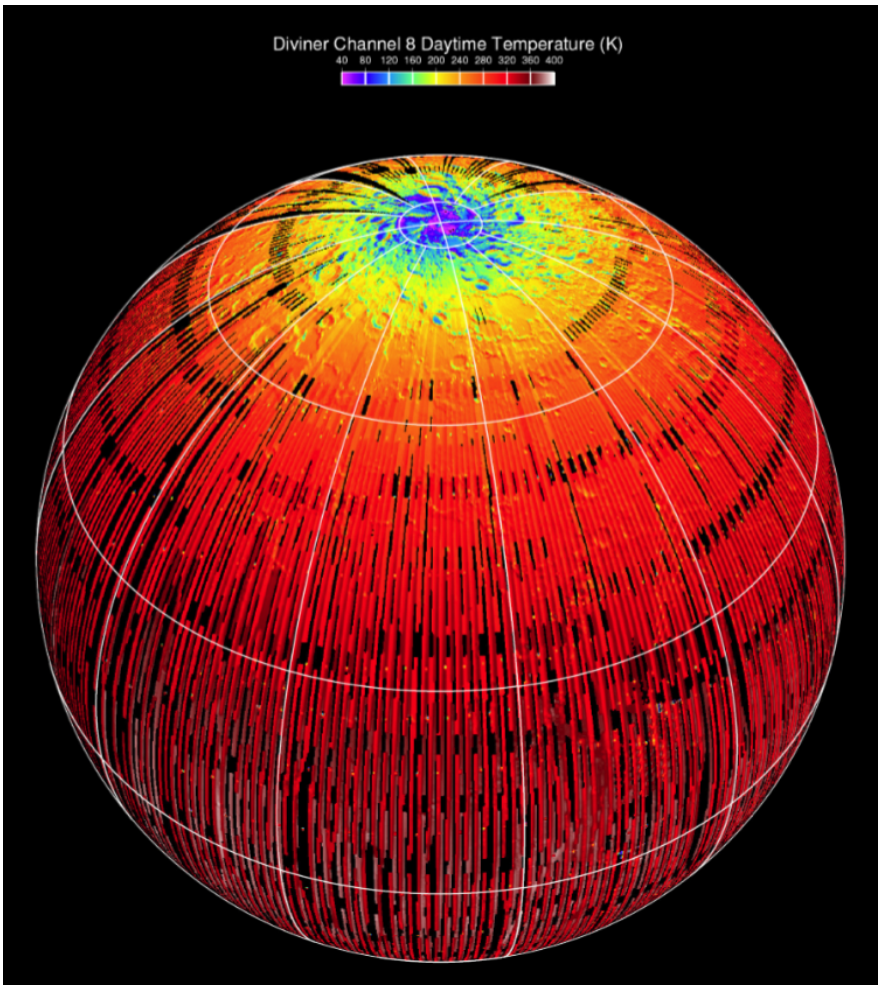

Figure 1.1: Diviner Temperature Map [3].

include 1) solar wind reduction of lunar iron, 2) deposition of water via ice-bearing asteroids, 3) deposition of water via comets, and 4) degassing of the lunar interior. The destruction mechanisms are 1) the photodissociation of water molecules adsorbed on the surface via solar radiation, and 2) the decomposition of trapped water by solar wind particles. If the destruction of water is incomplete an accumulation is possible [2].

Understanding the morphology and abundance of volatiles (such as water) will help answer key questions about the evolution and formation of the solar system itself [4]. The Lunar Exploration Analysis Group (LEAG) has identified several important lunar science goals and among them is the characterization of the lunar geophysical state variables to constrain the origin, composition, and structure of the Moon and other planetary bodies. Another goal is to determine the origin and distribution of endogenous lunar volatiles as one input to understanding the origin, composition, and structure of the Moon and other planetary bodies. Knowledge of the distribution of water fits well within these goals.

There are also practical purposes. If human beings are ever to establish a lunar base, reducing dependence on supplies from Earth would be critical. Since water is a necessity for human survival, lunar water would be the first important step in allowing human beings to "live off the land."

To explore the surface composition of the Moon, neutron spectroscopy may be employed as a remote sensing methodology [5]. It can be used to infer the abundance and distribution of a variety of elements, particularly those with large neutron cross-sections such as hydrogen. Although neutron spectroscopy does not directly measure water, its presence can be inferred from hydrogen abundances.

There are other methods that may be used to determine surface composition as well. Spectroscopic measurements using photons (e.g., infrared, x-ray, gamma-ray) also achieves the desired goal. There are, however, differences in the type of information gathered from each approach. For example, neutron spectroscopy is sensitive to the upper $\sim$ 50 cm of the upper surface layer while infrared photons

probe the upper ~ 2 mm [6]. The use of both photon and neutron spectroscopy would provide complementary information on surface composition. In fact, an integrated approach for mapping surface composition has been shown to be the most effective [4].

The use of orbital neutron spectroscopy to determine lunar hydrogen abundances has been used to great effect, but previous results have been limited to resolutions of ~ 100 kilometer spatial scales because of the uncollimated configuration of the detectors combined with high lunar orbits [7]. A reduction to meter sized resolution would provide better data to answer fundamental science questions, hence provide critical insights to the morphology and abundance of water on the Moon.

One relatively simple way to improve the spatial resolution is to use a surface-based neutron spectrometer. This subject has not been studied previously in any detail and is the focus of this work. The main question that needs to be addressed would be "Is it worth the time, effort, and money to put a surface-based neutron spectrometer on the Moon?". Although this thesis does not answer the question, it provides a basis for future investigations by presenting trends in performance parameters of an idealized spectrometer.

The ultimate goal of a mission with a surface-based neutron spectrometer would be to determine the location, distribution, and abundance of water within PSRs of a crater. For this objective to be achieved several requirement specifications must first be determined. A cost effective way to obtain initial estimates on parameters is to create a mathematical model for a lunar crater and neutron spectrometer and investigate the performance of a detector within a model. To this end, one has been

developed that allows a preliminary investigation of trends. The model is flexible enough to take into account different simple crater geometries and detectors. Different weight compositions of water are assumed and detector count rates are estimated. The model also takes into account background effects and the statistical significance of measurements. The goal of this work is to present trends derived from the model and hence a basis for addressing the feasibility of a surface-based neutron spectrometer.

1.2 Neutron Spectroscopy

An effective way of mapping lunar surface composition is by using neutron spectroscopy [8, 9]. When Galactic Cosmic Rays (GCRs) interact with the lunar soil, knock-on/charge-exchange and spallation/evaporation nuclear reactions produce secondary neutrons [10, 11]. The energies of the nascent neutrons are approximately half of the incident proton in the knock-on case and Maxwellian for the spallation case. As a consequence of these effects, neutrons are removed from their mother atoms and are transported through the regolith, undergoing additional interactions until reaching an equilibrium. Eventually, neutrons are ejected from the surface with a relative consistency [12].

In one study an MCNPX code was used to simulate the flux spectra for various lunar soils [13]. The result for ferroan anorthosite (a type of lunar soil) is shown in Figure 1.2. However, the resulting spectrum of the neutrons leaving the surface also depends on the materials in the upper surface layer. If there is hydrogen present, the neutrons are greatly moderated [9]. Thus, by looking at changes in neutron counts, it is possible to deduce the amount of hydrogen and, its equivalent water abundance

Table 1.1: Neutron Energy Ranges

Thermal	Low-Epithermal	Epithermal	Fast
0 eV $\rightarrow$ 0.4 eV	0.4 eV $\rightarrow$ 10 eV	0.4 eV $\rightarrow$ 500 keV	500 keV $\rightarrow$ onwards

in the regolith, if the hydrogen is in the form of water. How water may change the flux spectra for some particular cases is shown in Figure 1.3.

Neutron energies are traditionally divided into three ranges, in part because of the different experimental techniques used to detect them [14]. The low/medium/high energy neutrons are known as thermal/epithermal/fast neutrons, respectively. Table 1.1 shows the energy range definitions for this work. The low-epithermal range is considered due to performance characteristics of grazing incidence neutron spectrometers [15]. The effective energy range for this kind of spectrometer is the low-epithermal range.

The different energy ranges all have unique origins. Fast neutrons form at high energies when GCRs interact with atoms in the regolith. As the fast neutrons become moderated in the soil, an epithermal spectrum proportional to inverse energy develops. Additional moderation can reduce a neutron's energy to that of the thermal motion of the regolith resulting in a Maxwellian distribution [7].

Neutron energy spectra indicate the composition of elements in the upper surface layer of the Moon [16]. Variations in thermal neutron counts may be used to infer an abundance of neutron absorbing nuclei such as iron, potassium, gadolinium, titanium, and samarium. Epithermal variations are indicative of hydrogen abun-

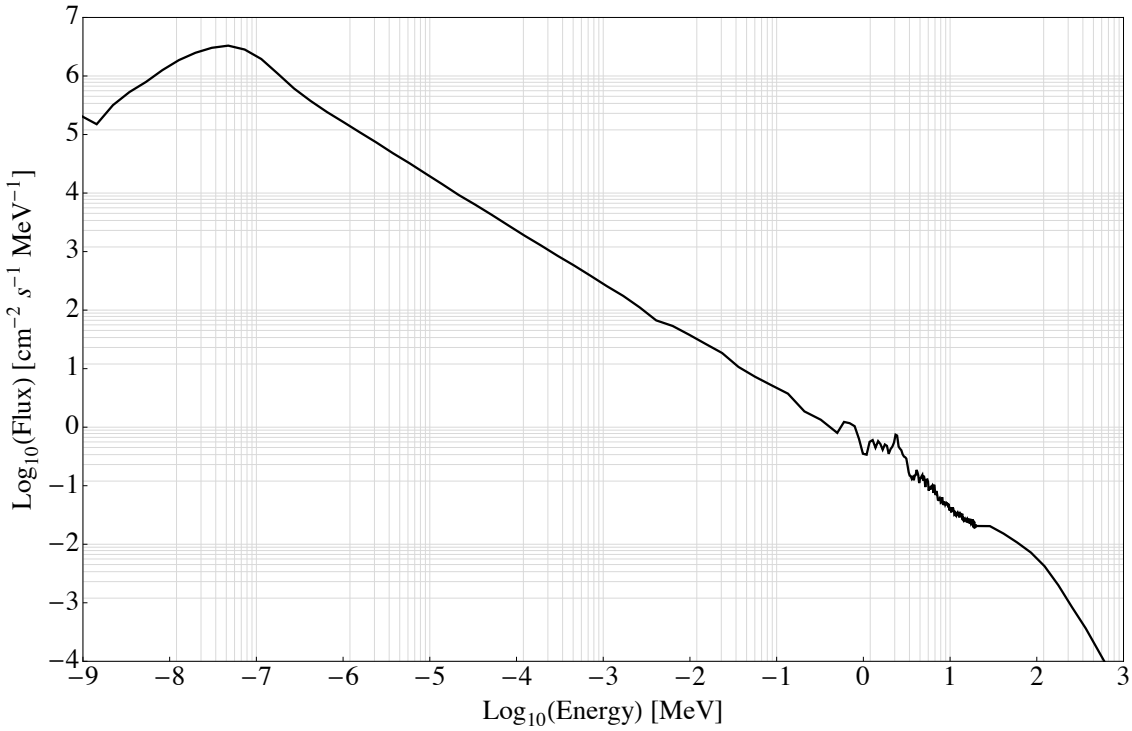

Figure 1.2: Flux Spectra for Neutrons in Dry Regolith [13].

dances.[1] Fast neutron variations are primarily used to provide information on iron and titanium abundances. Epithermal neutrons are the most sensitive to hydrogen abundances, although fast and thermal neutrons can also be used. One difference however, is that thermal neutron fluxes do not scale monotonically with increasing hydrogen abundances while fast and epithermal neutron fluxes do scale in such a manner [7]. This effect may be seen in the simulated neutron flux spectra for ferroan anorthosite (Figure 1.3). For lower energies the dotted (5% weight fraction of water) curve is above the solid (0% weight fraction of water) curve.

[1]By implication, this can also mean water abundances.

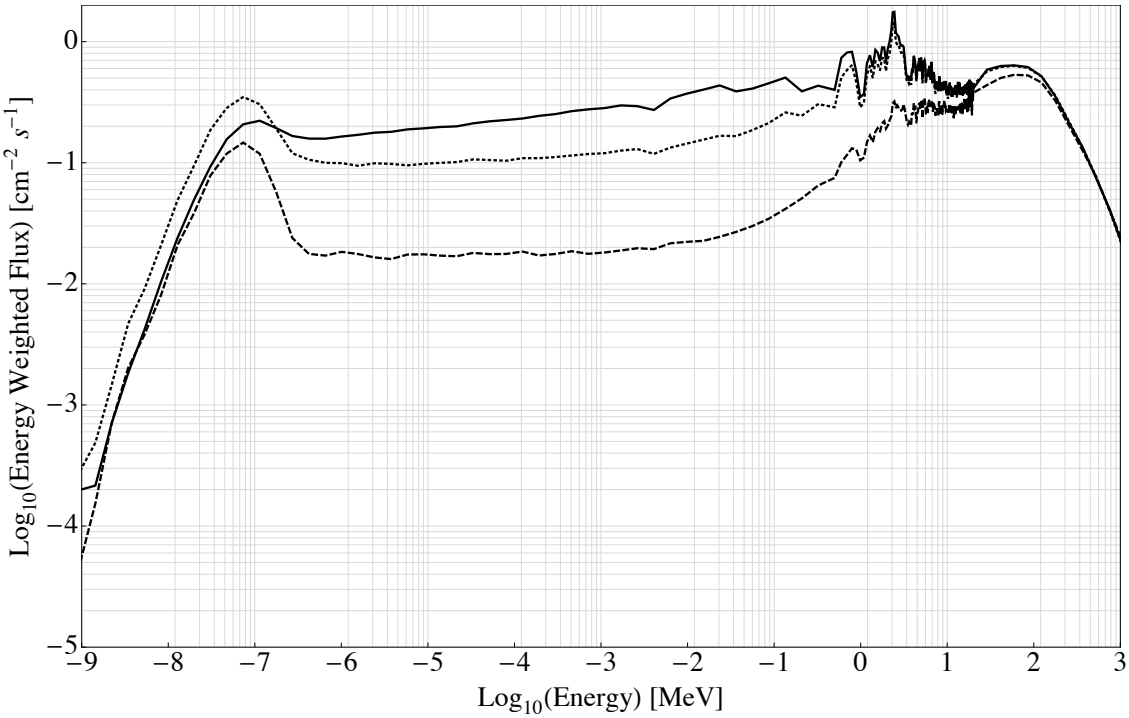

Figure 1.3: Energy Weighted Neutron Flux Spectra for Different Water Contents. [The solid, dotted, and dashed curves correspond to 0%, 5%, and 100% weight fractions of water, respectively [13].]

1.3 Evidence for Lunar Water

The evidence for lunar water deposits comes from a variety of missions using complementary techniques including 1) radar echoes, 2) neutron spectroscopy, and 3) infrared spectroscopy. All of the measurements were made from orbit, allowing the entire Moon to be examined. Table 1.2 summarizes the missions, instruments, and related techniques relevant to lunar water detection.

Table 1.2: Missions and Techniques

Mission	Instrument(s)	Technique
Clementine	Radio Antenna	Radar
Lunar Prospector	NS	Neutron Spectroscopy
	GRS	Neutron Spectroscopy
Chandraayan-1	M^3	Infrared Spectroscopy
LCROSS	NSP1	Infrared Spectroscopy
LRO	LEND	Neutron Spectroscopy

1.3.1 Clementine

Clementine was launched on January 25, 1994. The purpose of the mission was to test the effects of extended space exposure on new spacecraft components, as well as making observations of the Moon and asteroid 1620 Geographos. Unfortunately, due to a malfunction, *Clementine* was not able to collect any data on Geographos. It was, however, able to make several important observations of the Moon: The discovery of permanently shadowed regions (PSRs) at the lunar southern pole was one result [17]. *Clementine* returned over 1 million images of the Moon as well as data indicative of lunar water presence.

1.3.1.1 Relevant Mission Results

A device dedicated to the search for lunar water was not part of *Clementine*'s payload; however, an improvised method allowed for such an investigation. The bistatic radar experiment used *Clementine*'s transmitter to emit radio waves toward various locations on the Moon. The signal was aimed at permanently shadowed regions of the Moon and other locations for comparison. The signal was an unmod-

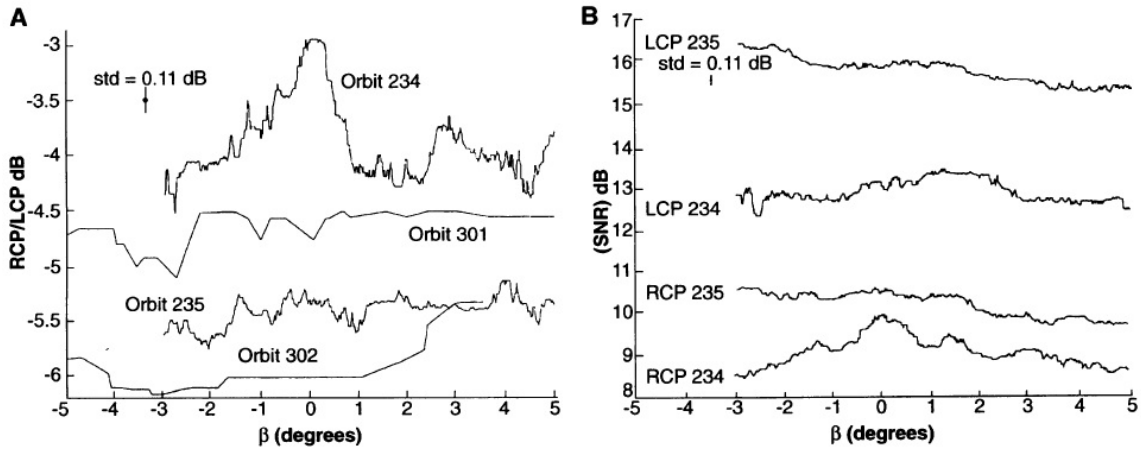

Figure 1.4: Bistatic Radar Data. [The graph on the left is the circular polarization ratio (RCP/LCP) as a function of beta angle for orbits 234, 235, 301, and 302. The graph on the right is the individual polarization channels RCP and LCP echo power response used on a frequency bin-by-bin basis to compute the ratios in orbits 234 and 235 [17].]

ulated S-band 2.273 GHz with right circular polarization, a net power of 6 watts, and was transmitted with *Clementine*'s 1.1 meter antenna. The radar echoes were received on Earth by one of the Deep Space Network's (DSN) 70-meter antennas, and the magnitude and polarization of radar echoes were analyzed [17].

Polarization enhancement in the reflected radio waves is indicative of water presence [18]. Figure 1.4 shows an apparent polarization enhancement in Orbit 234 in the vicinity of the beta angle[2] zero. Since this corresponded to a PSR in the lunar southern pole, it supported the belief that water may be located in PSRs. A later study reexamined the *Clementine* data and was unable to reproduce the previous results [19].

[2]The beta angle is the angle between the orbit plane and the direction to the sun.

1.3.2 Lunar Prospector

The *Lunar Prospector* (*LP*) mission was launched in January 1998 with several objectives. It was designed to investigate the Moon by mapping surface composition from a low orbit, make measurements of the Moon's magnetic and gravitational fields, and to study outgassing events.

1.3.2.1 Neutron Spectrometers

Two Helium-3 sensors with energy counters were used to detect thermal and epithermal neutrons on *LP* (Figure 1.5). The spectrometers (LPNS) had a diameter of 5.7 cm, were 20 cm long, and were pressurized to 10 atm. Although the geometry for both spectrometers was the same, one was covered by a 0.63 mm thick sheet of cadmium and the other in a 0.63 mm sheet of tin [7]. Due to the large cross-section of cadmium to thermal neutrons, the cadmium covered sensor was mostly sensitive to neutrons above 0.4 eV which implies that it was sensitive only to epithermal neutrons.

Because the detectors were uncollimated, they had a spatial resolution of approximately 100 km. The spatial resolution changed depending on the height of the spectrometer above the lunar surface and was calculated using a mix of geometry and statistics [20].

1.3.2.2 Gamma-Ray Spectrometer

While LPNS measured thermal and epithermal neutrons, its Gamma-Ray Spectrometer (GRS), with an anti-coincidence shield (ACS), detected moderated and

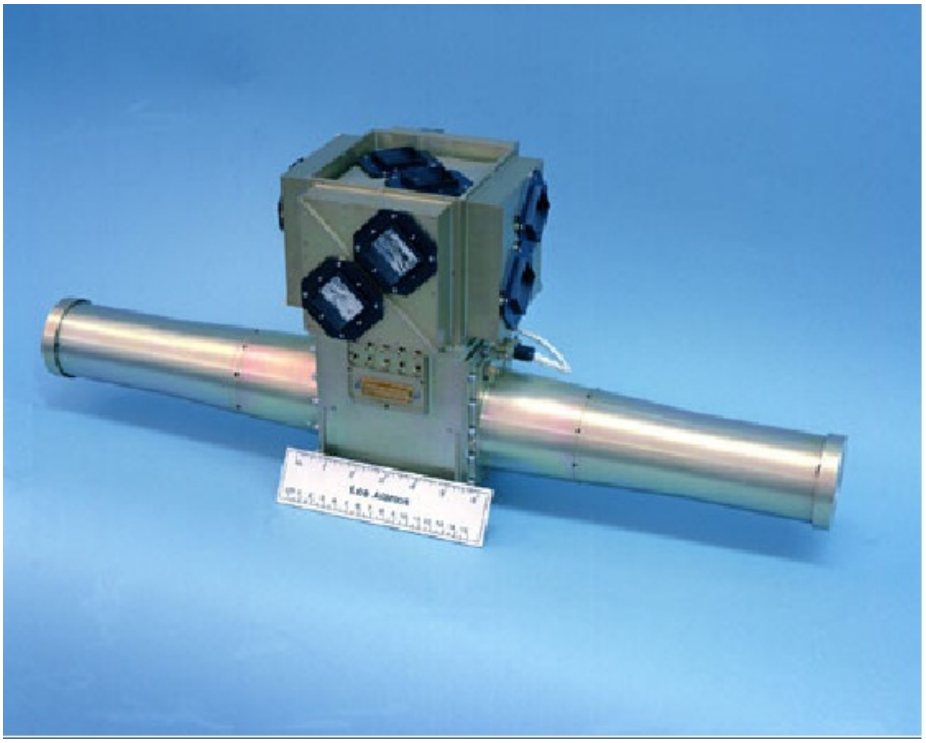

Figure 1.5: *Lunar Prospector* Neutron Spectrometers [21].

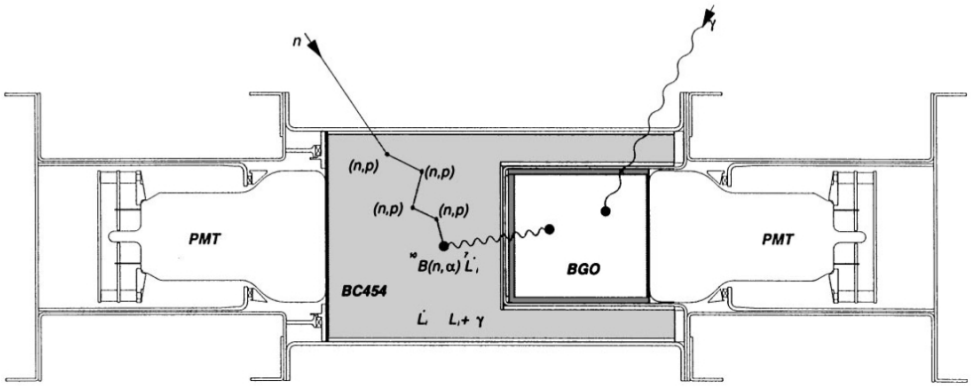

Figure 1.6: *Lunar Prospector* Gamma-Ray Spectrometer [22].

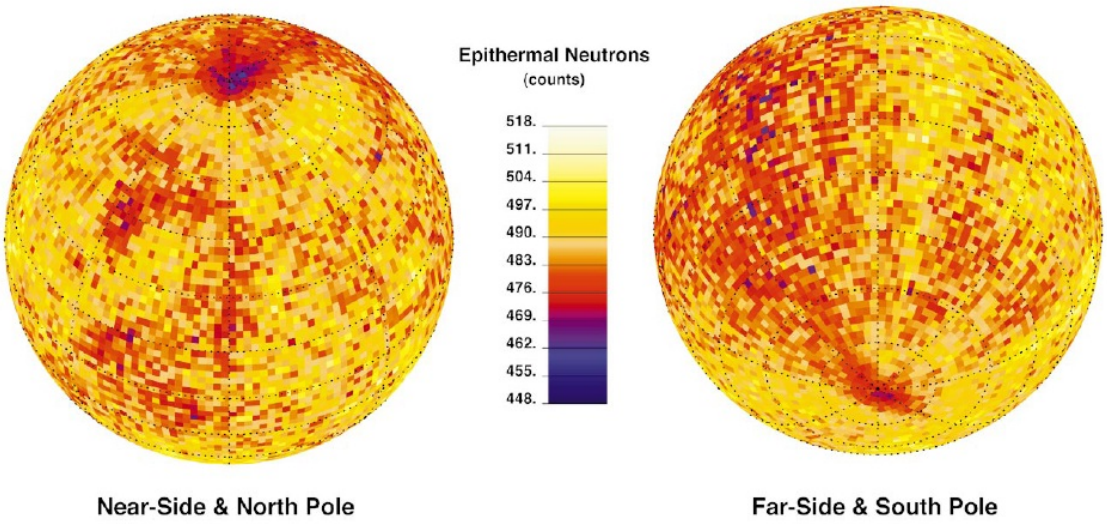

Figure 1.7: Epithermal Count Lunar Mapping. [Epithermal neutron counts over 32 seconds measured by *LP*'s cadmium covered helium-3 proportional counter [7].]

fast neutrons[3] [22]. The GRS was a bismuth-germanate (BGO) crystal cylinder with a 7.1 cm diameter and a height of 7.6 cm. It was sensitive to gamma rays with energies in the range 500 keV to 9 MeV. Surrounding the GRS was an ACS (a borated plastic scintillator) with external dimensions of 12 cm diameter and 20 cm height [22]. A schematic of the GRS is shown in Figure 1.6.

The neutrons were detected using both the ACS and the BGO. If a detection of the $^{10}B(n,\alpha)$ is observed in the ACS followed by coincidence 478 keV gamma-ray detection in the BGO, then a neutron was detected. Further conditions needed to be checked to discriminate between fast or moderated neutrons [23].

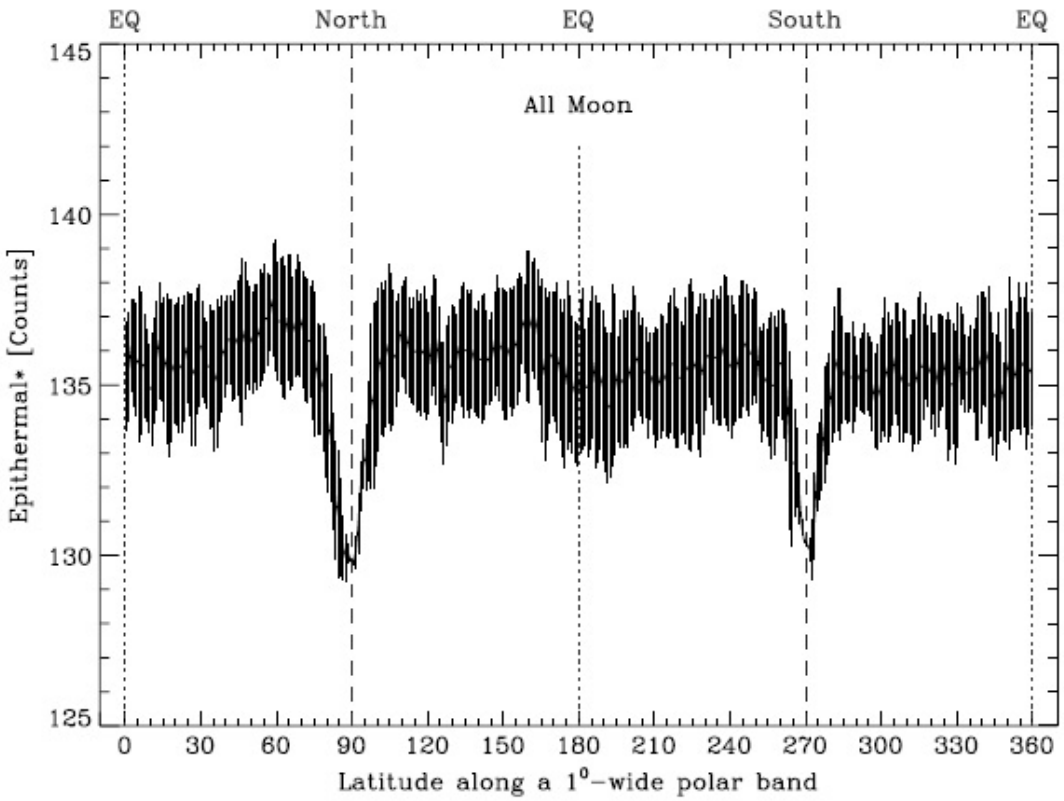

Figure 1.8: Neutron Counts Measured by *Lunar Prospector*. [The error bars are the standard deviation of epithermal neutron counts. [7].]

1.3.2.3 Relevant Mission Results

LP orbited the Moon and measured neutron counts, providing a mapping of the lunar surface as shown in Figure 1.7. The figure shows epithermal counts averaged over 32 seconds for different parts of the Moon. Similarly, Figure 1.8 shows the same information but from a different perspective. The main advantage of Figure 1.8 is that a drop in neutron counts can clearly be seen in the vicinity of the lunar poles. Although drops in epithermal counts are indicative of hydrogen, it may be attributable to other elements. Subsequent analysis concluded that the primary cause of the drop

[3]Moderated neutrons are neutrons with energies between 0 eV and 500 keV.

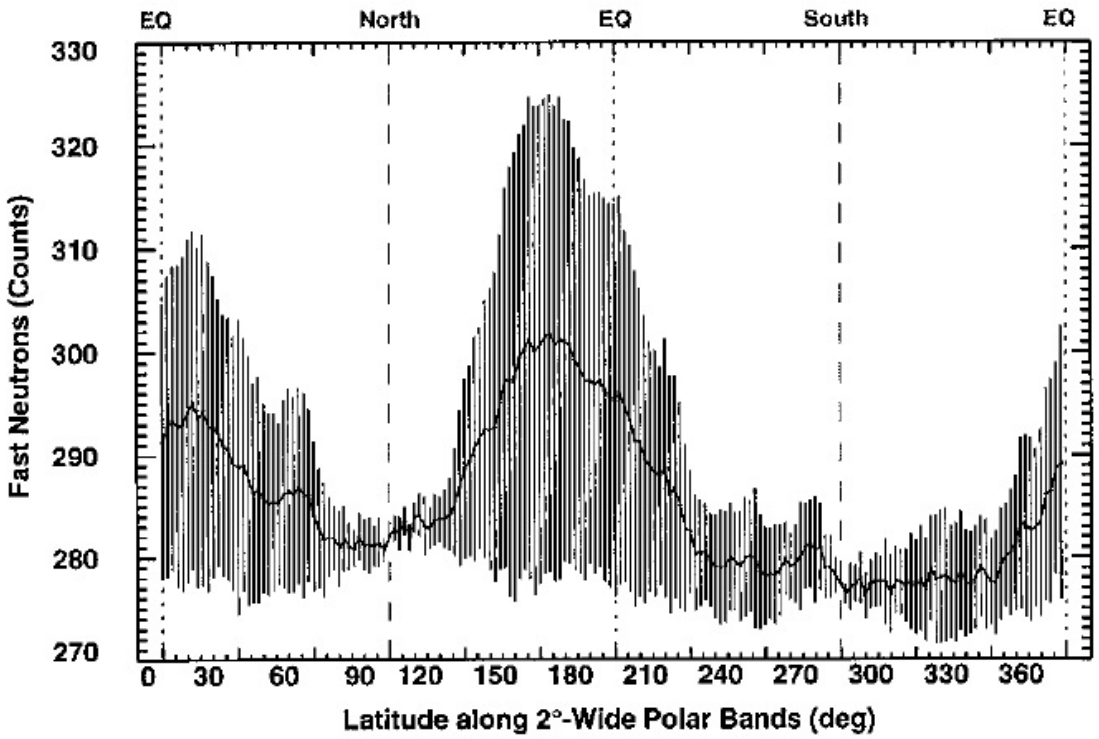

Figure 1.9: Fast Neutron Counts measured by *Lunar Prospector*. [The error bars are the standard deviation of fast neutron counts. [7].]

may be identified with hydrogen, possibly in the form of water [13]. The argument for a water based origin was further strengthened with another study which concluded that hydrogen deposited by the solar wind was not sufficient to produce the changes observed by *LP* [24].

Using the GRS, fast neutrons could also be mapped. The fast neutron counts are shown in Figure 1.9. In comparison to the epithermal counts, no appreciable deficit consistent with the epithermal counts is seen in the polar regions of the Moon. It is possible, however, to establish an upper limit for fast neutron deficit in this region [7]. When this limit is applied, the fast neutron deficit is a tenth of the epithermal count deficit. Although different, the count rates for both epithermal and

fast neutrons were consistent with theoretical expectations for pure water ice deposits [7].

1.3.3 Chandraayan-1

The Indian satellite *Chandraayan-1* was launched in October 2008. The goal of the mission was to map the Moon's topography and chemical characteristics as well as mark the initiation of India's space program. The spacecraft was equipped with instruments to detect photons in the infrared, visible, and X-ray regimes with very good resolution (energy and spatial). Although its mission was supposed to last 2 years, the instrument lasted only 312 days. *Chandraayan-1* was still able to meet most of its mission objectives.

1.3.3.1 Moon Mineralogy Mapper

The Moon Mineralogy Mapper (M^3) instrument onboard *Chandraayan-1* was a state of the art spectrometer that measured light in the visible and near-infrared range. This instrument was critical to the mapping of the surface composition of the Moon because the solar radiation re-radiated from the Moon contains information about the elements on the lunar surface up to a depth of about 2 mm [6].

The instrument had a sensitivity to photons with wavelengths in the range of 430 nanometers to 3000 nanometers (0.43 to 3 microns) and had a 10 nm spectral resolution. The spatial resolution was also good: At an altitude of 100 kilometers above the surface it could resolve features as small as 70 meters in diameter [25].

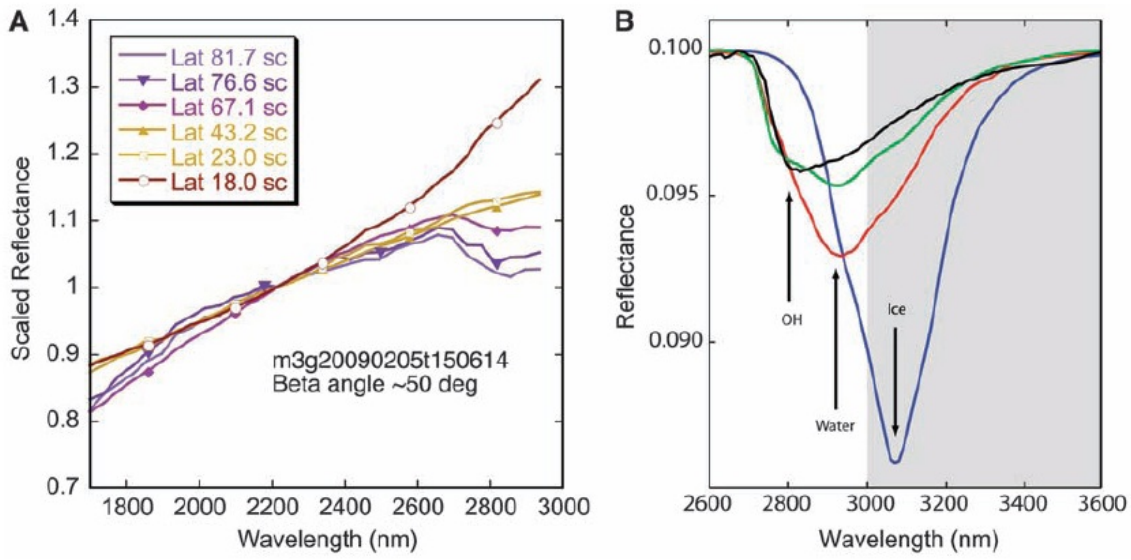

Figure 1.10: Reflectance and Scaled Reflectance. [The image on the left is the scaled reflectance spectra for M^3 image strip M3G200902005T- 150614 with no thermal emission removed. The spectra are 7 by 7 pixel averages. The image on the right is a model near-infrared reflectance spectra for water and hydroxyl. These spectra are highly dependent on physical state [6].]

1.3.3.2 Relevant Mission Results

Among the many important results of the *Chandrayaan-1* mission, was the discovery of water across the lunar surface. This was not, however, unambiguously determined. The spectra for water, ice, and hydroxyl overlap with each other (Figure 1.10B), making it difficult to distinguish between them. The M^3 instrument on *Chandrayaan-1* detected an absorption feature characteristic of water/hydroxyl over the entire lunar surface. However, absorption characteristics were stronger toward the lunar poles. The relative absorption increased monotonically with latitude (Figure 1.10 and Figure 1.11).

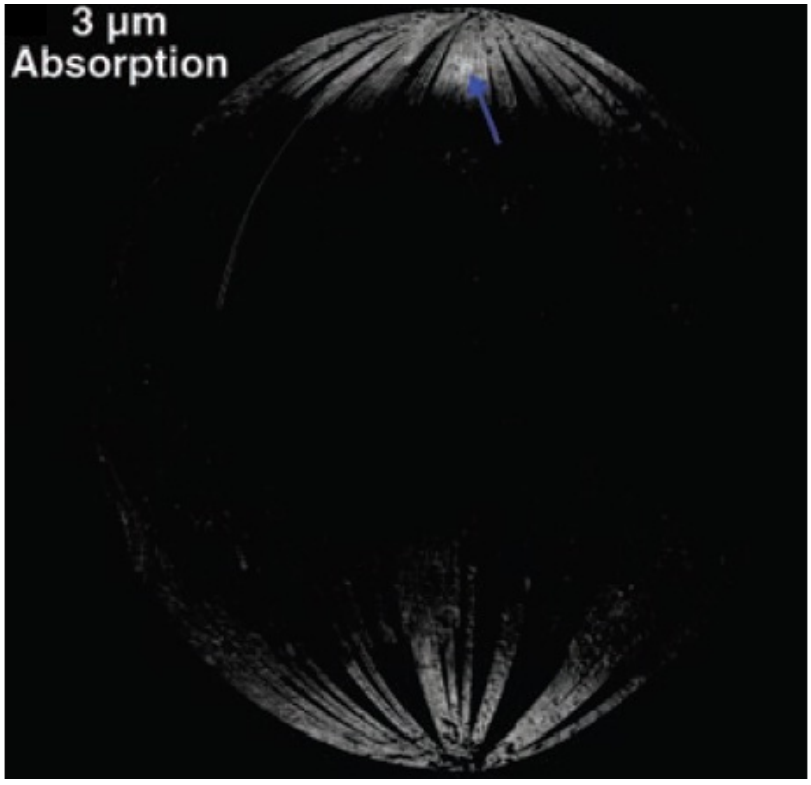

Figure 1.11: Three Micrometer Optical Absorbance. [The brighter areas indicate stronger $3 - \mu m$ absorption [6].]

Since both the M^3 instrument on *Chandrayaan-1* and the neutron spectrometer of *LP* are able to infer hydrogen abundances, the results may directly be compared to one another. In particular, the inferred hydrogen abundances over the Goldschmidt crater was compared to previous neutron spectroscopy measurements by *LP*. Since this crater has a diameter of over 113 kilometers, it was within *LP*'s spatial resolution. In comparison to the rest of the lunar pole, the *LP* neutron spectrometer experienced a relative maximum in neutron counts [26]. On the other hand, the *Chandraayan-1* M^3 instrument detected a relatively strong absorption feature in this region. This suggests that the hydrogen abundance detected by *LP* was only in the upper few

millimeters of regolith, since neutron spectroscopy maps composition of elements at a greater depth. However, this result is not conclusive [26].

With regard to the rest of the Moon, there was a lack of correlation with previous neutron spectrometry data, suggesting that the creation and retention of water and hydroxyl is not a static but an ongoing process. This leads to the belief that the Moon may have a water cycle [6].

1.3.4 LCROSS

The *Lunar CRater Observation Sensing Satellite* (*LCROSS*) spacecraft was launched with the *Lunar Reconnaissance Orbiter* (*LRO*) on an Atlas V rocket on June 18, 2009. One of the objectives of the *LCROSS* mission was to independently investigate the presence of water within PSRs at the Moon's southern pole [27]. To achieve this objective, the launch vehicle's upper stage (a Centaur) was crashed into the southern lunar crater Cabeus (October 9, 2009), knocking the regolith into the sunlight so that its absorption spectra could be analyzed by *LCROSS* [28]. The Cabeus crater was chosen for two primary reasons: (1) Its orientation to the sun and (2) hydrogen abundances inferred from *LP* and *LRO* data.

1.3.4.1 Relevant Mission Results

After *LRO* separated from *LCROSS* and the Centaur, the *LCROSS* shepherding spacecraft took control over the Centaur for the next 4 months. To reduce water contamination originating from the spacecraft, maneuvers were performed to expose the spacecraft to the Sun. An hour before the Centaur's impact *LCROSS*'s

instruments were activated and began taking measurements. Before the impact there were no water absorption features detected [27].

After Centaur crashed, a 1000 kelvin vapor cloud was detected followed by low and high angle ejecta. The spectral evolution of the crash suggested that there was an initial release of vapors and ice-rich ejecta that quickly passed out of the field of view of the instrument during the first 20 seconds, followed by a emergence of subliming ice-grains. This interpretation was supported by the increase in the 1.86 μm water vapor absorbance after impact.

The amount of water in the dust plume was evaluated to be approximately 5.6%$\pm$2.9 by weight fraction of water [27]. Assuming that Cabeus is not substantially different from other lunar craters, this suggests that a high fraction of the hydrogen measured by *LP* and *LRO* was in the form of water. It must, however, be noted that the ejecta plume sample may have contained a greater depth of regolith than the amount that neutron spectroscopy can measure. Thus, the answers are not expected to be completely consistent with one another.

Aside from the direct measurements of water absorption features, there is also indirect evidence from hydroxyl absorption lines. Hydroxyl may have been created from the photo-dissociation of water vapor or desorption of hydroxyl from grains. The hydroxyl feature is evident in the ratio of post-impact scans to a pre-impact reference. Before impact no hydroxyl band was detected [27].

1.3.5 LRO

The *LRO* was launched along with *LCROSS* on June 18, 2009. This mission serves as a precursor to future manned explorations on the Moon. Specifically, the *LRO* mission aims to identify safe landing sites, find useable materials, and characterize the radiation environment.

1.3.5.1 Lunar Exploration Neutron Detector

The Lunar Exploration Neutron Detector (LEND) instrument onboard *LRO* was designed to create a high resolution map of the lunar surface, characterize the surface distribution and column density of water at PSRs, and characterize global neutron space radiation [29]. LEND consists of four Helium-3 neutron spectrometers surround by a boron collimator. This allows it to achieve a claimed 10 kilometer spatial resolution from an orbit of about 50 kilometers. This is not, however, a universally accepted conclusion. An alternative study esimates that the resolution may be an order of magnitude poorer [30].

1.3.5.2 Relevant Mission Results

Initial data from the LEND instrument only associates a statistically significant drop in neutron counts with permanently shadowed regions for two craters: Shoemaker and Cabeus [31]. The neutron count measurements over the other seven craters considered in the study were not statistically significant; thus, the measurements could not provide any direct evidence of neutron suppression. The data does, however, allow for a conservative estimate. It seems to indicate that there could be

neutron suppression coming from regions that are not permanently shadowed. This implies that a more complex model may be needed to describe the volatile retention process.

As stated previously, data from the LEND instrument was used to select a proper site for the *LCROSS* mission. A relative neutron suppression 0.875 ± 0.023 was observed over the Cabeus, a good indicator of a relative increase in hydrogen content [31].

1.4 Summary of Missions

There have been several independent studies using satellites that validate the presence of lunar water. The *Clementine* bistatic radar experiment was the first among these and, using radio waves, detected polarization enhancement indicative of water in PSRs. To complement the results of the *Clementine* mission, neutron spectrometers on *LP* and *LRO* have both detected drops in neutron count rates at the lunar poles. Further studies with the *LP* data showed that this may be attributed to water in PSRs. To complement the results from neutron spectroscopy, *Chandraayan-1* detected an absorption characteristic of water/hydroxyl throughout the lunar surface with its M^3 instrument, and identified a possible dynamic water environment on the Moon. The *LCROSS* mission made a definitive detection of water within a single crater.

CHAPTER 2

MODEL GEOMETRY AND TRENDS

2.1 Introduction

An examination of detector tradeoffs and optimal search strategies is paramount in constructing the most suitable detector. An ideal detector (and search scenario) is one that minimizes the required exposure, provides good (meter scale) resolution, and can easily distinguish between different weight fractions of water. A mathematical model has been developed in this investigation to estimate detector performance. This model uses a combination of crater geometry, detector performance characteristics, neutron fluxes and spectra, to estimate the neutron signatures relevant to the search for lunar water.

A program has been created to numerically obtain the desired parameters because an analytic solution to the equations of the model are not easily easily obtained. The program is flexible and a powerful tool of investigation. Estimates of neutron count rates for different weight fractions of water may be obtained by varying geometric and detector parameters. Furthermore, a likelihood approach is used to determine the significance of neutron counts. Table 2.1 summarizes the simulation parameters.

Table 2.1: Simulation Parameters

Simulation Parameters	Symbol	Units	Type	Section
Crater Diameter and Depth	a, b, c	m	Input	Section 2.2
Detector Aperture Area	$\mathcal{A}$	m^2	Input	Section 2.3
Detector Opening Angle	ϑ_o	-	Input	Section 2.3
Detector Position	p_i	m	Input	Section 2.3
Detector Pointing Direction	$\vec{n}$ or (θ_d, ϕ_d)	-	Input	Section 2.3
Footprint Area and Geometry	A_g and $\mathcal{S}$	m^2	Output	Section 2.4
Sampled Area	A_s	m^2	Output	Section 2.10
Neutron Counts	N	-	Output	Section 3.1
Confidence Level	-	-	Input	Section 3.2
Significance	-	-	Output	Section 3.2
Neutron Energy Range	-	eV	Input	Section 3.3
Weight Fraction of Water	-	-	Input	Section 3.3
Neutron Flux	Φ_i	$m^{-2}s^{-1}$	Output	Section 3.3
Dwell Time	T	s	Output	Section 3.5
Background Ratio	ξ	-	Input	Section 3.6
Crater Survey Time	τ	s	Output	Section 3.8

2.2 Crater Geometry

A generic ellipsoid is used to describe the shape of a crater. Although this neglects the finer details of a crater, it describes the gross geometric features. In Cartesian coordinates an ellipsoid is given by the equation

$$x_3 = -c\sqrt{1 - \left(\frac{x_1}{a}\right)^2 - \left(\frac{x_2}{b}\right)^2}. \tag{2.1}$$

The parameter c is a measure of the depth of the crater and a, b describe the width in the x_1 and x_2 directions, respectively. For the work presented here

$a = b = 2.5$ kilometers and $c = 500$ meters. The key elements of this feasibility study

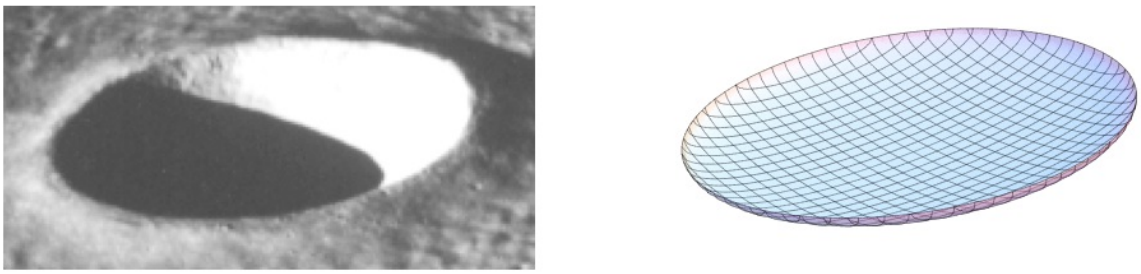

Figure 2.1: Lunar Crater and Crater Model. [The image on the left is the Moltke Crater and the image on the right is the ellipsoidal model given by Equation 2.1.]

are not directly affected by this choice. As shown in Figure 2.1, the ellipsoid geometry is a reasonable description of a "typical" lunar crater.

Spatial information is central to the feasibility study, thereby requiring positions within the crater to be identified. Cartesian coordinates are one option; however, it is convenient to parametrize the ellipsoid in spherical polar coordinates (θ, ϕ), where

$$\begin{aligned} x_1 &= a\sin(\theta)\cos(\phi) \\ x_2 &= b\sin(\theta)\sin(\phi) \\ x_3 &= c\cos(\theta) \end{aligned} \tag{2.2}$$

and (θ, ϕ) are the polar and azimuthal angles [32]. The domains of these parameters are shown in Table 2.2, along with the crater coordinate in Figure 2.2 and Figure 2.3. One advantage of using spherical polar coordinates over cartesian coordinates is the scale independence of the coordinate system.

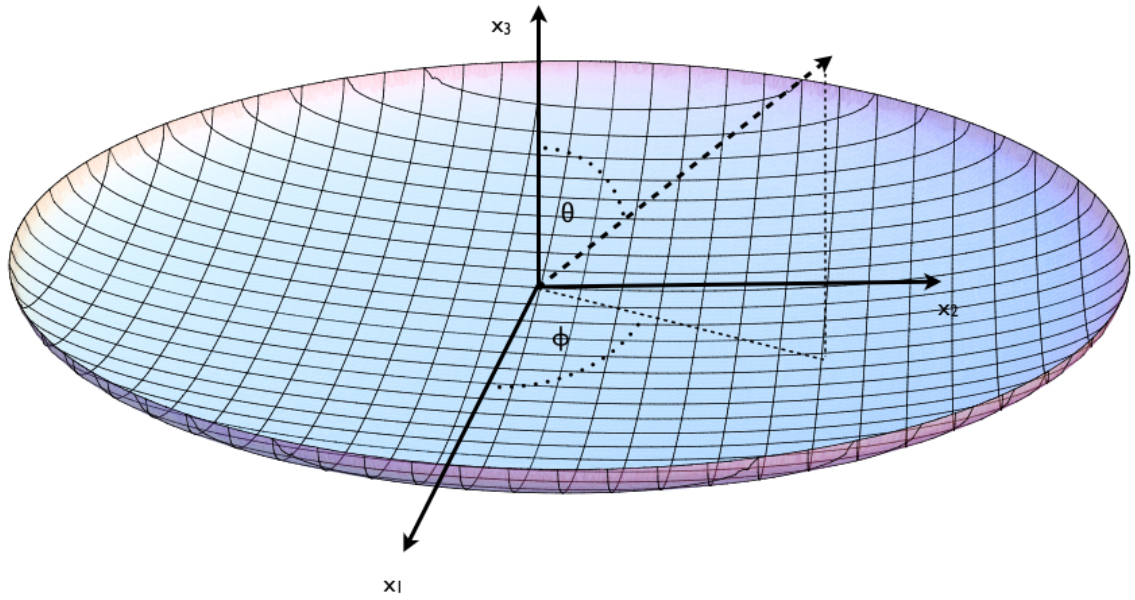

Figure 2.2: The Crater Geometry. [The origin of the coordinate system is defined as c meters above the crater center. The polar and azimuthal angles have their usual meanings in spherical coordinates.]

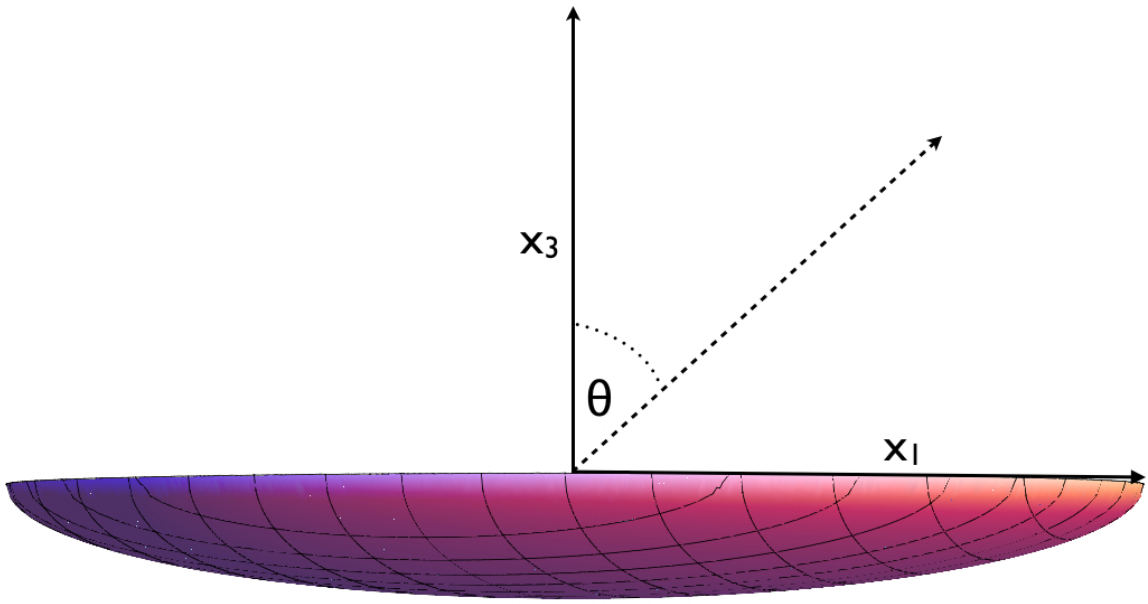

Figure 2.3: Side View of the Crater Model.

Table 2.2: Polar and Azimuthal Angle Domain

	θ	ϕ
Name	Polar Angle	Azimuthal Angle
Domain	$[90°, 180°]$	$[0°, 360°)$

2.3 Detector Geometry

A generic detector model is used in order to keep the treatment general. Detector efficiencies will be neglected; hence, the detection process considered here solely consists of the neutron transport to the telescope aperture. This approach is used because detector efficiencies are highly dependent on the specific detector implementation, and the goal of this work is only to evaluate the feasibility of a surface-based approach.

The detector's position within the crater may be specified by (p_1, p_2, p_3) in Cartesian coordinates or by the angles (θ_p, ϕ_p) and its height h above the crater floor. Using Equation 2.2, the detector's position is then

$$\begin{aligned} p_1 &= a\sin(\theta_p)\cos(\phi_p) \\ p_2 &= b\sin(\theta_p)\sin(\phi_p) \\ p_3 &= c\cos(\theta_p) + h. \end{aligned} \tag{2.3}$$

This is a particulary convenient description of detector position if detector height is assumed to remain constant.

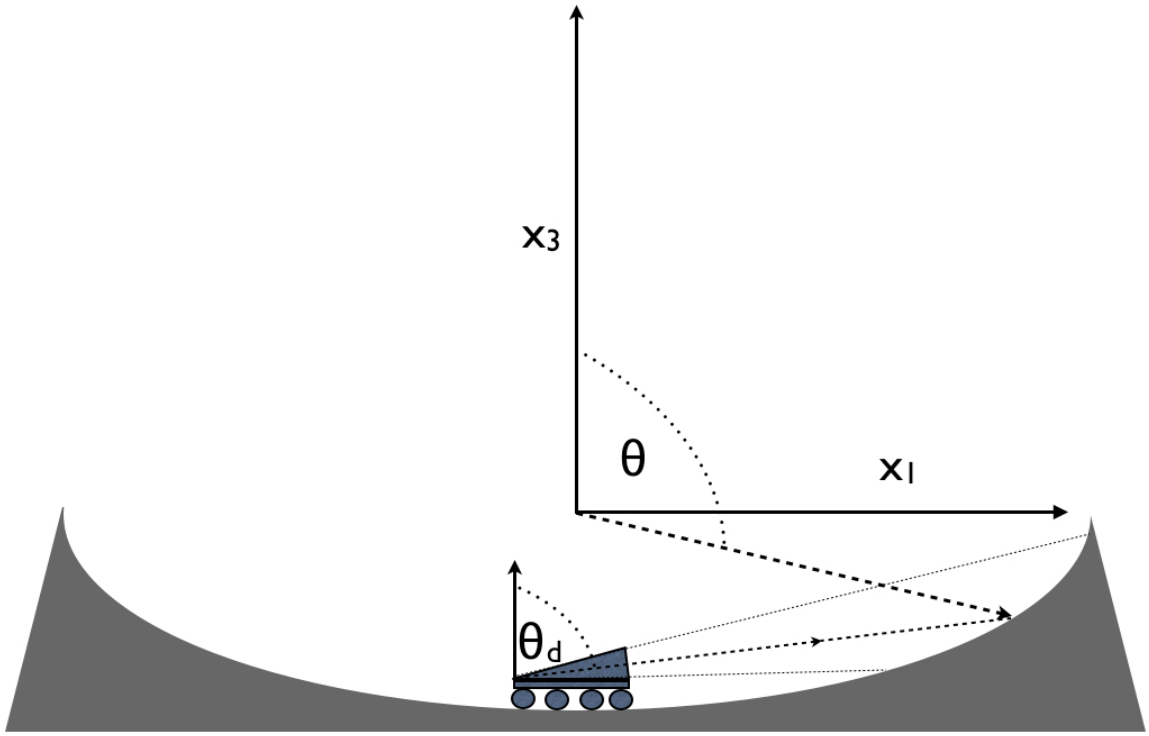

Figure 2.4: Crater Geometry with a Detector.

The detector is assumed to have a limited field-of-view, rather than being omni-directional. Thus knowledge of its pointing direction is critical. The pointing direction vector $\vec{n}$ is defined to be normal to the aperture:

$$\vec{n} = \sin(\theta_d)\cos(\phi_d)\hat{x}_1 + \sin(\theta_d)\sin(\phi_d)\hat{x}_2 + \cos(\theta_d)\hat{x}_3, \tag{2.4}$$

where (θ_d, ϕ_d) are the polar and azimuthal angles with respect to a coordinate system centered at the detector. The relationship between this coordinate system and the crater coordinate system is just a simple translation.

Although (θ_d, ϕ_d) may be used to describe which direction the detector is looking, it is more convenient to measure everything with respect to the crater coordinate system (Figure 2.4). To solve for the angles (θ_d, ϕ_d) in terms of a crater location, the cartesian components (x_1, x_2, x_3) of (θ, ϕ) must be found using Equation 2.2. From geometric considerations, the relationship between (θ_d, ϕ_d) and (x_1, x_2, x_3) is

$$\begin{aligned} \theta_d &= \arccos\left(\frac{x_3 - p_3}{\sqrt{(x_1 - p_1)^2 + (x_2 - p_2)^2 + (x_3 - p_3)^2}}\right) \\ \phi_d &= \arctan\left(\frac{x_2 - p_2}{x_1 - p_1}\right) \end{aligned} \tag{2.5}$$

and are derived from the standard coordinate transformation from cartesian to spherical coordinates.

2.4 Field-of-View and Footprint

For this work, the field-of-view (FoV) is the observed shape of a region in three-dimensional space. In the case of a collimated detector with a circular aperture, the FoV would be a cone defined by its opening angle ϑ_o (Figure 2.5). The equation for a point (x_1', x_2', x_3') within the FoV of such a telescope is

$$x_3' \geq \sqrt{\frac{(x_1')^2 + (x_2')^2}{\tan^2(\vartheta_o)}} \tag{2.6}$$

for the case where the detector is located at the origin and looking straight up (Figure 2.6).

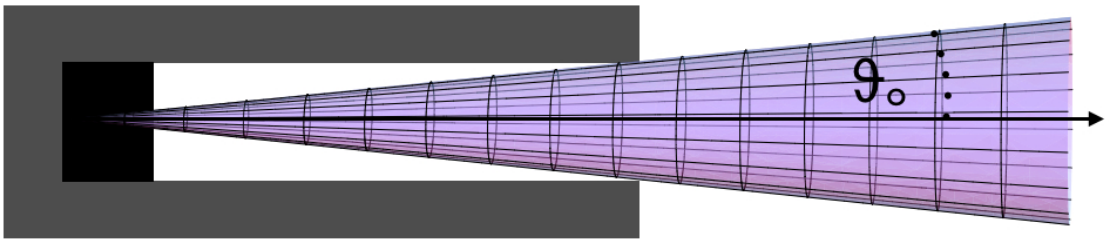

Figure 2.5: Detector and Field of View. [The FoV of a detector with a circular aperture is conical.]

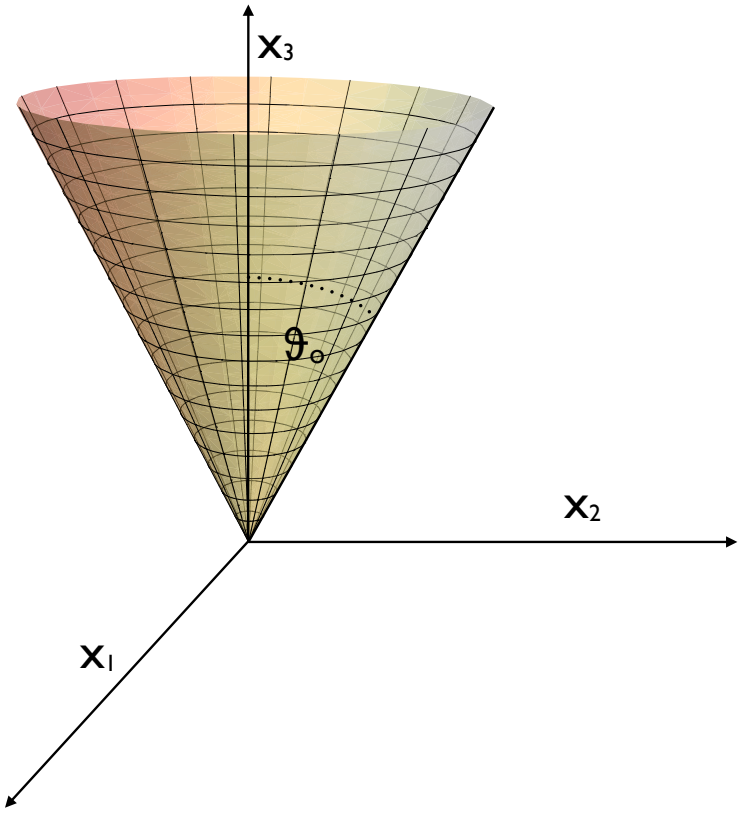

Figure 2.6: Field of View. [The FoV of a detector looking upwards with a circular aperture and opening angle ϑ_o is shown.]

In this work the intersection of the FoV with the crater surface is relevant since it defines the observable surface area. This intersection is defined to be the footprint of the detector and is denoted by the symbol $\mathcal{S}$. The FoV terminates on this surface of intersection. For example, a detector pointing straight down toward a flat surface would have a circular footprint. If the detector is tilted at an angle while looking at a flat surface, then the shape would be an ellipse. For an ellipsoid, the footprint is not a simple conic section except for the simplest of scenarios (a detector located at the origin of a sphere); thus, the shape of the footprint is evaluated numerically.

2.5 Calculation of Footprint Outline

One method of finding the footprint of a detector at an arbitrary location and pointing direction within a crater is to use rotations and translations of Equation 2.6 to solve for the surface of intersection with the crater ellipsoid (Equation 2.1).

If the FoV is contained completely within the crater it is not necessary to identify all points that satisfy Equation 2.6. Instead, only the surface is required. Thus the inequality of Equation 2.6 may be taken to be an equality and x_3' may be eliminated as a dependent variable.

In general it is not possible to write the equation of the rotated and translated cone as a function of x_3'. This can be most easily imagined by rotating the cone by 90° toward the x_1'-x_2' plane. In this case there are two x_3' for every (x_1', x_2'). So, instead of finding an explicit functional form, a point that satisfies equality in Equation 2.6 is manipulated to obtain the condition necessary for lying on the footprint outline.

Let (x'_1, x'_2, x'_3) represent a point on the cone (Equation 2.6) and (x_1, x_2, x_3) represent a point on the crater. A rotation matrix (derived in Appendix A) R_{ij} denotes the ij components of a 3D rotation matrix R that orients the cone to the appropriate pointing direction, and p_i $(i = 1, 2, 3)$ denote the position of the detector in cartesian components. Using this notation, the equation that takes a point within the FoV and places it in the proper location would be

$$\sum_{j=1}^{3} R_{ij} x'_j + p_i = x_i. \tag{2.7}$$

In the crater all (x_1, x_2, x_3) satisfy Equation 2.1. Setting the x_i of Equation 2.7 equal to the ellipsoidal components (Equation 2.1), yields the equation

$$\sum_{j=1}^{3} R_{3j} x'_j + p_3 = -c\sqrt{1 - \left(\frac{\sum_{j=1}^{3} R_{1j} x'_j + p_1}{a}\right)^2 - \left(\frac{\sum_{j=1}^{3} R_{2j} x'_j + p_2}{b}\right)^2}. \tag{2.8}$$

Since x'_3 is dependent[1] on x'_1 and x'_2, this equation is of the form

$$f(x'_1, x'_2) = 0. \tag{2.9}$$

This function represents the outline of the detector footprint. Solving for the x'_1 and x'_2 that satisfy this equation and using Equation 2.7 gives the (x_1, x_2, x_3) coordinates of the footprint outline.

[1]The x'_3 is determined by equality in Equation 2.6.

2.6 Geometric Area

There are two primary reasons to calculate the geometric area of the footprint. The first is to determine the spatial resolution of the detector and the second is to estimate the number of particles being emitted from the surface given a specific flux.

To calculate the number of particles being emitted from the footprint, it is necessary to integrate the flux over the footprint area. However, if the flux is assumed to be uniform and steady, this calculation may be simplified: The number of particles emitted is simply obtained by multiplying the flux by the geometric area A_g.

The geometric area of the projected field of view is computed using a double integral over the footprint surface $\mathcal{S}$ bounded by the outline defined by Equation 2.9. The equation for the surface area is

$$A_g = \iint_{\mathcal{S}} \sqrt{1 + \left(\frac{\partial x_3}{\partial x_1}\right)^2 + \left(\frac{\partial x_3}{\partial x_2}\right)^2}\, \mathrm{d}x_1\, \mathrm{d}x_2, \tag{2.10}$$

where x_3 is given by Equation 2.1. This integral cannot, in general, be evaluated analytically due to the complicated shape of $\mathcal{S}$; therefore, it is solved numerically.

2.7 Calculation of Geometric Area

To calculate the geometric area of the footprint, a numerical scheme was created. The integral in Equation 2.10 was approximated by a Riemann sum. The x_1 were divided into β bins by finding the minimum x_1 (x) and maximum x_1 (X) in the footprint outline. Within each bin, the minimum x_2 (y) and maximum x_2 (Y) were

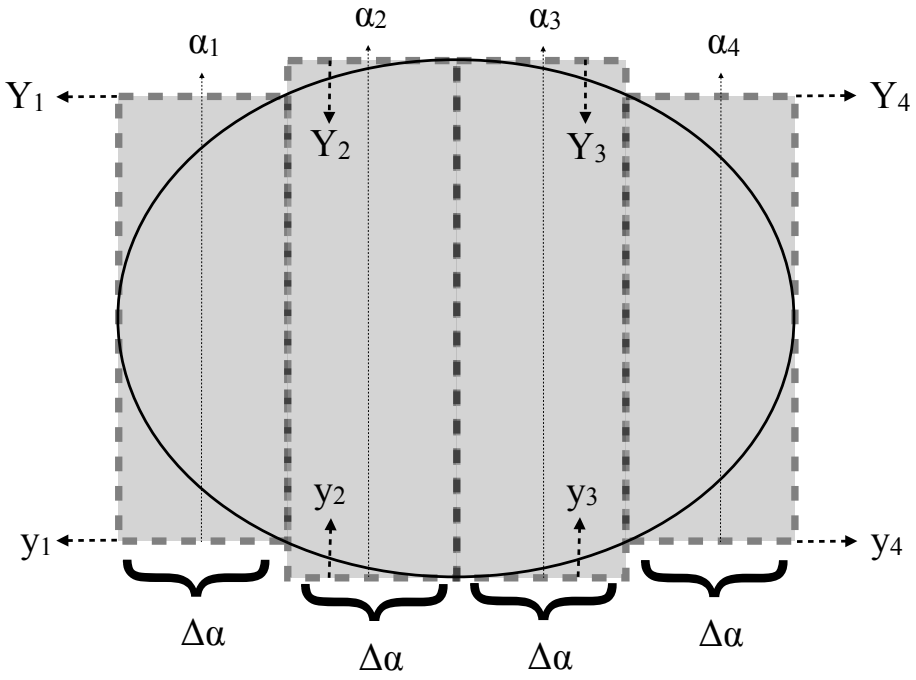

Figure 2.7: Geometric Area Approximation. [For $\beta = 4$ an approximation to the area of the above figure may be made. From the figure it is clear that this will overestimate the area of the shape.]

then found. Using the following substitutions,

$$\Delta\alpha = \frac{X - x}{\beta} \tag{2.11}$$

$$\alpha_j = x + (j - 1/2)\Delta\alpha \tag{2.12}$$

$$Y_j = Y \text{ in the domain } [x + (j-1)\Delta\alpha, x + j\Delta\alpha] \tag{2.13}$$

$$y_j = y \text{ in the domain } [x + (j-1)\Delta\alpha, x + j\Delta\alpha]. \tag{2.14}$$

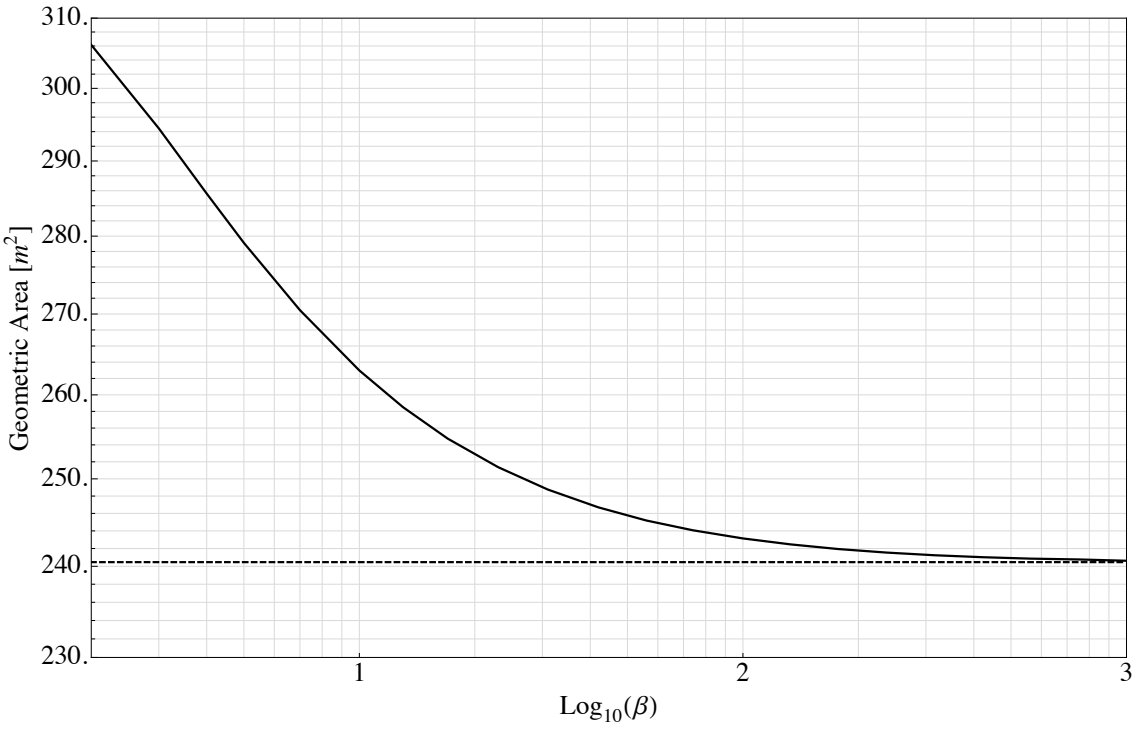

Figure 2.8: Geometric Area Convergence. [For a detector with an opening angle of 5° located 100 meters above the crater center and looking downwards, the geometric area calculation converges as beta increases. The dashed line is the exact value of the geometric area.]

Equation 2.10 is approximated by the Riemann sum

$$A_g \approx \sum_{j=1}^{\beta} \Delta\alpha \int_{y_j}^{Y_j} \sqrt{1 + \left(\frac{\partial x_3}{\partial x_1}\right)^2 \Bigg|_{\alpha_j} + \left(\frac{\partial x_3}{\partial x_2}\right)^2} \, \mathrm{d}x_2. \tag{2.15}$$

This process is shown graphically in Figure 2.7. It should be noted that this procedure will overestimate the geometric area. If β sufficiently large, however, Equation 2.15 is a good approximation. Figure 2.8 shows the convergence for a particular test case.

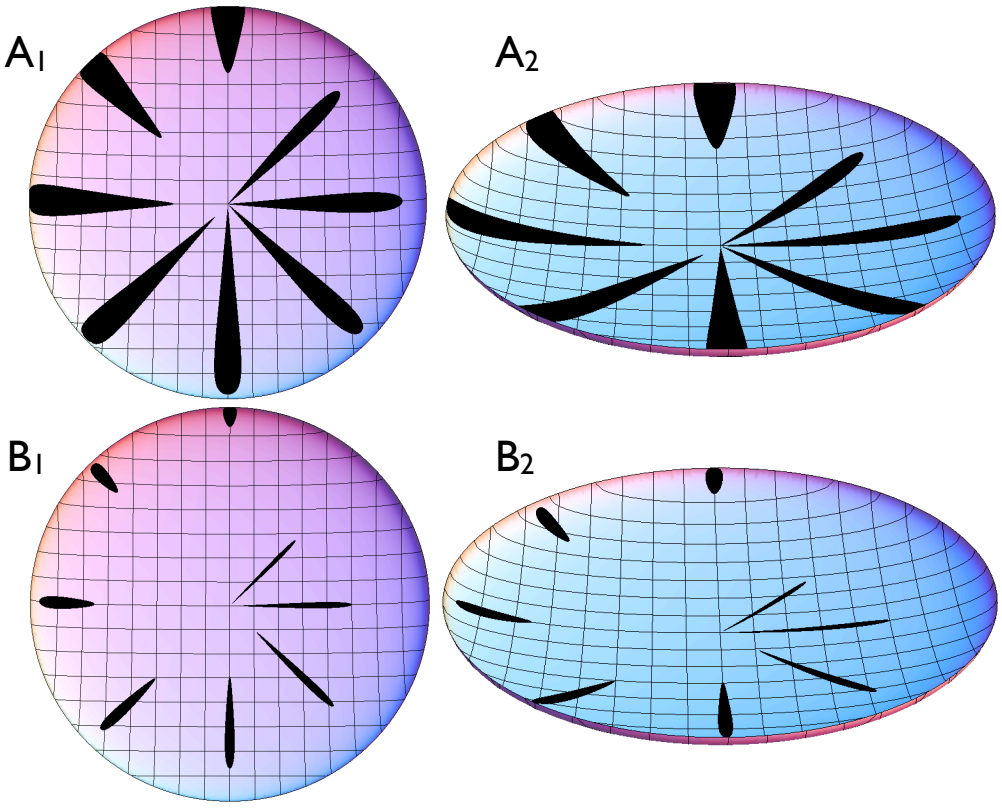

Figure 2.9: Footprint Shapes. [These are the footprints for a detector located one meter above the crater center. The A figures are footprints for an opening angle of 5 degrees while the B is for 2 degrees. The rightward graphs are the same as the ones on the left but from a different perspective. From the northern footprint shape, proceeding counter-clockwise, the detector is pointed towards the polar angles 100° to 170° in 10° increments.]

2.8 Pointing Direction, Geometric Area, and Opening Angle Trends

Using the scheme described in previous sections, it is possible to compute the shape and geometric area of the footprint for various scenarios.[2] In particular, Figure 2.9 displays the resulting footprint shapes for two different telescope opening angles and different pointing directions (Figure 2.4 is a guide to how θ is related to

[2]The parameter β was taken to be 400 for these computations.

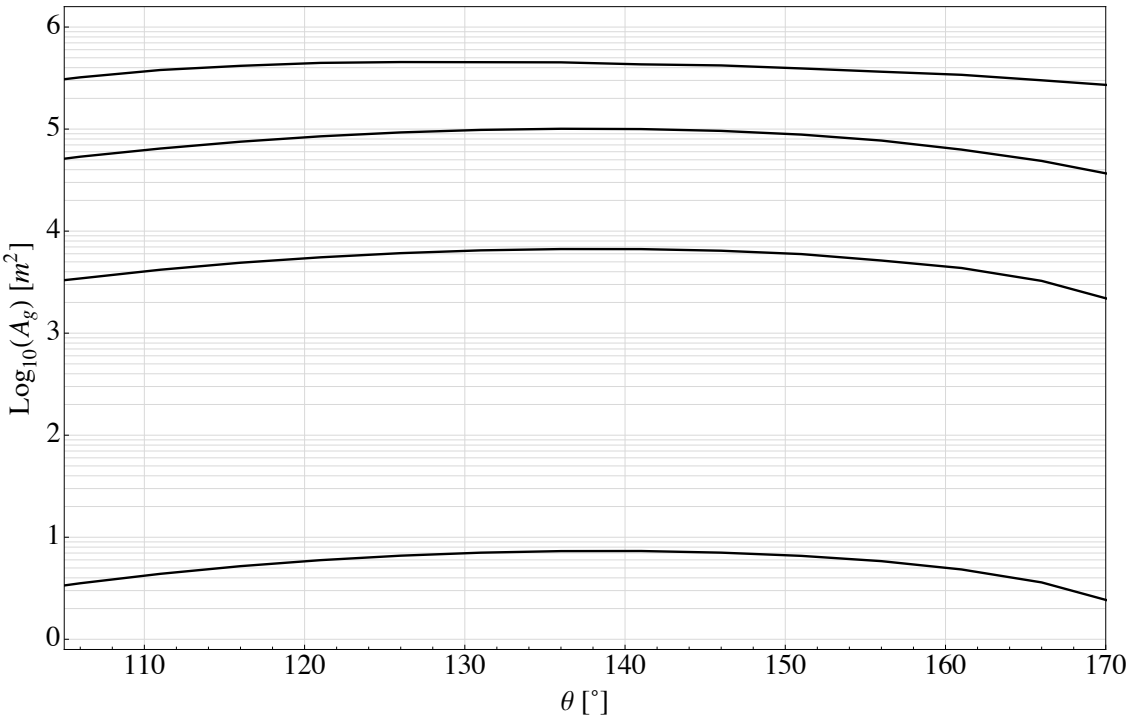

Figure 2.10: Polar Angle, Geometric Area, and Opening Angle Trends. [The above figure is the geometric area of a footprint for a detector one meter above the crater center as a function of the polar angle. From bottom to top the lines correspond to opening angles of $1/60, 1/2, 2, 5$ degrees.]

where the detector is looking). The geometric area for two additional opening angles as a function of the polar angle is shown in Figure 2.10.

The prominent feature in these graphs is that the geometric area has a local maximum. This can be understood by examining the footprints in Figure 2.9. As the pointing direction moves from the crater edge towards the center of the crater, the field of view becomes completely contained within the crater and the footprint spreads out across the flat part of the surface, thus increasing the area. However, as

it continues in this direction, the area decreases because the footprint gets closer to the detector.

Even though the geometric area of the footprint varies by an order of magnitude with pointing direction, the effect is relatively small when compared to changes produced by the detector's opening angle. The modifications to the opening angle produce changes that span several orders of magnitude. As expected a smaller opening angle produces a much smaller footprint, hence better resolution, while a larger opening angle produces a bigger footprint area.

2.9 Geometric Probability

The number of particles emitted from within the FoV of the detector could be calculated by multiplying the geometric area of the footprint by the flux. Unfortunately, not all of these particles will reach the aperture. An emitted neutron must be on an appropriate trajectory to pass through the aperture, and there is an associated probability P for this event to occur. The explicit form of P is derived in Appendix B, but some simplifying assumptions are made to obtain a more reasonable expression.

To illustrate the elements required to calculate this, a 2D case is outlined. In 2D the detector aperture would be represented as a line segment of length L. To calculate the probability that a particle passes through the aperture, two assumptions are made: particles have an isotropic distribution and ray-like trajectories. The assumption of an isotropic distribution has the consequence that the probability P of a particle being emitted between an angle ϑ_1 and ϑ_2 is $P = \frac{1}{\pi}\int_{\vartheta_1}^{\vartheta_2} \mathrm{d}\theta$. The variables

ϑ_1 and ϑ_2 are measured with respect to the surface normal. The normalization is taken to be π because the particles leave the surface between $-\frac{\pi}{2}$ and $\frac{\pi}{2}$ radians.

The necessary geometry is illustrated in Figure 2.11. Assume that a particle is being emitted within the field of view of the detector from the point $(0, 0)$ on a flat surface. Also, let (x, y) be the aperture point closest to the particle and $(x + \delta x, y + \delta y)$ be the farthest. Then, the angles ϑ_1 and ϑ_2 are $\vartheta_1 = \arctan\left(\frac{x}{y}\right)$ and $\vartheta_2 = \arctan\left(\frac{x+\delta x}{y+\delta y}\right)$. The probability that a particle has a path through the aperture is simply

$$P = \frac{\vartheta_2 - \vartheta_1}{\pi} = \frac{\arctan\left(\frac{x+\delta x}{y+\delta y}\right) - \arctan\left(\frac{x}{y}\right)}{\pi}. \tag{2.16}$$

This expression is exact, but it is very useful to have an approximation for cases where the aperture is far away from the point of particle emission. This would correspond to the scenario where $x \gg \delta x$ and $y \gg \delta y$, allowing for a Taylor expansion of $\arctan\left(\frac{x+\delta x}{y+\delta y}\right)$. If second order terms are neglected, Equation 2.16 becomes

$$\frac{\arctan\left(\frac{x+\delta x}{y+\delta y}\right) - \arctan\left(\frac{x}{y}\right)}{\pi} \approx \frac{y\delta x - x\delta y}{\pi\left(x^2 + y^2\right)}. \tag{2.17}$$

Using the surface normal $\vec{n}$ and distance to the aperture center $|\vec{r}|$, Equation 2.17 may be rewritten. Given the geometry, these quantities are

$$\vec{n} = -\delta y\hat{x} + \delta x\hat{y} \tag{2.18}$$

and

$$\vec{r} = -\left(x + \delta x/2\right)\hat{x} - \left(y + \delta y/2\right)\hat{y}. \tag{2.19}$$

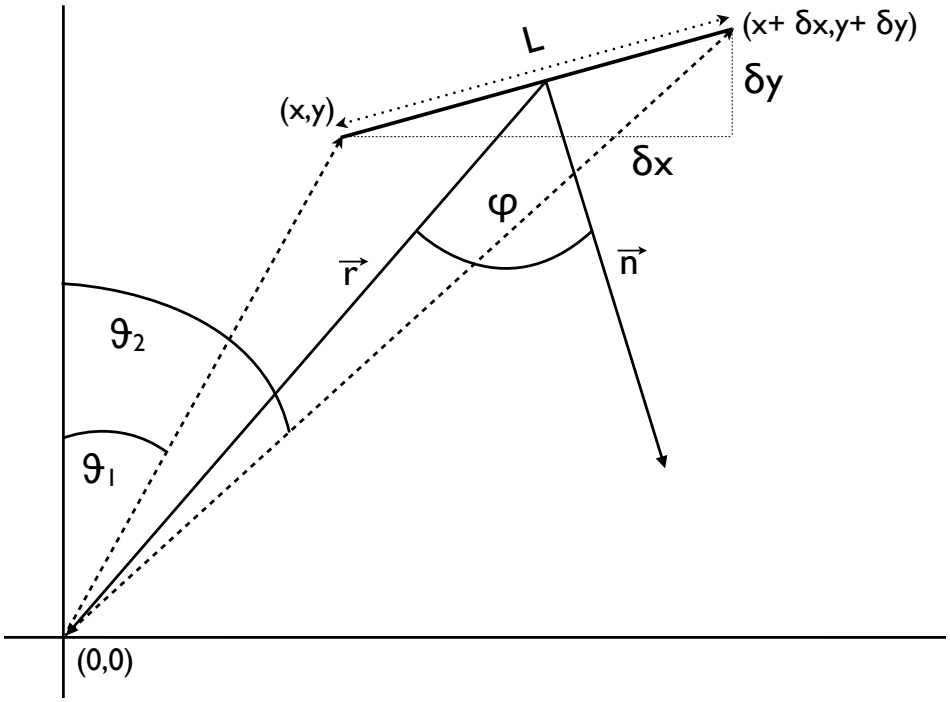

Figure 2.11: 2D Geometry. [A neutron that emits isotropically from the origin must lie between the angles ϑ_1 and ϑ_2 to be detected. The vector $\vec{r}$ points from the center of the detector aperture to the particle emission point and $\vec{n}$ is normal to the aperture.]

Note that the magnitude of $\vec{n}$ is L and $\vec{r}$ is $\sqrt{x^2+y^2}$ (if first order terms are neglected).

From these definitions it may be concluded that

$$\vec{n}\cdot\vec{r} = L|\vec{r}|\cos(\varphi) \approx y\delta x - x\delta y, \tag{2.20}$$

where second order terms are neglected and θ is the angle between the vectors $\vec{n}$ and $\vec{r}$. Finally, Equation 2.17 may be rewritten as

$$P \approx \frac{L\cos(\varphi)}{\pi|\vec{r}|}. \tag{2.21}$$

Table 2.3: 2D/3D analogy

Dimension	2D	3D
Length	L	$\mathcal{A}$
Angle	Radian	Solid Angle
Normalization	π	2π
Angle Estimate	$L\cos(\varphi)/\lvert\vec{r}\rvert$	$\mathcal{A}\cos(\varphi)/\lvert\vec{r}\rvert^2$
Probability Estimate	$L\cos(\varphi)/(\pi\lvert\vec{r}\rvert)$	$\mathcal{A}\cos(\varphi)/(2\pi\lvert\vec{r}\rvert^2)$

Equation 2.21 may be given an intuitive description. Recalling that the definition of the radian is the arclength of a circle divided by the radius of the circle, the quantity $L\cos(\varphi)$ may be interpreted as the projected length of L onto a circle of radius $|\vec{r}|$. The quantity $\frac{L\cos(\varphi)}{|\vec{r}|}$ is just an arclength divided by the radius of a circle, precisely the definition of a radian.

The 3D case is analogous to the 2D case (see Table 2.3). In 2D the necessary value was a radian, while in three dimensions it is the solid angle. If the aperture is circular, the set of points from the emission site of a neutron to the aperture creates a solid angle subtending a cone. Just like in the 2D case, the angle is proportional to the probability P.

The approximation in the 2D case holds in three dimensions as well. In this case, the result is

$$P \approx \frac{\mathcal{A}\cos(\varphi)}{2\pi|\vec{r}|^2}. \tag{2.22}$$

The quantity $|\vec{r}|^2$ is the magnitude squared of the vector from the aperture center to the point of emission and $\cos(\varphi)$ is the cosine of the angle between this vector and the pointing direction vector.

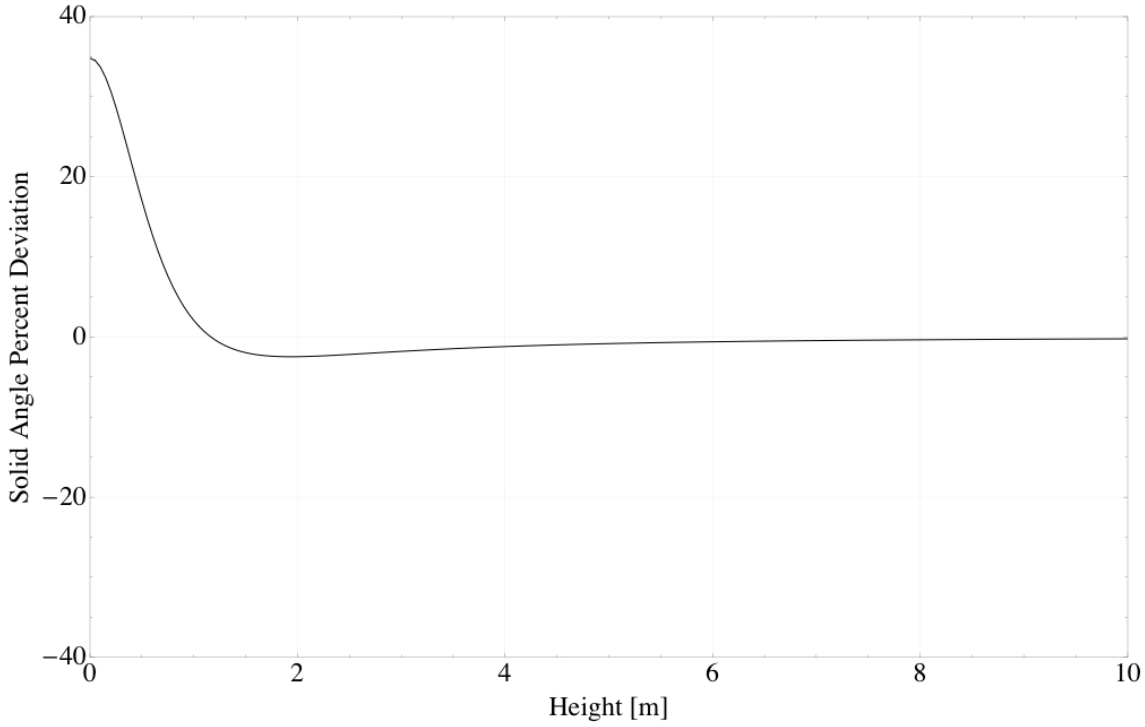

Figure 2.12: Height Convergence of Solid Angle. [For a particle emitted a horizontal distance of one meter from a square meter circular aperture, the above shows the percent deviation of the approximation to the exact solid angle as a function of height.]

The quantity $\mathcal{A}\cos(\varphi)$ is the projected area of the aperture area $\mathcal{A}$ onto a sphere of radius $|\vec{r}|$. Thus, the quantity $\frac{\mathcal{A}\cos(\varphi)}{|\vec{r}|^2}$ is the solid angle generated by the aperture in the far field limit. The factor of 2π is needed as the normalization for an isotropic distribution since it emits into a hemisphere not a sphere. The exact expression for the solid angle is not used in any calculations but is derived in Appendix B for completeness. The deviation of Equation 2.22 (or, equivalently, solid angle) from the exact expression is illustrated in Figure 2.12. As height increases the deviation approaches zero.

2.10 Sampled Area

In order to calculate the number of particles reaching the detector, it is necessary to integrate the product of geometric probability and flux over the surface area of the footprint. However, if the flux is assumed to be homogeneous, it may be pulled out of the integral. The remaining integral is defined as the sampled area and is denoted by A_s. Detector parameters and the angular distribution of neutrons are encapsulated in this parameter. This is a useful quantity since it allows flux (which is determined by physical parameters such as energy range and weight fraction of water) to be considered as an independent quantity in the calculation of neutron counts.

To calculate sampled area, it is necessary to integrate over the footprint surface $\mathcal{S}$ and include the probability that a particle emitted from some area element $\mathrm{d}x_1\,\mathrm{d}x_2$ is "detected". The integral for the quantity A_s becomes

$$A_s = \iint_{\mathcal{S}} P(x_1, x_2)\sqrt{1 + \left(\frac{\partial x_3}{\partial x_1}\right)^2 + \left(\frac{\partial x_3}{\partial x_2}\right)^2}\,\mathrm{d}x_1\,\mathrm{d}x_2, \tag{2.23}$$

where P is the geometric probability defined by Equation 2.22. Note that since P (Equation 2.22) is proportional to aperture area ($\mathcal{A}$), the sampled area is also proportional to the aperture area.

Using the same parametrization as the one in Section 2.7 it is possible to evaluate Equation 2.23.

$$A_s \approx \sum_{j=1}^{\beta} \Delta\alpha \int_{y_j}^{Y_j} P(\alpha_j, x_2)\sqrt{1 + \left(\frac{\partial x_3}{\partial x_1}\right)^2\bigg|_{\alpha_j} + \left(\frac{\partial x_3}{\partial x_2}\right)^2}\,\mathrm{d}x_2 \tag{2.24}$$

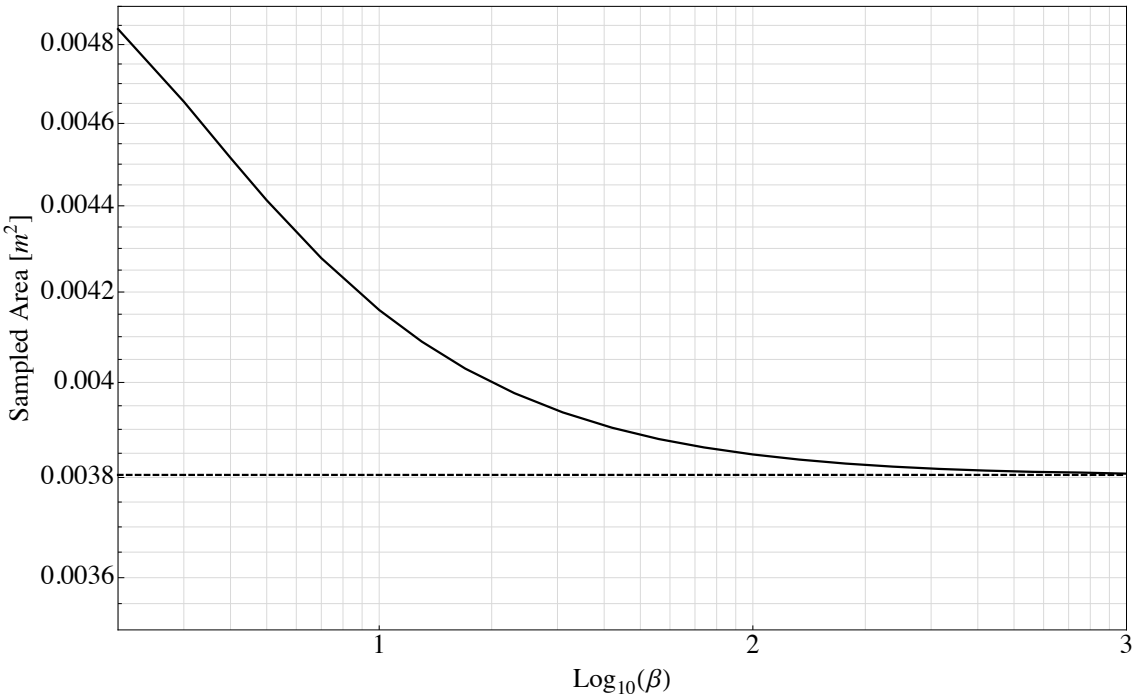

Figure 2.13: Sampled Area Convergence. [For a detector with an aperture area of 1 square meter, opening angle of 5°, located 100 meters above the crater center, and looking downwards, the sampled area calculation converges as beta increases. The dashed line is the exact value of the sampled area.]

The rest of the calculation is equivalent to that of Section 2.7. Figure 2.13 shows the convergence of sampled area as a function of β.[3]

2.11 Sampled Area Estimate

As a check on the numerical results of sampled area, it is useful to have a simple analytic order of magnitude estimate. Figure 2.14 will be used as a guide.

[3]The parameter β was taken to be 400 for all sampled area computations.

For a circular aperture with an opening angle ϑ_o, pointing straight downward a distance h above a flat surface, the integral for the sampled area becomes

$$A_s = \int_0^{2\pi} \int_0^{h\tan(\vartheta_o)} \frac{\mathcal{A}h}{2\pi\left(s^2+h^2\right)^{3/2}} s \, \mathrm{d}s \, \mathrm{d}\phi, \tag{2.25}$$

which may be evaluated to yield

$$A_s = \mathcal{A}\left[1-\cos\left(\vartheta_o\right)\right]. \tag{2.26}$$

From Equation 2.26 inspection shows that for small ϑ_o the sampled area should be of the order $\mathcal{A}(\vartheta_0)^2$. This will be taken to be the sampled area estimate A_E, that is,

$$A_E = \mathcal{A}(\vartheta_0)^2. \tag{2.27}$$

Although the quantity A_E was derived under a comparatively simpler scenario than that of the crater, it will be used to estimate sampled area in the following section. This may be used because there are scenarios where the crater geometry is similar to a flat plane (Figure 2.9).

2.12 Pointing Direction, Sampled Area, Opening Angle, and Aperture Area Trends

The sampled area for the same scenarios considered in Section 2.8 are shown in Figure 2.15. As the polar angle increases the sampled area increases monotonically. This is caused by two primary effects. The first comes from the dependence on

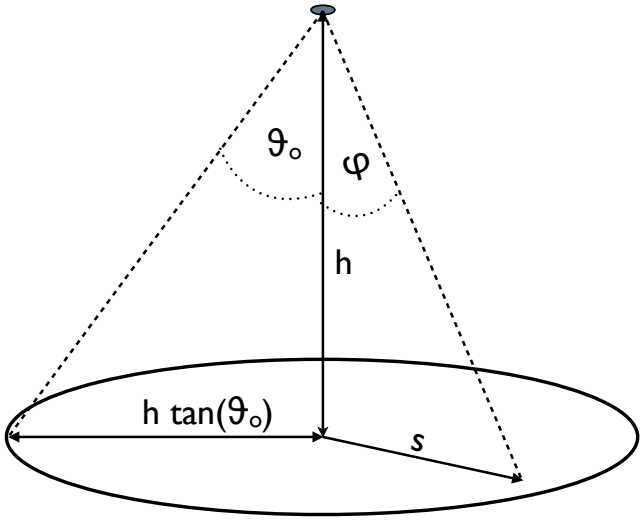

Figure 2.14: Sampled Area Estimate Geometry. [The small dark circle represents the detector and the large circle respresnts the footprint.]

probability with distance. Since the detector is located at $(180°, 0)$ in this scenario, as the polar angle approaches this value the footprint will be, on average, closer to the detector; thus, particles will have a higher probability of being detected. Furthermore, the geometric area does not change very much over the range of values considered in Figure 2.15. Changes in the geometric probability dominate the changes in geometric area, leading to a net gain in sampled area as the footprint comes closer to the detector.

The domain of the graph is chosen due to two considerations: 1) The approximation used to calculate the geometric probability is not expected to hold for points close to the detector and 2) If the field of view is not completely contained within the crater, the numerical scheme used to find the footprint outline is incomplete (the edge

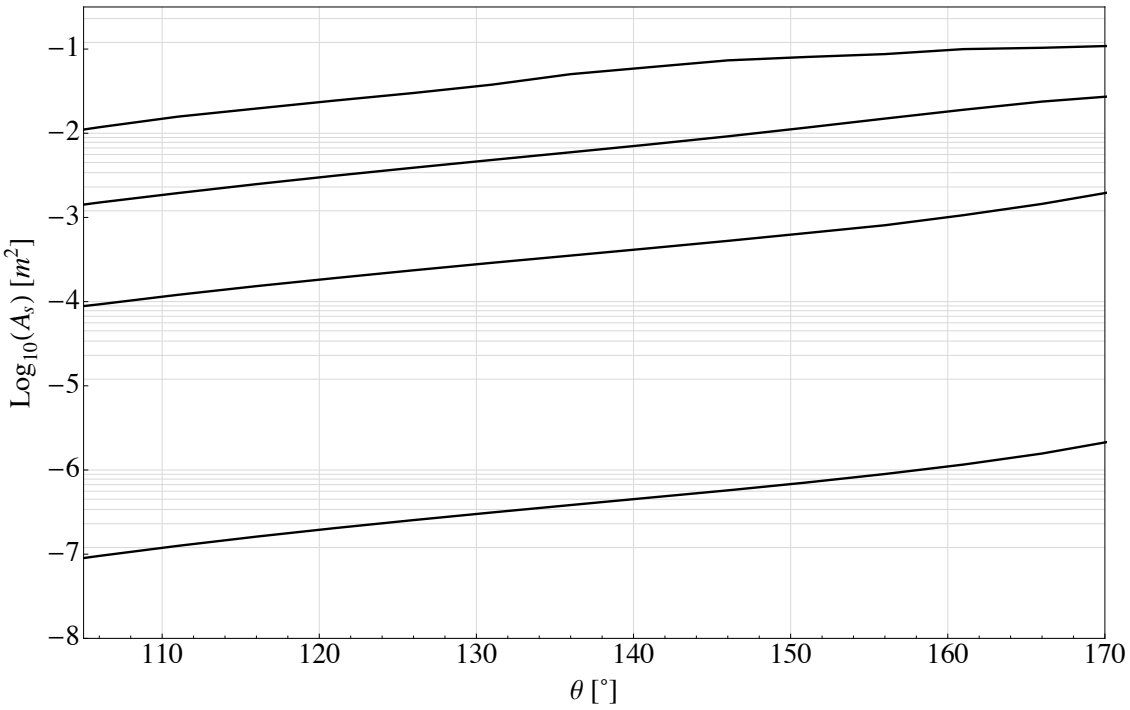

Figure 2.15: Polar Angle, Sampled Area, and Opening Angle Trends. [Above is the sampled area for a detector with an aperture area of 1 square meter in the crater center 1 meter above the ground. From top to bottom the curves correspond to opening angles of $5, 2, 1/2, 1/60$ degrees.]

of the crater is not used in any computations). In regard to the second reason, this should not be a problem for two main reasons: 1) for small halfwidths, the amount of surface area gained from a more complete description would be negligible and 2) the neglected points will be the ones that are farthest away from the detector and will, consequently, contribute the least to sampled area.

The sampled area varies by about an order of magnitude over the domain considered in Figure 2.15. However, the primary effect seems to come from the

Table 2.4: Sampled Area Estimate

ϑ_o [°]	A_E $[m^2]$	$\mathrm{Log}_{10}(A_E)$ $[m^2]$
1/60	8.5×10^{-8}	-7.07
0.5	7.6×10^{-5}	-4.12
2	1.2×10^{-3}	-2.91
5	7.6×10^{-3}	-2.12

detector opening angle. The analysis of Section 2.11 may be used to obtain an estimate of the sampled areas for different opening angles. Using Equation 2.27 the sampled area estimates are displayed in Table 2.4. These rough approximations are in agreement with the values in Figure 2.15 and provide further confidence in the validity of the numerical scheme used to calculate sampled area. Also, it is apparent that the entire range of values in Figure 2.15 is almost within an order of magnitude of the estimates. It seems safe to say that the sampled area has, approximately, a $(\vartheta_o)^2$ dependance.

It was mentioned in Section 2.10 that the sampled area is directly proportional to the aperture area. Thus the effect of changing the aperture size merely rescales the sampled area axis of Figure 2.15. For example, if the aperture area was instead one square centimeter then the sampled area of the 5° opening angle and 170° looking direction case would be about 10^{-3} square meters. This would imply that, of course, a large detector would be better.

CHAPTER 3

NEUTRON SPECTROSCOPY TRENDS

3.1 Introduction

To estimate neutron counts there are three fundamental parameters: sampled area (square meters), flux (neutrons per square meter per second), and the dwell (observation) time (in seconds). Assuming the flux is constant and uniform, the number of neutrons N reaching the aperture is

$$N = A_s \Phi T, \tag{3.1}$$

where Φ is the neutron flux, and T is the dwell time. As shown previously (Figure 1.3), the neutron flux varies with the weight fraction of water. Ultimately, the goal is to distinguish between different weight fractions of water. To this end, a likelihood method is employed.

3.2 Likelihood Ratio Method

The likelihood ratio method enables a comparison of different hypotheses [33]. Specifically, it provides a statistical measure. The way this statistic is used here is to assume a "null hypothesis" to which every other hypothesis is compared.

For counting experiments, Poisson statistics are an appropriate description. A Poisson distribution $\mathcal{P}$ with an expected count μ and detected count x is given by

$$\mathcal{P}(x,\mu) = \frac{\mu^x e^{-\mu}}{x!}. \tag{3.2}$$

The likelihood ratio statistic is defined as the ratio of $\mathcal{P}(x,\mu)$ to $\mathcal{P}(\mu,\mu)$, where μ is the mean number of counts associated with the null hypothesis. However, the quantity of importance is

$$\lambda = -2\ln\left(\frac{\mathcal{P}(x,\mu)}{\mathcal{P}(\mu,\mu)}\right) \tag{3.3}$$

since it is distributed as chi-squared and thus provides a statistical measure. This statistic can also determine the confidence level with which the null hypothesis may be rejected. This confidence level is defined as

$$\text{confidence level } = \int_0^\lambda \chi_1^2(x)\,\mathrm{d}x,$$

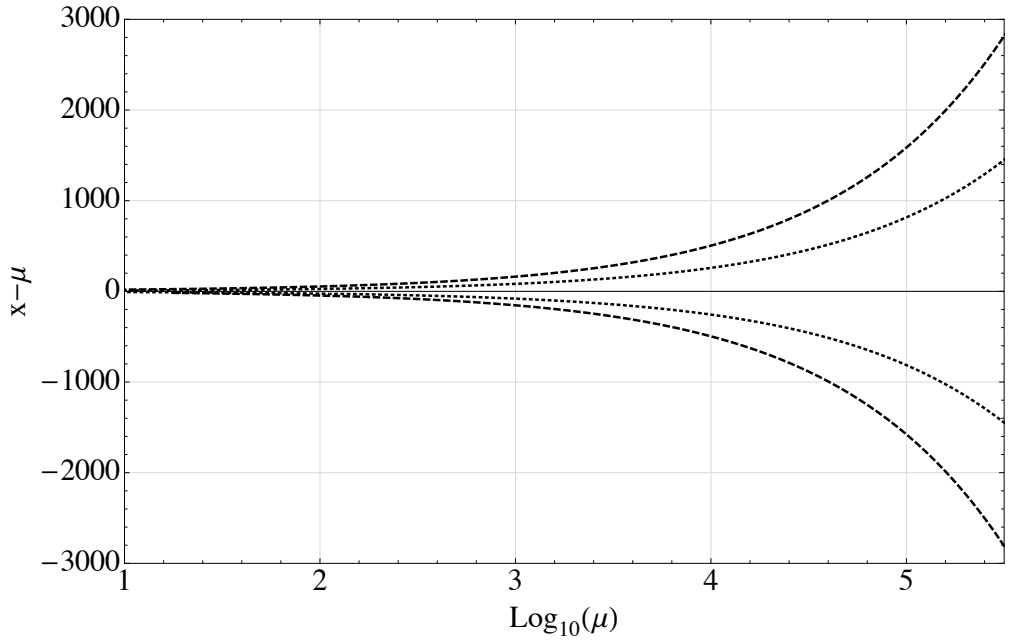

Figure 3.1: Threshold Curves. [The thick and thin dashed lines represent the necessary ordered pairs $(x, x-\mu)$ that satisfy the 99.9999% and 99% threshold criteria, respectively.]

where $\chi^2_1(x)$ is a chi-squared distribution with one degree of freedom. It has one degree of freedom because every other hypothesis is being compared to one hypothesis: the null hypothesis [33].

The confidence level is used to define a threshold criteria for rejecting the null hypothesis. For this work, the threshold values were chosen to be 99% ($\lambda = 6.635$) and 99.9999% ($\lambda = 25$). These values were chosen because they roughly correspond to a 3σ and 5σ measurement.

The threshold curves that satisfy the 99% and 99.9999% threshold are shown in Figure 3.1 as a function of μ, where the y-axis is the deviation from the mean.

Table 3.1: Flux Φ_i and Weight Fraction of Water List [13].

Weight Fraction (% weight H_2O)	Index	Epithermal Flux ($n\ m^{-2}s^{-1}$)	Low-Epithermal Flux ($n\ m^{-2}s^{-1}$)	Thermal Flux ($n\ m^{-2}s^{-1}$)
0	0	41,046	5,761	5,284
0.022	1	40,325	5,697	5,395
0.045	2	39,774	5,615	5,491
0.068	3	39,159	5,562	5,551
0.1	4	38,400	5,478	5,666
0.3	5	34,479	5,056	6,188
0.4	6	32,831	4,879	6,396
0.5	7	31,328	4,705	6,565
0.8	8	27,840	4,337	6,921
1	9	26,014	4,127	7,023
2	10	19,946	3,274	7,412
5	11	12,301	2,121	6,723
10	12	7,954	1,387	5,430
30	13	3,409	574	2,809
100	14	1,012	163	854

The x that satisfies Equation 3.3 for a given μ and λ is solved for numerically. In Figure 3.1 it is seen that there are two ways to obtain the threshold criteria: excess or deficit relative to the mean.

3.3 Neutron Counts, Weight Fraction of Water, and Flux

A simulation to obtain neutron flux spectra for various lunar soils and water content has already been done [13]. Here the flux spectra for ferroan anorthosite regolith is used. To obtain fluxes, this spectrum was integrated over the energy ranges defined by Table 1.1 for epithermal, low-epithermal, and thermal neutrons.

The weight fraction of water and corresponding flux (neutrons per square meter per second) are listed in Table 3.1 for different energy ranges. The number of neutrons from within the field of view N_i associated with a particular flux Φ_i (and, consequently, weight fraction of water) is

$$N_i = A_s T \Phi_i. \tag{3.4}$$

3.4 Statistical Significance of Neutron Measurements

The goal of a mission with a surface based neutron spectrometer would be to identify any amount of water. Therefore, the null hypothesis to which every other hypothesis will be compared is dry regolith (0% weight fraction of water). The statistical significance of a deviation from the null hypothesis is assigned using the likelihood method. At first no background will be considered.

Suppose the null hypothesis is true and the detector observes some patch of area for a time T_0. Then the expected number of detected neutrons N_0 is

$$N_0 = A_s \Phi_0 T_0. \tag{3.5}$$

For any other scenario (hypothesis) the expected number of neutrons would be

$$N_i = A_s \Phi_i T_0. \tag{3.6}$$

The variable T_0 may be eliminated using Equation 3.5 to write this as

$$N_i = \frac{\Phi_i}{\Phi_0} N_0. \tag{3.7}$$

Therefore, the neutron enhancement (or suppression) ΔN is

$$\Delta N \equiv N_i - N_0 = \left(\frac{\Phi_i}{\Phi_0} - 1 \right) N_0. \tag{3.8}$$

The likelihood method is now used to quantify the statistical significance of a deviation from the null hypothesis.

Using Equation 3.8 the expected neutron enhancement (or suppression) is graphed as solid lines for different weight fractions of water (hypotheses). Also, by superimposing the threshold curves of Figure 3.1 (with $x \to N_i$ and $\mu \to N_0$) on the same plot, it is possible to see where the deviations from the null hypothesis first attain the relevant threshold. This will lie on the intersection of the dashed threshold curves in Figure 3.2, Figure 3.3, and Figure 3.4 with the solid water-content curves.

Only neutron deficits are expected for epithermal (and low-epithermal) neutrons, as shown in Figure 3.2 and Figure 3.3. This is caused by the monotonic decrease of epithermal flux with increasing weight fraction of water (Table 3.1). On the other hand, Figure 3.4 shows that for thermal neutrons there is both neutron enhancement and suppression. This is expected because in Table 3.1 only the 30% and 100% weight fraction of water are smaller than the null thermal flux.

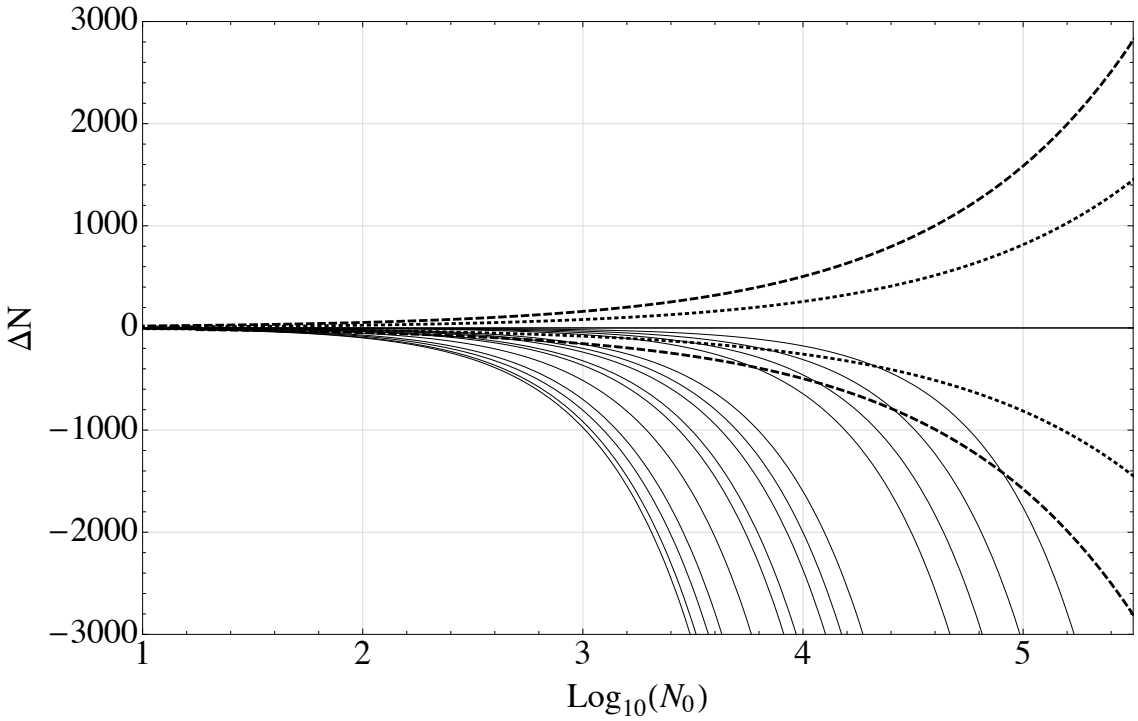

Figure 3.2: Epithermal and Threshold Curves. [The thick and thin dashed curves are the ordered pairs that meet the 99.9999% and 99% thresholds respectively. The solid curves are the neutron deficits with respect to the null hypothesis for different weight fractions of water (Section 3.3) in the epithermal energy range. Left to right corresponds to decreasing the weight fraction of water.]

To obtain an expression for the intersection of the threshold curves with the water-content curves, Equation 3.7 is used in conjunction with Equation 3.3. The intersection could be specified by either (N_0, N_i) or $(N_0, \Delta N)$. Since N_i and ΔN depend on N_0 via Equation 3.7, it is only necessary to use N_0 to describe the intersection. However, the intersection will depend on the weight fraction of water being considered; thus, instead of using N_0, the notation will be changed to $N_{0,i}$. The exact

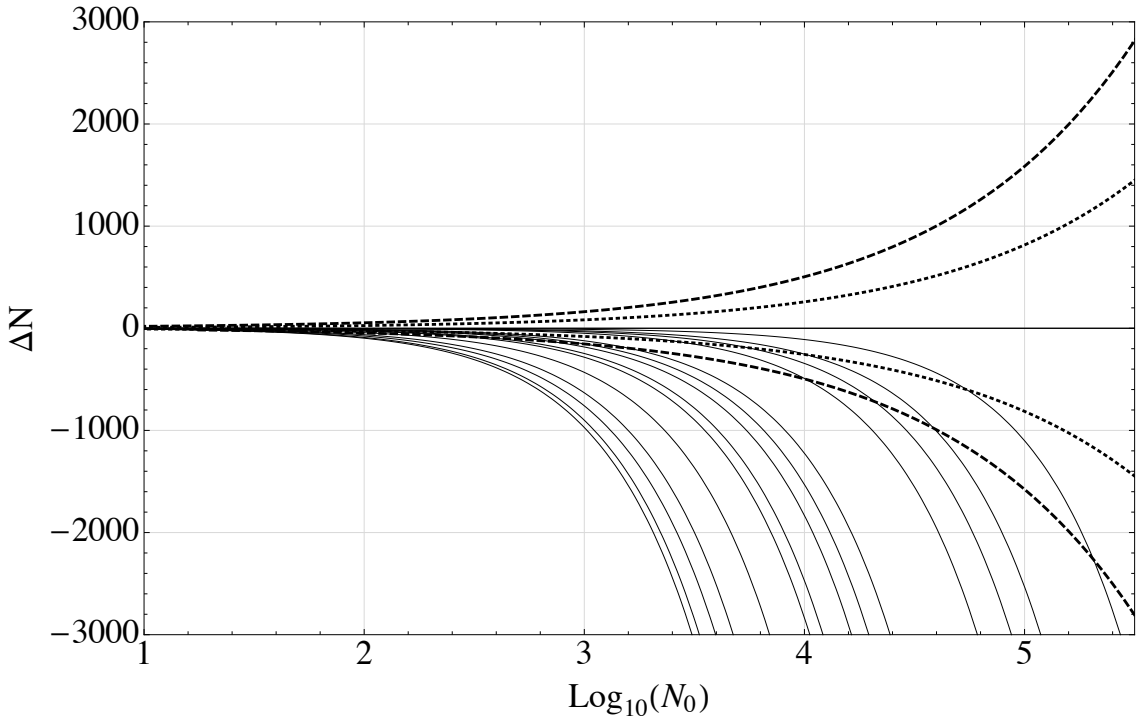

Figure 3.3: Low-Epithermal and Threshold Curves. [The thick and thin dashed curves are the ordered pairs that meet the 99.9999% and 99% thresholds respectively. The solid curves are the neutron deficits with respect to the null hypothesis for different weight fractions of water (Section 3.3) in the low- epithermal energy range. Left to right corresponds to decreasing the weight fraction of water.]

expression for the intersection is

$$\frac{\lambda}{2} = \left(\frac{\Phi_i}{\Phi_0} - 1\right) N_{0,i} \ln\left(N_{0,i}\right) + \ln\left(N_{0,i}!\right) - \ln\left(\left[\frac{\Phi_i}{\Phi_0} N_{0,i}\right]!\right). \tag{3.9}$$

Assuming that $\frac{\Phi_i}{\Phi_0} N_{0,i}$ and $N_{0,i}$ are large justifies Stirling's approximation on the factorial terms of Equation 3.9. The asymptotic expression for $N_{0,i}$ under these

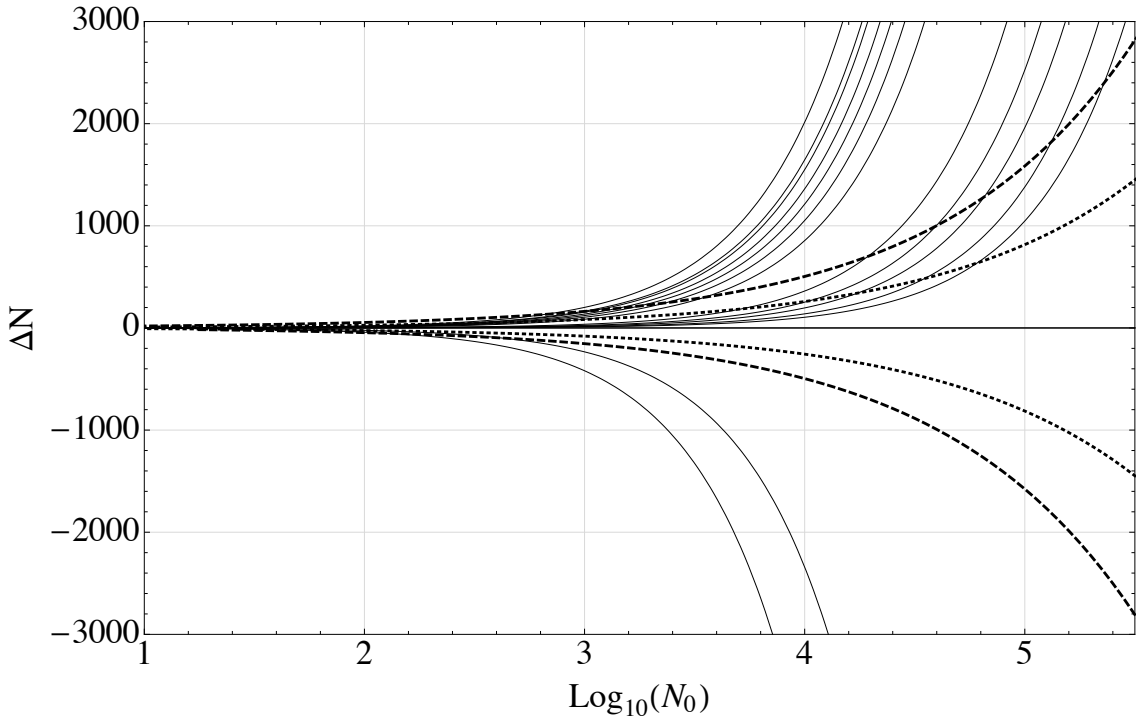

Figure 3.4: Thermal and Threshold Curves. [The thick and thin dashed curves are the ordered pairs that meet the 99.9999% and 99% thresholds respectively. The solid curves are the neutron enhancements or deficits with respect to the null hypothesis for different weight fractions of water (Section 3.3) in the thermal energy range. The deficits correspond to 100% and 30% weight fractions of water from left to right.]

circumstances is

$$N_{0,i} \approx \frac{\lambda}{2\left(\frac{\Phi_i}{\Phi_0}\ln\left(\frac{\Phi_i}{\Phi_0}\right) - \frac{\Phi_i}{\Phi_0} + 1\right)}. \tag{3.10}$$

Equation 3.10 will not be valid for large water contents in the epithermal and low-epithermal ranges since the ratio $\frac{\Phi_i}{\Phi_0}$ is low. This is also true for thermal neutrons but for water contents that are $\geq 30\%$.

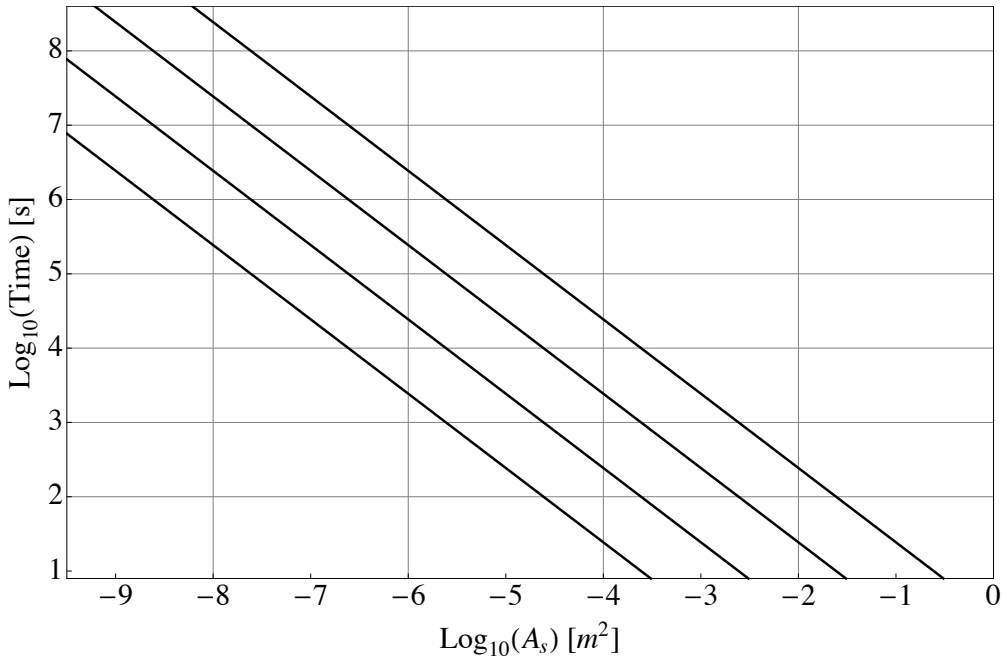

Figure 3.5: Sampled Area, Time, and Epithermal Neutron Count Trends. [From top to bottom the number of neutrons are 10^5, 10^4, 10^3, 10^2.]

3.5 Sampled Area, Time, and Neutron Count Trends

The number of neutrons necessary to reject the null hypothesis (attain a threshold) defines a dwell time T for the detector. Dwell time is defined with respect to the number of neutrons from the null hypothesis as follows:

$$T = \frac{N_{0,i}}{\Phi_0 A_s}, \tag{3.11}$$

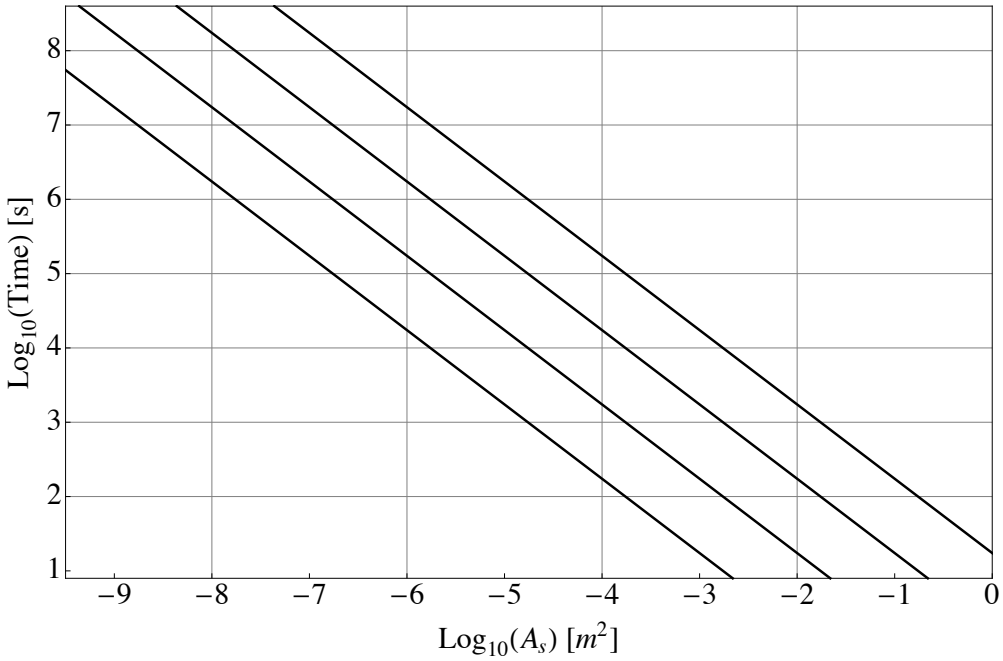

Figure 3.6: Sampled Area, Time, and Low-Epithermal Neutron Count Trends. [From top to bottom the number of neutrons are 10^5, 10^4, 10^3, 10^2.]

where the number of neutron counts $N_{0,i}$ is defined by the intersection of a threshold curve with a water-content curve (Equation 3.9). This number will depend on the threshold criteria and weight fraction of water that is being considered.

Dwell time is plotted as a function of sampled area for different energy ranges and neutron counts in Figure 3.5 and Figure 3.6. The thermal range is not considered because the null flux is similar to the low-epithermal range.

3.6 Background Ratio

In the previous sections it was assumed that all detected neutrons come from within the telescope FoV. However, these are not the only kinds of particles that can be detected. It is possible that background may contribute to neutron counts. Physically, this would correspond to particles leaking through or being generated from the collimator. These particles may come from outside the field of view of the detector or, perhaps, the instrument itself.

If background is included, the total number of neutrons N_0 expected from the null hypothesis comes from two sources: the FoV (N_F) and the background (N_B). Thus,

$$N_0 = N_F + N_B. \tag{3.12}$$

This is rewritten by introducing the background ratio ξ

$$\xi \equiv \frac{N_B}{N_F} \Rightarrow N_0 = N_F(1+\xi). \tag{3.13}$$

A value of $\xi = 1$ would mean that 50% of neutrons come from background (in the null hypothesis) and $\xi = 9$ would mean that 90% of neutrons come from background (in the null hypothesis). In addition, the formula $N_F = A_s T \Phi_0$ implies that background is

$$N_B = A_s T \Phi_0 \xi \tag{3.14}$$

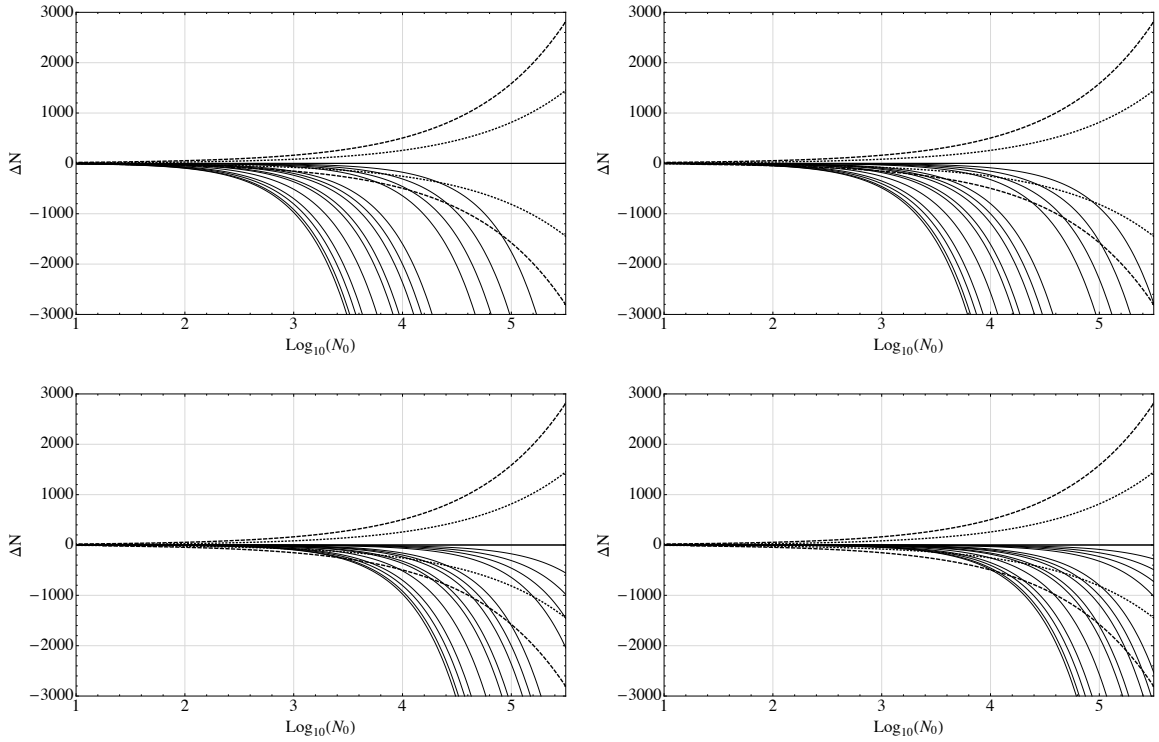

Figure 3.7: Epithermal and Threshold Curves with Background. [The thick and thin dashed curves are the ordered pairs that meet the 99.9999% and 99% thresholds respectively. The solid curves are the neutron deficits with respect to the null hypothesis for different weight fractions of water (Section 3.3) in the epithermal energy range. The upper left and right figures correspond to no background and 50% of neutrons coming from background (in the null hypothesis), respectively, while the lower left and lower right figures are 90% and 95%, respectively.]

and that the total number of neutron counts $N_i^{(\xi)}$ for different weight fractions of water and background ratios is

$$N_i^{(\xi)} = A_s T \Phi_i + A_s T \Phi_0 \xi, \tag{3.15}$$

where the $A_s T \Phi_i$ term comes from neutrons within the field of view.

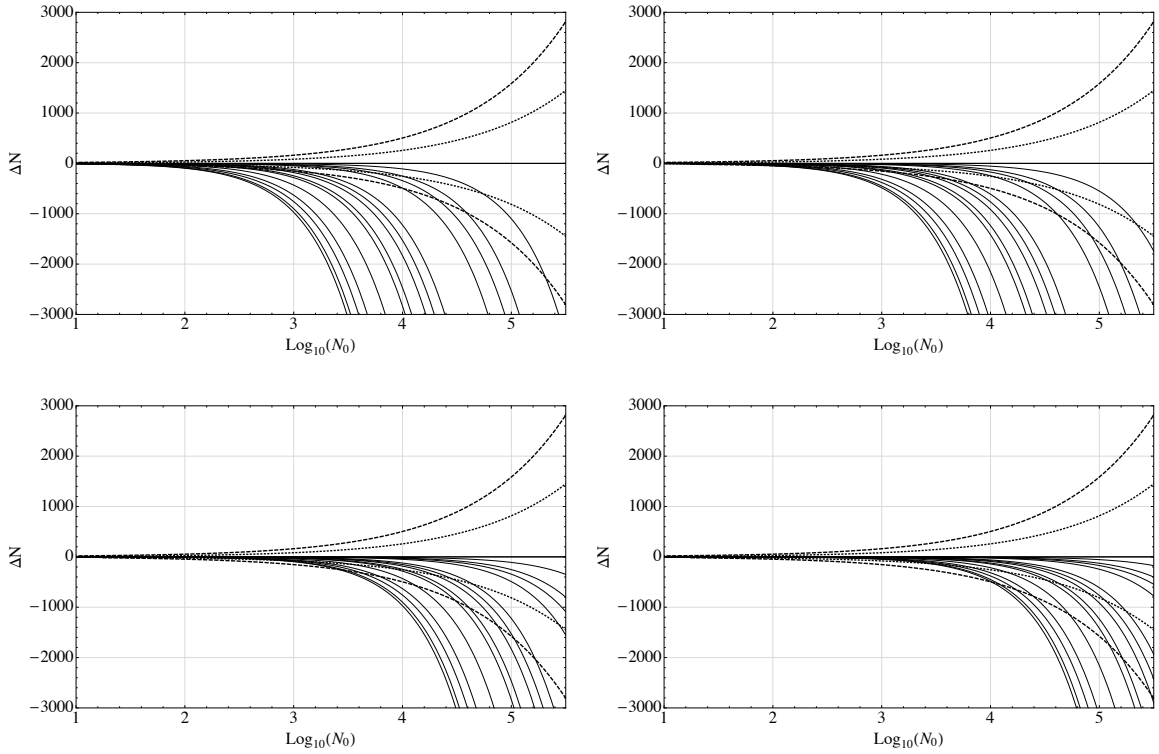

Figure 3.8: Low-Epithermal and Threshold Curves with Background. [The thick and thin dashed curves are the ordered pairs that meet the 99.9999% and 99% thresholds respectively. The solid curves are the neutron deficits with respect to the null hypothesis for different weight fractions of water (Section 3.3) in the low-epithermal energy range. The upper left and right figures correspond to no background and 50% of neutrons coming from background (in the null hypothesis), respectively, while the lower left and lower right figures are 90% and 95%, respectively.]

Figure 3.7, Figure 3.8, and Figure 3.9 show the effect that adding background has on the statistical significance of a deviation from the null hypothesis: a larger deviation is necessary to attain a threshold.

An approximate expression for the intersection of the threshold curves with the water-content curves can be obtained analogous to Section 3.4. Equation 3.10 is

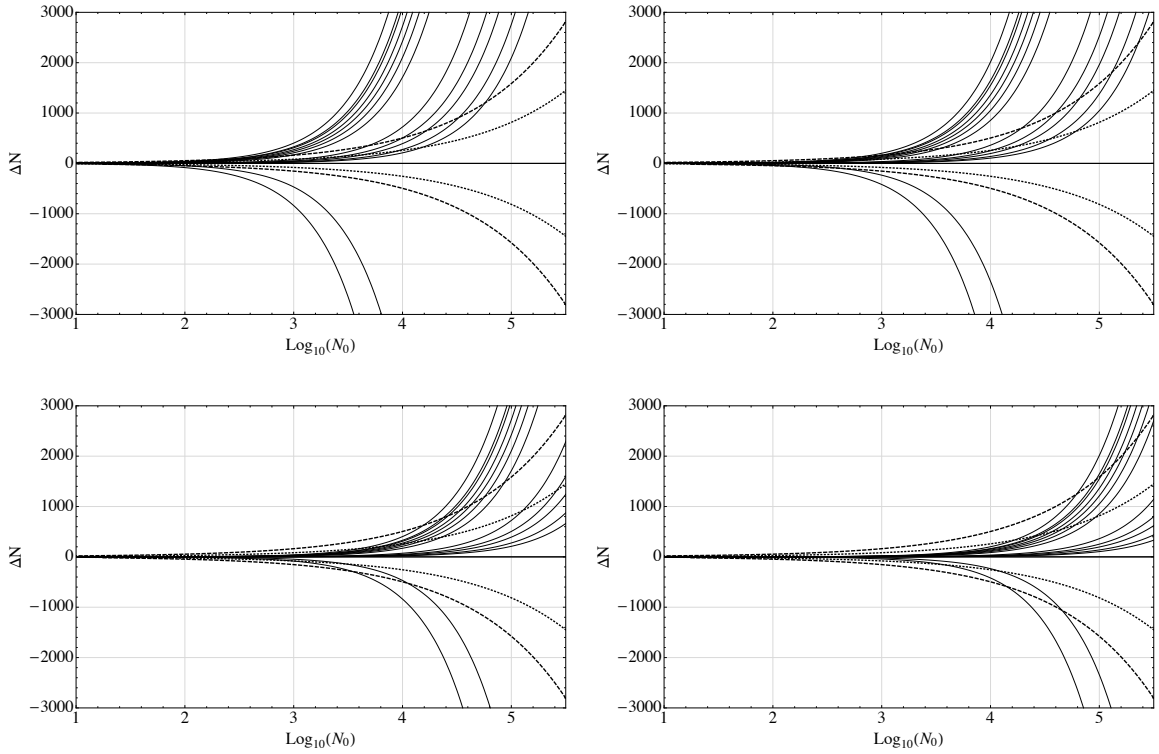

Figure 3.9: Thermal and Threshold Curves with Background. [The thick and thin dashed curves are the ordered pairs that meet the 99.9999% and 99% thresholds respectively. The solid curves are the neutron deficits with respect to the null hypothesis for different weight fractions of water (Section 3.3) in the thermal energy range. The upper left and right figures correspond to no background and 50% of neutrons coming from background (in the null hypothesis), respectively, while the lower left and lower right figures are 90% and 95%, respectively.]

generalized to include background and becomes

$$N_{0,i}^{(\xi)} \approx \frac{\lambda}{2\left(\left[\frac{\Phi_i/\Phi_0+\xi}{1+\xi}\right]\ln\left(\left[\frac{\Phi_i/\Phi_0+\xi}{1+\xi}\right]\right)-\left[\frac{\Phi_i/\Phi_0+\xi}{1+\xi}\right]+1\right)}. \tag{3.16}$$

This time, Stirling's approximation must be valid for large $N_{0,i}^{(\xi)}$ and $\left[\frac{\Phi_i/\Phi_0+\xi}{1+\xi}\right] N_{0,i}^{(\xi)}$. Equation 3.16 will not be valid for low backgrounds and large weight fractions of water, but it is valid for larger backgrounds regardless of water content in the field of view.

3.7 Time Ratio

It is also expected that it will impact the required dwell time of the detector since the statistical significance of a measurement is affected by background. This effect is considered by defining a parameter that takes into account the relative increase with respect to the zero background case. A ratio of the background dwell time $T_i^{(\xi)}$ to the zero background dwell time $T_i^{(0)}$ fits this role. Solving Equation 3.15 for time, then taking the ratio of the background case to the no background case, yields the equation for the time ratio $\mathcal{T}_i$

$$\mathcal{T}_i = \frac{T_i^{(\xi)}}{T_i^{(0)}} = \frac{N_{0,i}^{(\xi)}}{N_{0,i}^{(0)}\,(1+\xi)}. \tag{3.17}$$

The quantities $N_{0,i}^{(\xi)}$ and $N_{0,i}^{(0)}$ are the number of null hypothesis neutrons associated with a deviation necessary to meet a threshold criteria.

The time ratio is estimated by using the asymptotic expressions for $N_i^{(\xi)}$ (Equation 3.16) and $N_i^{(0)}$ (Equation 3.10). Assuming the necessary conditions are satisfied,

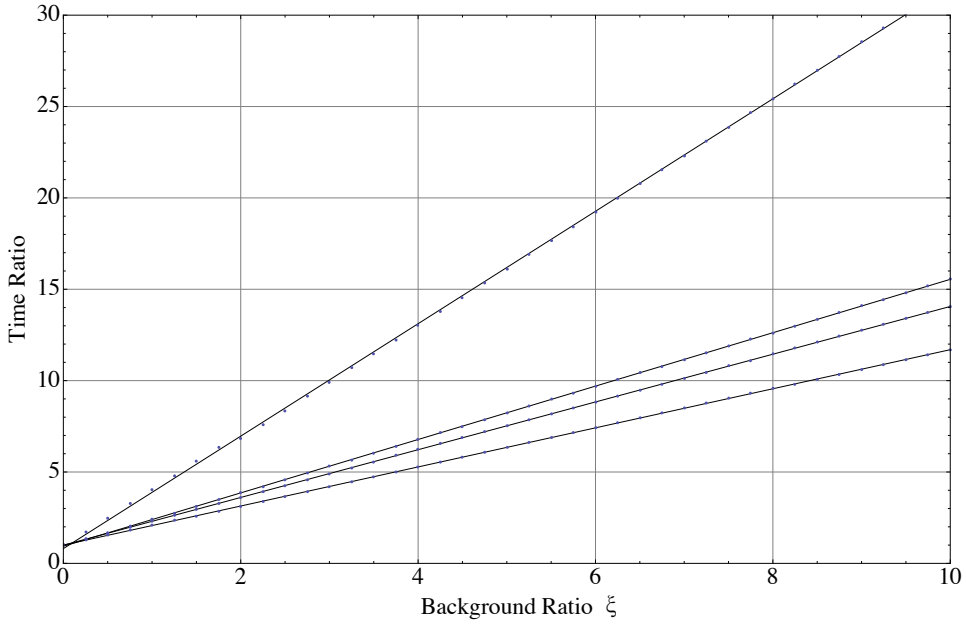

Figure 3.10: Low-Epithermal Time Ratio for the 99% Threshold. [From top to bottom the corresponding weight fractions of water are 5, 1, 0.5, 0.1 percent.]

the time ratio is

$$\mathcal{T}_i \approx \frac{\frac{\Phi_i}{\Phi_0}\ln\left(\frac{\Phi_i}{\Phi_0}\right) - \frac{\Phi_i}{\Phi_0} + 1}{(\Phi_i/\Phi_0 + \xi)\ln\left(\frac{\Phi_i/\Phi_0+\xi}{1+\xi}\right) - \Phi_i/\Phi_0 + 1} \tag{3.18}$$

$$\approx 1 + \frac{\frac{\Phi_i}{\Phi_0} - \ln\left(\frac{\Phi_i}{\Phi_0}\right) - 1}{\frac{\Phi_i}{\Phi_0}\ln\left(\frac{\Phi_i}{\Phi_0}\right) - \frac{\Phi_i}{\Phi_0} + 1}\xi, \tag{3.19}$$

where Equation 3.19 is a Taylor expansion of Equation 3.18 about the point $\xi = 0$, truncated to first order.

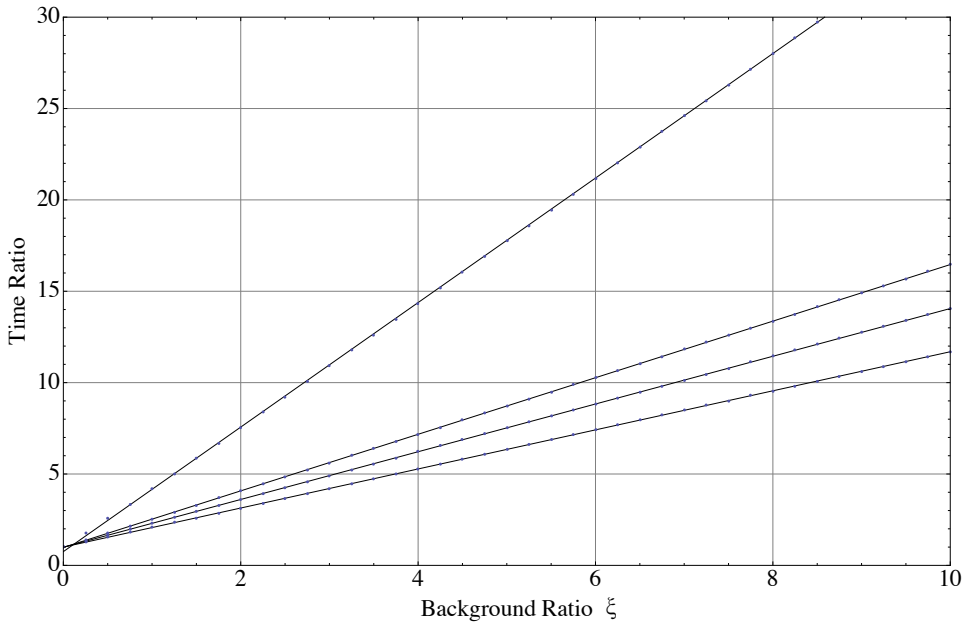

Figure 3.11: Low-Epithermal Time Ratio for the 99.9999% Threshold. [From top to bottom the corresponding weight fractions of water are 5, 1, 0.5, 0.1 percent.]

The time ratio (for different weight fractions of water, threshold criteria, and energy ranges) as a function of background ratio is shown in Figure 3.10, Figure 3.11, and Figure 3.12. To plot these curves, the exact expression for time ratio is used. Figure 3.10 and Figure 3.11 seem to contradict Equation 3.18 since the curves depend on the threshold criteria; whereas, Equation 3.18 has no dependence. There is, however, no such problem. Only the upper two lines are significantly different from each other and these curves do not meet the requirement for using Equation 3.18. For Figure 3.12, only the 99% threshold is shown because it is not significantly different from the 99.9999% threshold.

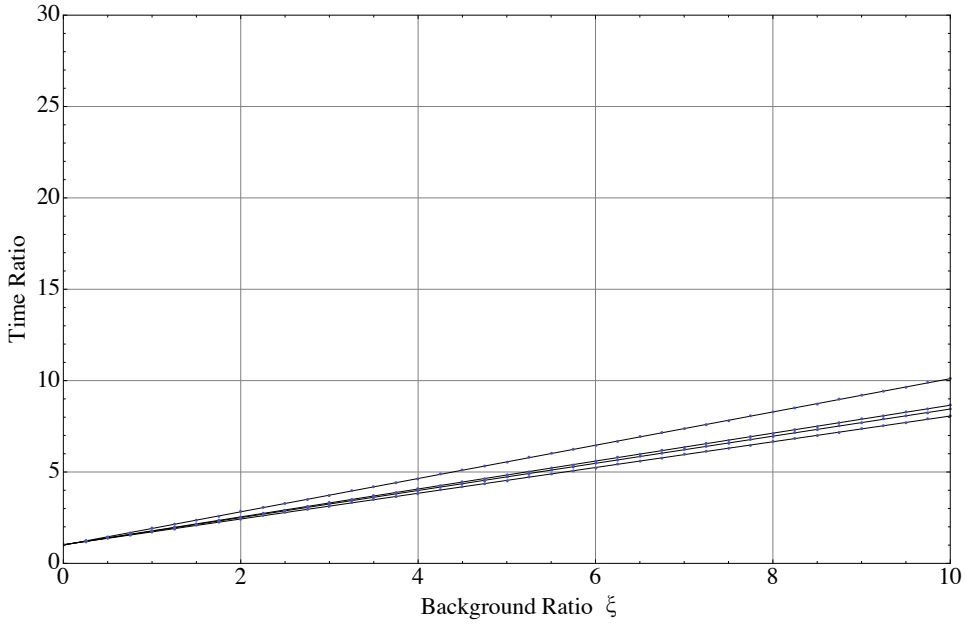

Figure 3.12: Thermal Time Ratio for the 99% Threshold. [From top to bottom the corresponding weight fractions of water are 0.1, 0.5, 5, 1 percent.]

3.8 Crater Survey Time

A simple estimate to how long it would take to survey a crater is useful in determining the practicality of a given detector configuration. The detector footprint covers an area A_g which is some fraction of the total crater area A_{crater}. For the scenario considered here, the total area of the crater is $\sim 2.15 \times 10^7$ square meters. Assuming (naively) it takes the same amount of time to survey a particular area A_g, the total amount of time τ that it would take to survey the entire crater is

$$\tau \equiv \frac{A_{crater}}{A_g} T\mathcal{T}_i. \tag{3.20}$$

This provides a measure of the feasibility of a particular detector. The geometric area is not constant since it depends on which direction the detector is pointed, but Equation 3.20 is still used regardless. As long as the time τ is a "reasonable" number, a given detector configuration has the possibility of being a good candidate for surveying the entire crater.

3.9 Example Scenario

As an example of how to use the information presented in the previous sections two scenarios will be considered. The first will roughly correspond to parameters in a grazing incidence spectrometer while the second will be an alternative consideration [15].

For a detector with an aperture are of $\mathcal{A} = 1$ square meter, with an opening angle $\vartheta_0 = 1/60°$, located 1 meter above the crater center, and pointed in the direction of $\theta = 160°$, the geometric and sampled area are uniquely specified. From Figure 2.10 and Figure 2.15 these values are $A_s \approx 10^{-6}$ square meters and $A_g \approx 5$ square meters.

Furthermore, the sensitivity of the instrument to a specified weight fraction of water is determined for a detector that operates in the low-epithermal range. The number of neutrons necessary to make a 99.9999% threshold detection for 0.1 weight fraction of water is $\approx 10^4$ (Figure 3.3). Since both A_s and N_0 are known, Figure 3.6 is used to obtain the dwell time of $T \approx 19$ days. However, this does not take into account background. If the background ratio is assumed to be four (80% of neutrons from the null hypothesis are from background), then time ratio is approximately five (using Figure 3.11) and the dwell time would increase to 13 weeks and 3 days. The

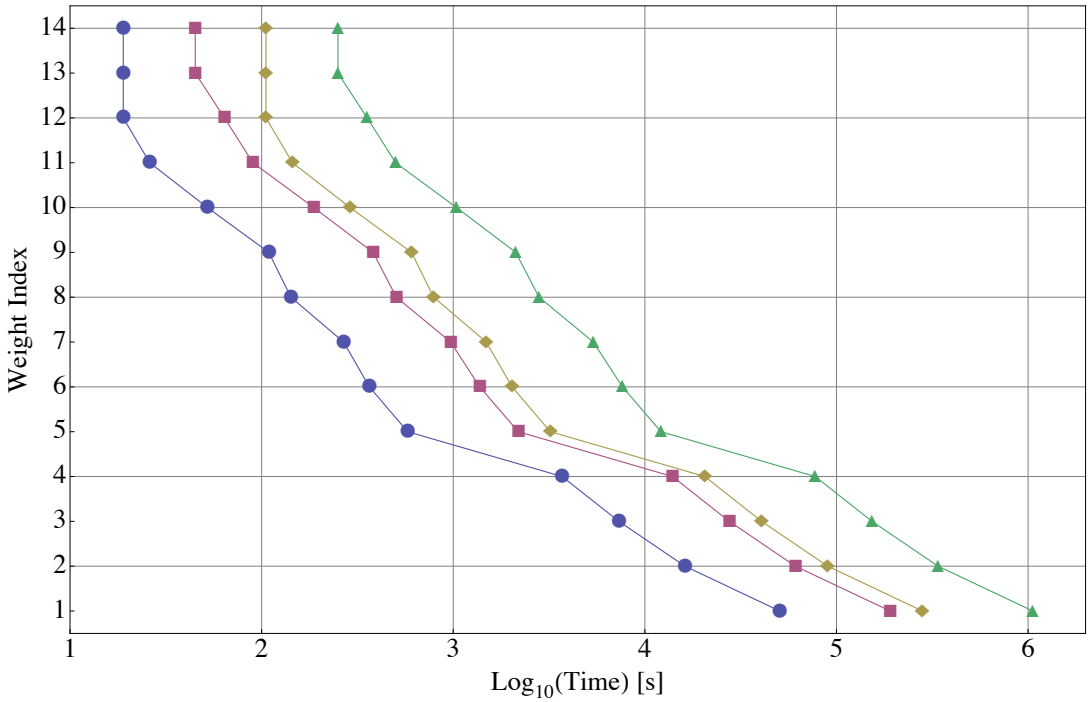

Figure 3.13: The Dwell Time for Various Scenarios. [How the dwell time is affected by changing the weight fraction of water, significance criteria, and pointing direction is shown. Weight indices are provided in Table 3.1. The detector operates in the epithermal range, has an aperture area of ten square centimeters, and an opening angle of two degrees. The circles and diamonds are 99% threshold criteria and the squares and triangles are 99.9999% thresholds. The circle and square correspond to $\theta = 160°$ and the diamond and triangle correspond to $\theta = 110°$.]

approximate amount of time it would take to observe the entire crater is

$\tau \approx 10^6$ years. This unreasonable survey time is attributed to the small opening angle and restricted energy range.

A more reasonable detector would correspond to $\mathcal{A} = 10$ square centimeters, an opening angle of 2°, and a sensitivity to the entire epithermal range. In this case, if it is pointed towards $\theta = 160°$, the amount of time it would take to make a 99.9999%

threshold detection for a 0.1 weight fraction of water is $T \approx 4$ hours and the survey time for the crater would be $\tau \approx 315$ days. However, the resolution of the detector is considerably worse than the grazing-incidence resolution. The geometric area in this case is $A_g \approx 6 \times 10^4$ square meters (Figure 2.10). For the same aperture area and opening angle, the amount of time it takes for a given weight fraction of water to achieve both threshold limits is shown in Figure 3.13 for the particular cases $\theta = 160°$ and $\theta = 110°$. It can be seen that pointing direction, threshold criteria, and weight fraction of water have a significant affect on the dwell time of the detector.

3.10 Application to Orbital Neutron Spectroscopy

The principle features of the model described in this work can also be applied to orbital investigations. As one example, the model is used to make epithermal neutron count rate estimates for the LEND instrument on the *LRO*, a collimated neutron spectrometer. As described previously (Section 2.3), the estimates made here are optimistic since efficiencies are not included.

Orbital neutron spectroscopy is geometrically similar to the scenario considered in Section 2.11. Assuming that the detector is observing dry regolith (0% by weight fraction of water) and that the angular distribution of neutrons is isotropic, the predicted count rate is

$$\mathcal{N}_{model} = A_s \Phi_0 = \mathcal{A}[1 - \cos(\vartheta_o)]\Phi_0, \tag{3.21}$$

where the sampled area is taken from Equation 2.26.

Equation 3.21 assumes a 100% detection efficiency and does not incorporate ballistic trajectories nor neutron lifetimes, simplifying assumptions made in this work. Incorporating these factors will lead to a decrease in count rates. To take into account such parameters, a scaling factor ϵ is introduced:

$$\mathcal{N}_\epsilon = \epsilon A_s \Phi_0 = \epsilon \mathcal{A}[1 - \cos(\vartheta_o)]\Phi_0. \tag{3.22}$$

The scaling factor ϵ is determined by comparing the count rates predicted from the model $\mathcal{N}_{model}$ and the *observed* epithermal neutron count rate $\mathcal{N}_{observed}$ of LPNS:

$$\mathcal{N}_{observed}/\mathcal{N}_{model} \equiv \epsilon.$$

Said differently, the scaling factor renormalizes Equation 3.21 using *observed* LPNS count rates; Equation 3.22 is then used to estimate LEND count rates. It is expected that the scaling factors for LPNS and LEND are similar: LPNS and LEND are both neutron spectrometers that used Helium-3 sensors. There are, however, differences in detector efficiencies since LEND and LPNS operate at different pressures. The overall effect is that the LEND sensor is 95% as efficient as LPNS [30].

The LPNS was an uncollimated instrument, but it had a footprint on the Moon defined by geometry (Figure 3.14). The size of the footprint can be specified by the detector height as well as the angle between the vector from the detector to the center of the Moon and the vector from the detector to the edge of the Moon. At

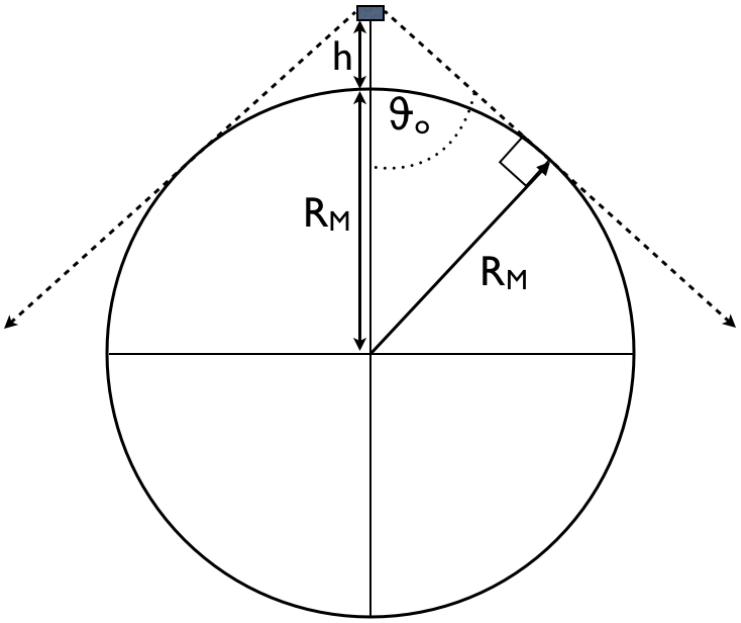

Figure 3.14: Lunar Prospector Footprint Geometry. [The radius of the Moon is $R_M \approx 1737$ km and the LP height above the Moon is $h = 50$ km.]

Table 3.2: LPNS and LEND Parameters Relevant to Sampled Area Calculation [30].

Instrument	LPNS	LEND
$\mathcal{A}$ (cm^2)	114	78.5
ϑ_o $(^\circ)$	76.4	6.2

a 50 km orbit, this angle was

$$\arcsin\left(\frac{R_M}{R_M + h}\right) = \arcsin\left(\frac{1737}{1737 + 50}\right) = 76.4^\circ.$$

The LPNS and LEND parameters relevant to the calculation of sampled area are summarized in Table 3.2.

Using Table 3.2 and Equation 3.21, the LPNS model count rate for epithermal neutrons (Table 3.1, 0% weight fraction of water for epithermal energy range) is

$$\mathcal{N}_{model} = 358\ n\ s^{-1}.$$

However, the observed average count rate of Lunar Prospector, $\mathcal{N}_{observed}$, is 21 counts per second [30]. This gives a scaling factor of

$$\mathcal{N}_{observed}/\mathcal{N}_{model} = \epsilon = 21/358 = 0.059.$$

The LEND neutron count rate is estimated to be

$$\mathcal{N}_{\epsilon} = 0.11\ n\ s^{-1}.$$

The count rate estimates for LPNS and LEND assumed an isotropic angular distribution, the same assumption used in previous chapters. However, it is possible that an angular dependence $\sqrt{\cos(\theta)}$ may be more appropriate [30]. In Appendix C the sampled area for a $\sqrt{\cos(\theta)}$ is derived and used to obtain the following formulas for count rates

$$\mathcal{N}_{model} = \mathcal{A}[1 - \cos(\vartheta_o)^{3/2}]\Phi_0 \tag{3.23}$$

$$\mathcal{N}_{\epsilon} = \epsilon\mathcal{A}[1 - \cos(\vartheta_o)^{3/2}]\Phi_0. \tag{3.24}$$

Table 3.3: LPNS and LEND Count Rate Estimate Comparison [30].

Distribution	Isotropic		$\sqrt{\cos(\theta)}$	
Instrument	LPNS	LEND	LPNS	LEND
$\mathcal{N}_{model}$	358	1.9	415	2.8
$\mathcal{N}_{observed}$	21	-	21	-
ϵ	5.9 %	-	5.1%	-
$\mathcal{N}_{\epsilon}$	-	0.11	-	0.14

In this scenario, the LPNS count rate is 415 counts per second (Equation 3.23)and the scaling factor is $\epsilon = 21/415 = 0.051$. For LEND the estimated count rate is 0.14 counts per second (Equation 3.24). Table 3.3 summarizes the values of the procedure outlined here for isotropic and $\sqrt{\cos(\theta)}$ distributions. In all scenarios the scaling factor was determined using LPNS data and applied to LEND, assuming similar detector performance measures.

These estimates can be compared to other studies (Figure 3.15). One study (Lawrence et al. 2010) used a different scaling procedure and a simulation obtained LEND count rate estimates of 0.15 and 0.18 respectively [30]. In contrast, the LEND team (Mitrofanov et al. 2004) has estimated a number of neutron count rates for dry regolith, obtaining rates of 0.29, 0.32, and 0.9 counts per second [34]. It is unclear what assumptions were made to account for these published values. Overall, the numbers obtained in this work are of the same order of magnitude as previous studies, lending credence to the use of a scaling approach and the method described here of obtaining neutron count rate estimates.

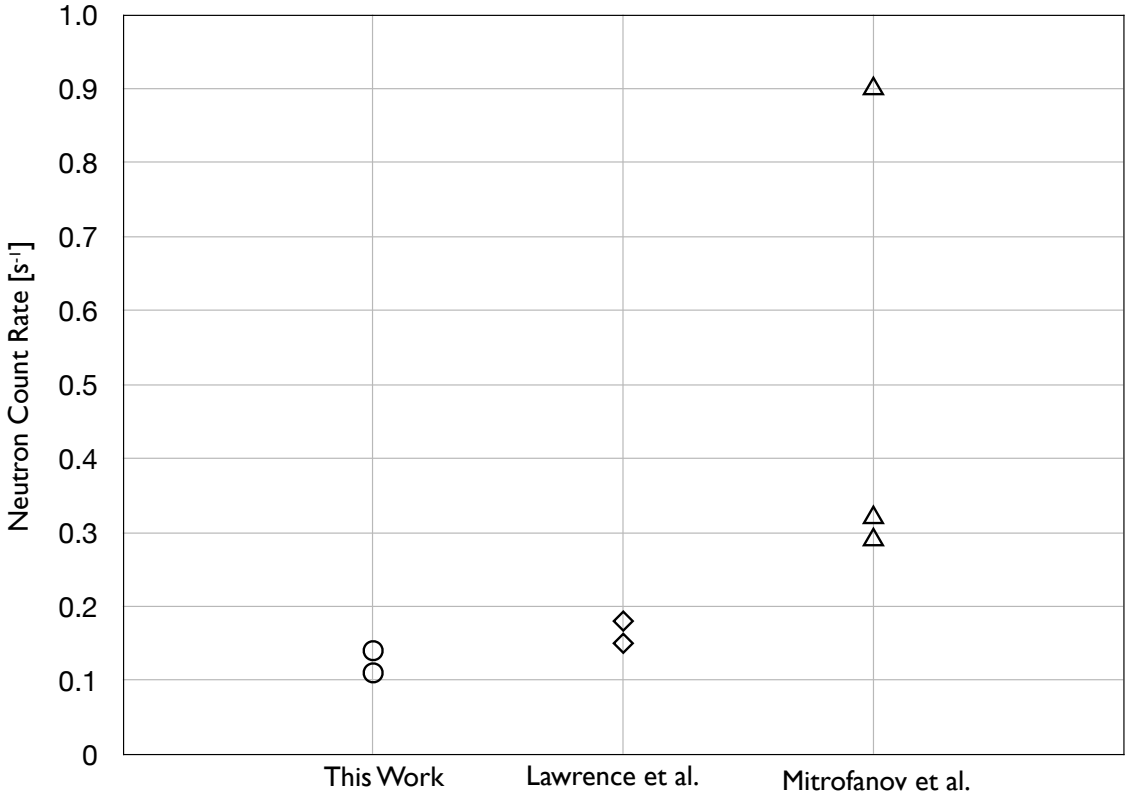

Figure 3.15: LEND Count Rate Estimate Comparison. [In this work the top and lower circles were count rates obtained for a $\sqrt{\cos(\theta)}$ and isotropic distribution respectively. The top and lower diamonds are obtained using a scaling approach and a simulation respectively [30]. The LEND team obtained count rates by numerical estimates (bottom), a simple scaling approach (middle), and a simulation (top) [34].]

3.11 Suggestions for Future Work

The original question "Is it worth the time, effort, and money to put a surface-based neutron spectrometer on the Moon?" needs to be addressed with more rigor. One detector capability that has not been examined here is the ability to distinguish between different water morphologies. Preliminary estimates on this may be done

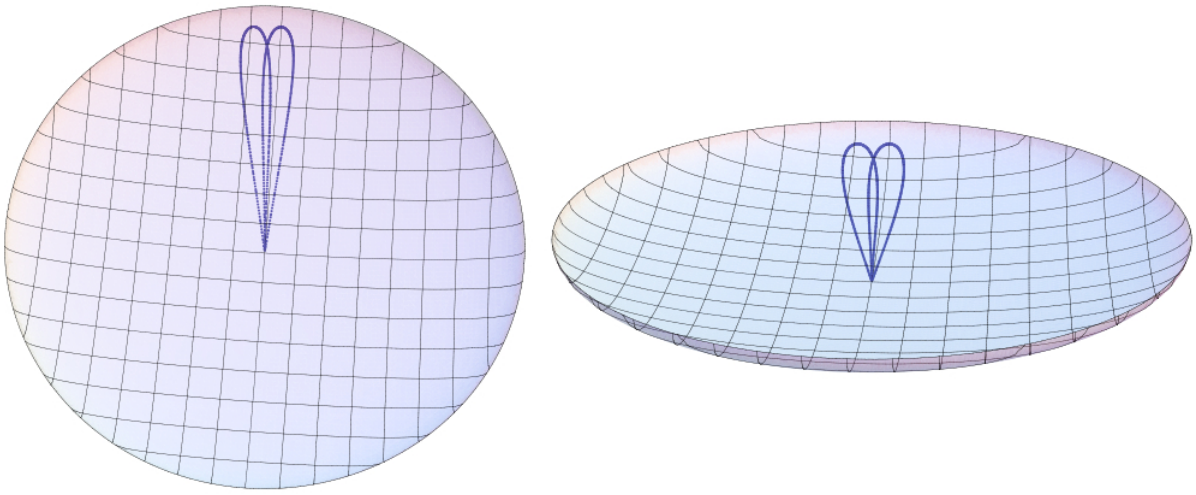

Figure 3.16: Oversampling Crater Regions Using Overlapping Footprints. [The footprint outlines for a detecter located one meter above the crater center with a 5° opening angle is shown. The detector is pointed in direction of $\theta = 150°$ and the footprints are $\phi = 7°$ apart. The two figures are the same scenario, but viewed from different perspectives. Overlapping footrpints may be used to provide constraints on water morphology.]

with the simple model discussed in this thesis. By oversampling footprints, constraints may be placed on water morphologies of overlapping footprint regions (Figure 3.16). For example, if the footprint on the left in Figure 3.16 is associated with large neutron deficit with respect to the region on the right, then the overlapping region of the two footprints is most likely not associated with the neutron deficit. Additional oversampling can further constrain the region associated with the deficit.

A good place to begin further study would involve an investigation of non-homogenous water distributions within a footprint. It would be interesting to see how neutron counts are (or are not) changed in such a scenario. If neutron counts do not change, then it is necessary to see how oversampling the area could provide additional insight.

Additionally, some of the assumptions of the model need to be examined in greater detail in order to verify that the assumptions of the model are reasonable, or to incorporate additional effects. For example, thermal neutrons would not have ray-like trajectories over the typical length scales considered in the crater; rather, they should have ballistic trajectories. Epithermal and Fast neutrons are, however, expected to have ray-like trajectories over typical crater length scales due to their larger energies. The assumption of isotropic neutron emission also needs to be examined since other distributions may be more appropriate [30]. A neutron transport simulation that tracks the angle with which neutrons leave the surface needs to be investigated. It would be interesting to see if the angular distribution is affected by different elemental abundances in the regolith. Quantifying the impact of these simplifying assumptions is essential for determing the kind of information provided by the model.

Once the assumptions of the model are verified or modified to incorporate a more realistic detection scenario, it should be possible to determine whether or not it is viable to place a neutron spectrometer on the Moon. This would involve comparing the scientific information potential of a surface based spectrometer to its orbital counterpart. If it is deemed viable, then a more detailed model should be examined. This new model should take into account detector geometries and efficiencies, as well as the entire detection process. Realistic crater geometries should also be considered.

CHAPTER 4

CONCLUSIONS

4.1 Recapitulation of Motivation

Mankind's understanding of the Moon is incomplete. There are still many investigations that need to be undertaken and knowledge of lunar water distribution is paramount. The first evidence of water on the Moon came from the *Clementine* mission. From theoretical studies of lunar water retention it was known at the time that if there were regions on the Moon that were sufficiently cold, then the possibility for water existed. *Clementine* found evidence for PSRs on the Moon's surface and data indicative of lunar water presence based on an experiment with radio waves.

The *Clementine* mission was just the beginning of the search for lunar water. Several more missions, using complementary techniques, followed. Perhaps the most important of these was the *Lunar Prospector* mission, which used neutron spectroscopy to infer hydrogen abundances and deficits over the entire Moon.

Changes in neutron counts are indicative of hydrogen abundances or deficits since neutrons are greatly moderated by hydrogen present in the regolith. Although other elements may also contribute to moderation, none affect neutron counts more

than hydrogen. Also, since water contains hydrogen, its abundances may be associated with water abundances.

Over the lunar poles, where there are many regions that are in permanent shadow, a drop in neutron counts was detected by *Lunar Prospector*. After further investigation, it was concluded that the primary contributor to the drop could be lunar water.

The success of orbital neutron spectroscopy in mapping the elemental composition of the Moon gave fruition to the topic of this thesis: surface-based neutron spectroscopy. A model has been created to begin examining the detector performance. The model takes into account simple crater geometries and some universal parameters of collimated neutron spectrometers. It uses a simulated neutron flux spectra for different weight fractions of water to estimate neutron count rates and a likelihood method to determine the statistical significance of the count rates. Furthermore, estimates of the amount of time to meet a statistical significance threshold with or without background were made.

4.2 Model Summary

Since a surface-based neutron spectrometer would most likely operate in (or close to) a region with permanent shadow, a geometric model that describes the gross features of such places was needed. PSRs are normally associated with craters; thus, the lunar environment geometry was chosen to be that of a crater. The crater was modeled as a generic ellipsoid, where the depth, length, and width of the ellipsoid

could be modified. The ellipsoid was compared to a typical lunar crater in order to justify this approach (Section 2.2).

It was also necessary to isolate the key features of collimated neutron spectrometers. Detectors normally have complicated geometries and efficiencies that make each one unique, but they have certain parameters in common. Two such parameters are aperture area and opening angle. These were the only detector parameters taken into account. For simplicity, the aperture was assumed to be circular.

The detector was was not omni-directional and assumed to be collimated. Therefore the FoV of the detector needed to be taken into account. A circular aperture has the consequence that the FoV takes the form of a cone whose width is determined by the opening angle.

The FoV defined the observable surface area on the crater known as the footprint. This quantity is critical because it provides localization information on the detected neutrons. In other words, it provided a measure of the spatial resolution.

To calculate the shape and geometric area of the footprint, the intersection of the FoV with the crater needed to be known. The expression for the outline of this surface was obtained by rotating and translating a cone that was originally pointed upward to the appropriate location and direction on the crater. The footprint was shown for several different pointing directions and two different opening angles to illustrate the complicated geometry of the footprint. Also, the geometric area of the footprint was approximately calculated for different pointing directions to provide a better understanding of possible spatial resolutions for different detector configura-

tions. Interestingly, the geometric area did not depend very strongly on the pointing direction. However, the opening angle drastically changed the spatial resolution.

A neutron count estimate for a detector was obtained by first considering the probability that an emitted neutron lies on an appropriate trajectory to the aperture. The neutrons were assumed to have ray-like trajectories to make the analysis tenable. Furthermore, they were assumed to emit from the surface isotropically. An expression for the far field limit of the probability was obtained by analogy with a two-dimensional case and was shown to be in agreement with the exact expression (in the far field limit). An important feature of the far field probability was its direct proportionality to the aperture area.

The distribution of water in the footprint was assumed to be homogeneous so that a quantity called sampled area could be defined (Section 2.10). This parameter was useful in separating the dependence of neutron counts on water content. Sampled area, when multiplied by flux, gave an estimate on the neutron counts per unit time seen by a detector. It may also be thought of as the average probability over the footprint multiplied by the area. An order-of-magnitude estimate of sampled area was calculated by considering the relatively simple scenario of a detector pointing downward to a flat surface. This was done to have a notion of what kind of numbers to expect for sampled area.

For different detector opening angles and pointing directions, the sampled area was calculated. In contrast to the geometric area, there was a strong dependence on the pointing direction. Unsurprisingly, when footprints came closer to where the detector was located, the sampled area increased. The opening angle also had a

strong effect on the sampled area. An increase in the opening angle increased the sampled area. This was expected since larger opening angles corresponded to a larger observable area.

Using sampled area, it was possible to obtain neutron count estimates, but not all detections are equal and a way to estimate the statistical significance of a measurement was needed. To this end, a likelihood method was employed. Since the goal of a mission with a surface-based neutron spectrometer would be to find any amount of water, the crater was assumed to be dry and a detection was deemed significant if it deviated from this assumption by an amount specified by the likelihood criteria. There were two threshold criteria used to reject the null hypothesis: a 99% threshold and 99.9999% threshold. These values were chosen because they roughly corresponded to a 3σ and 5σ measurement.

The neutron flux spectra for various lunar soils had already been calculated. For this work, ferroan anorthosite was used to estimate expected fluxes for epithermal, low-epithermal, and thermal neutrons on the Moon for varying water content. Dry regolith (0% by weight fraction of water) was assumed to be the null hypothesis; thus, for a given detection scenario, the number of expected neutrons for dry regolith was compared to the neutron counts for different weight fractions of water. The calculations were performed by (at least initially) neglecting background. A deviation from the null hypothesis was quantified by using the likelihood criteria. The confidence with which the null hypothesis could be rejected was defined by the threshold criteria. The minimum amount of time it takes to reject the null hypothesis based on the relevant threshold was used to define a dwell time for the detector.

Background was included in the analysis since it is not expected that a spectrometer will detect neutrons coming only from its field of view. This parameter was introduced as a new independent variable defined with respect to the null hypothesis. Treating it as an independent parameter allowed an investigation of background effects on statistical significance and dwell time. Background had the effect of increasing the amount of time it takes to make a significant detection.

Detector performance for two configurations was considered. One was modeled after a grazing incidence neutron spectrometer and the other was chosen for comparison. The grazing incidence spectrometer turned out to be an unreasonable detector for attempting to localize water in the entire crater due to the amount of time it would take. In contrast, a detector that utilized the entire epithermal range and had a larger opening angle took a reasonable amount of time.

The model was also used to estimate neutron count rates for LEND. A scaling factor was determined using *LP* neutron spectrometry data as a starting point. Applying the model of the thesis along with the scaling factor lead to an estimate of LEND count rates similiar to previous studies.

4.3 A Basis for Future Work

An investigation that should be undertaken would involve considering a non-homogeneous distribution of water. It would be interesting to see if oversampling could provide constraints on the morphology of water. Also, a more detailed simulation should be performed which takes into account detector efficiencies and ballistic trajectories for neutrons. If it can be shown that a surface-based neutron spectrom-

eter would greatly increase our current knowledge of the distribution of elements on the Moon, then a spectrometer should be built and placed there.

The importance of the work presented in this study is that it provides a basis for future investigations: considerations that must be made and ideas that can be used. It is meant to both orient and provide information for future developments.

APPENDICES

APPENDIX A

ROTATION MATRIX

The rotation operator O may be represented as a matrix R with respect to a particular basis (e.g., the crater coordinate system). Figure A.1 shows the effect of the operator on a vector originally directed along the x_3 axis.

In order to derive the rotation matrix R a secondary basis is introduced with the following relation to the original $\{\hat{x}_1, \hat{x}_2, \hat{x}_2\}$ crater coordinate basis

$$\hat{e}_1 = \hat{x}_3 \tag{A.1}$$

$$\hat{e}_2 = \cos(\phi_d)\,\hat{x}_1 + \sin(\phi_d)\,\hat{x}_2 \tag{A.2}$$

$$\hat{e}_3 = -\sin(\phi_d)\,\hat{x}_1 + \cos(\phi_d)\,\hat{x}_2. \tag{A.3}$$

The basis $\{\hat{e}_1, \hat{e}_2, \hat{e}_3\}$ constitutes an orthonormal right-handed basis. That is,

$$\hat{e}_i \cdot \hat{e}_j = \delta_{ij} \text{ and } \epsilon_{ijk}\hat{e}_j\hat{e}_k = \hat{e}_i,$$

where δ_{ij} is the Kronecker delta and ϵ_{ijk} is the permutation tensor. This is a convenient choice because the rotation operator in this basis may be represented as the

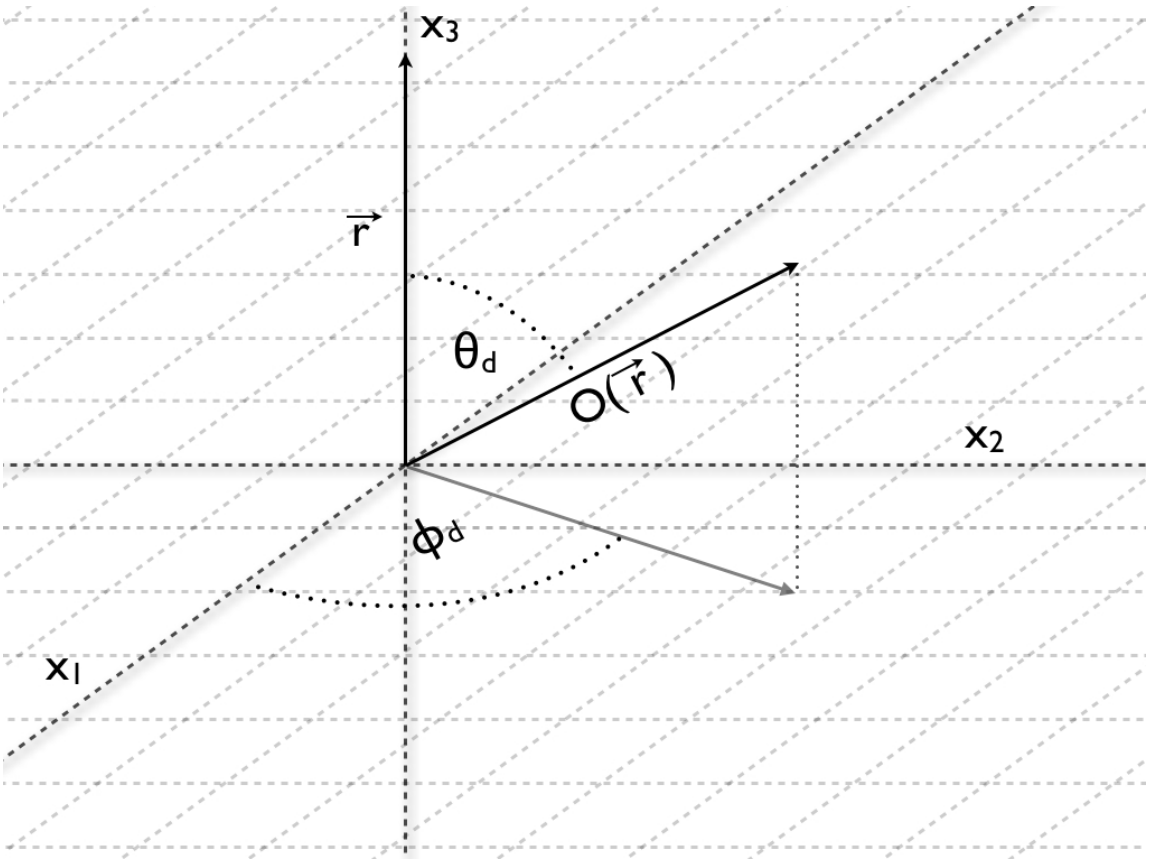

Figure A.1: Rotation Operator. [The above figure illustrates the effect of using the rotation operator O on a vector $\vec{r}$ that originally pointed along the x_3 axis.]

matrix

$$R_e = \begin{bmatrix} \cos(\theta_d) & \sin(\theta_d) & 0 \\ -\sin(\theta_d) & \cos(\theta_d) & 0 \\ 0 & 0 & 1 \end{bmatrix}. \tag{A.4}$$

In order to convert the operator into its representation in the $\{\hat{x}_1, \hat{x}_2, \hat{x}_2\}$ basis, the matrix that relates the two bases

$$\begin{bmatrix} \hat{e}_1 \\ \hat{e}_2 \\ \hat{e}_3 \end{bmatrix} = M \begin{bmatrix} \hat{x}_1 \\ \hat{x}_2 \\ \hat{x}_3 \end{bmatrix} \Longrightarrow M = \begin{bmatrix} 0 & 0 & 1 \\ \cos(\phi_d) & \sin(\phi_d) & 0 \\ -\sin(\phi_d) & \cos(\phi_d) & 0 \end{bmatrix} \tag{A.5}$$

must be used [32]. Using M allows R to be written in terms of R_e by the following transformation

$$R = M^T R_e M. \tag{A.6}$$

After carrying through the multiplication, the matrix

$$\begin{bmatrix} \cos^2(\phi_d)\cos(\theta_d) + \sin^2(\phi_d) & \cos(\phi_d)\sin(\phi_d)[\cos(\theta_d) - 1] & \cos(\phi_d)\sin(\theta_d) \\ \cos(\phi_d)\sin(\phi_d)[\cos(\theta_d) - 1] & \sin^2(\phi_d)\cos(\theta_d) + \cos^2(\phi_d) & \sin(\phi_d)\sin(\theta_d) \\ -\cos(\phi_d)\sin(\theta_d) & -\sin(\phi_d)\sin(\theta_d) & \cos(\theta_d) \end{bmatrix}$$

is obtained.

APPENDIX B

SOLID ANGLE

The problem of determining the probability that a particle is on an appropriate trajectory toward the aperture amounts to determining the solid angle of a cone. The shape of the cone is defined by the particle emission point and the outer edge of a circular aperture. To describe the geometry, some notation is introduced in Table B.1. Also, the geometry for the setup and parameters are displayed in Figure B.1, Figure B.2, Figure B.3, and Figure B.4.

The goal is to determine the limits of integration for the solid angle

$$\Omega = \iint \sin(\theta)\ \mathrm{d}\theta\,\mathrm{d}\phi.$$

To derive the proper limits there are two situations that must be considered. The first case is one where the particle is emitted directly beneath the aperture ($d \leq R$) and the other is the complementary scenario ($d > R$). These will be given the names "Scenario 1" and "Scenario 2" respectively. The reason for this division is more apparent if the geometry in Figure B.3 is examined. In Scenario 1 the azimuthal angle may span its full range (0 to 2π), whereas in Scenario 2, this angle is more

Table B.1: Table of Variables

Parameters	Symbol
Distance from aperture center to particle emission point on the x-y plane.	d
Distance from particle emission point on the x-y plane to aperture edge.	s
Aperture height	h
Detector Radius	R
Azimuthal Angle with respect to particle emission point.	ϕ
Polar with respect to the normal particle of the emission plane.	θ
The vector from the detector center to the particle emission point.	$\vec{r}$
Detector pointing direction.	$\vec{n}$
Angle between $\vec{r}$ and $\vec{n}$	φ

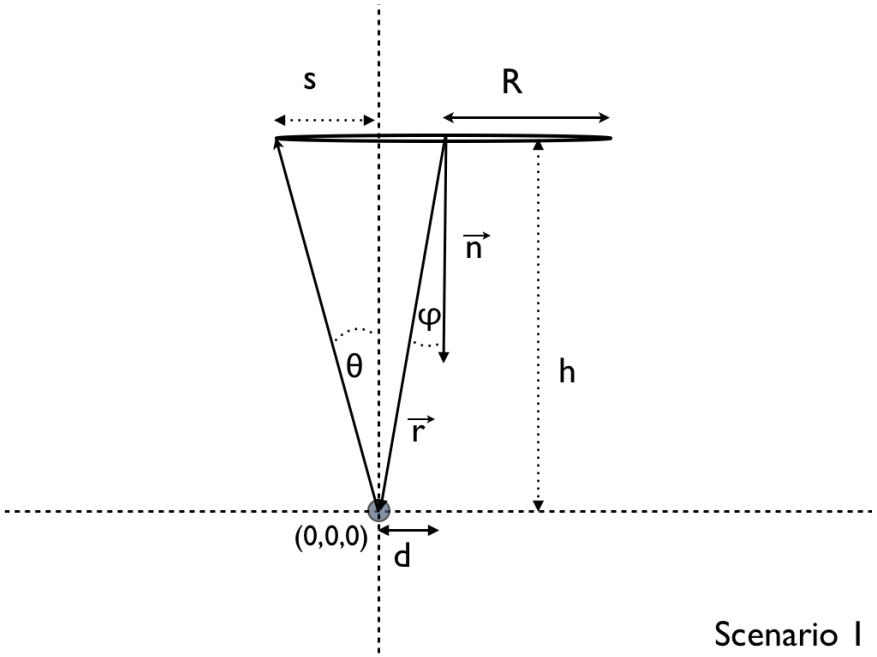

Figure B.1: Side Geometry of Scenario 1.

limited. Furthermore, the limits of integration for the polar angle are also different for the two scenarios, as shown in Figure B.1 and Figure B.2.

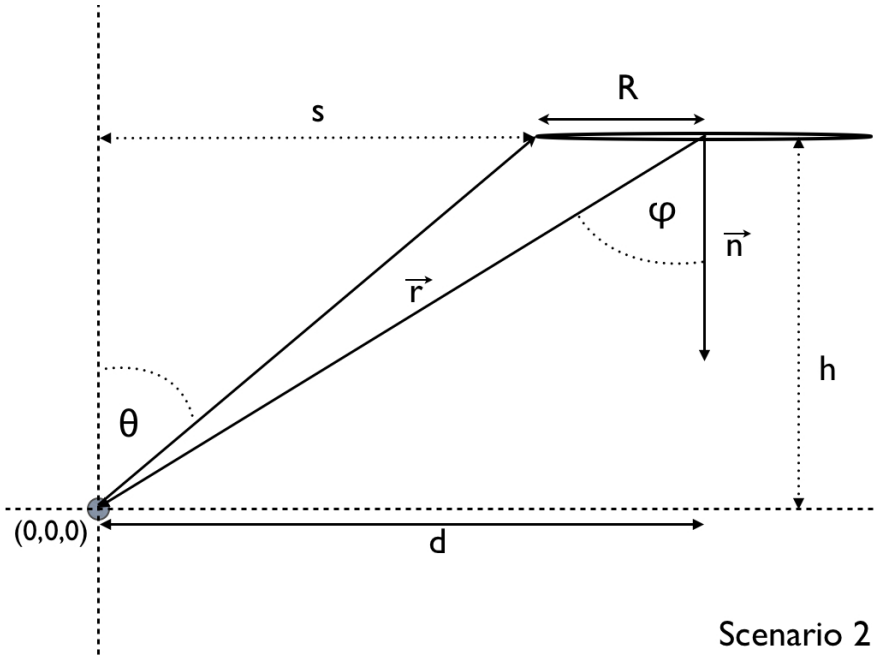

Figure B.2: Side Geometry of Scenario 2.

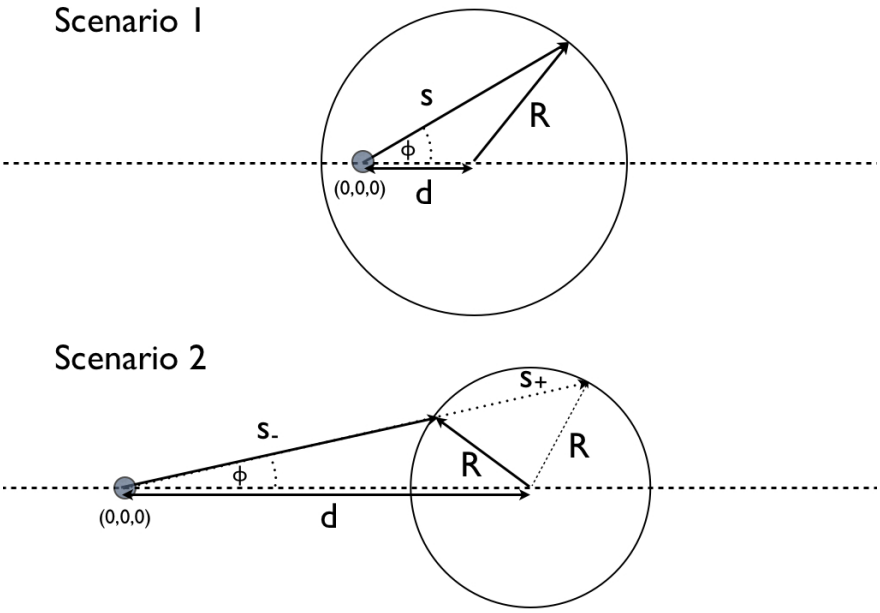

Figure B.3: XY Projection of Solid Angle Geometry.

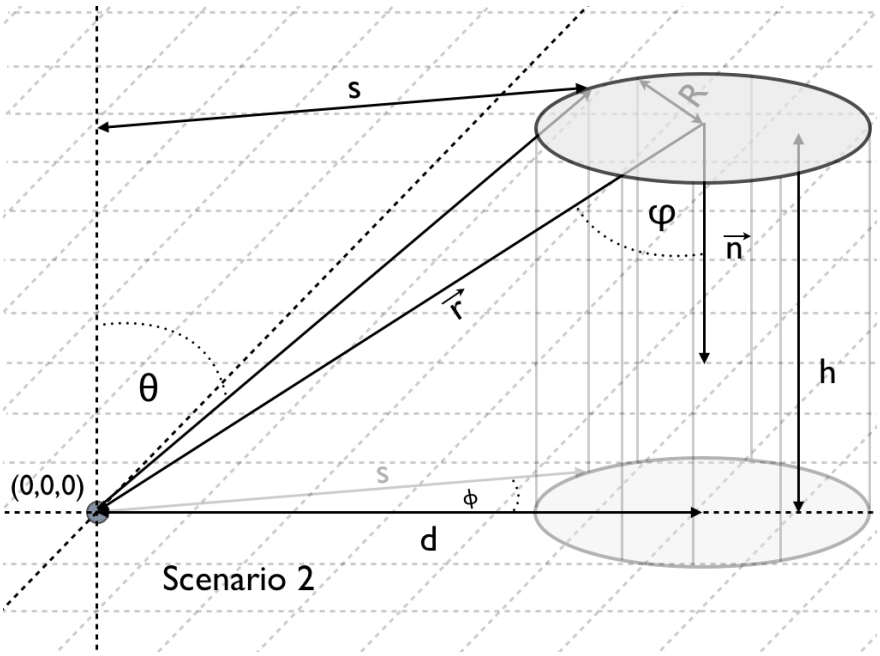

Figure B.4: Three-Dimensional Solid Angle Geometry.

Since ϕ is chosen as the outer integration variable, the limits of integration for θ will, in general, have a dependence on the ϕ variable. Determining the relationship between these variables is equivalent to finding s as a function of ϕ, since

$$\theta = \arctan\left(\frac{s}{h}\right). \tag{B.1}$$

For Scenario 1, by examining Figure B.1, the law of cosines and the quadratic formula[1] may be used to arrive at

$$s = d\cos(\phi) + \sqrt{R^2 - d^2\sin^2(\phi)}. \tag{B.2}$$

[1]The quadratic formula yields two answers but only the one that corresponds to the positive sign is relevant.

For notational convenience let

$$\theta_1(\phi) = \arctan\left(\frac{s}{h}\right), \tag{B.3}$$

where s is defined by Equation B.2. Thus the integral for the solid angle for Scenario 1 is

$$\int_0^{2\pi}\int_0^{\theta_1(\phi)} \sin(\theta)\, \mathrm{d}\theta\, \mathrm{d}\phi. \tag{B.4}$$

For Scenario 2, a similar procedure may be performed. The end result gives two values for s, namely,

$$s_\pm = d\cos(\phi) \pm \sqrt{R^2 - d^2\sin^2(\phi)}. \tag{B.5}$$

The minus sign corresponds to the first time s intersects the aperture edge while the positive sign corresponds to the latter intersection. This is shown in Figure B.3. The two values of s define the limits of integration for θ. Letting

$$\theta_2(\phi) = \arctan\left(\frac{s_-}{h}\right) \tag{B.6}$$

and

$$\theta_3(\phi) = \arctan\left(\frac{s_+}{h}\right), \tag{B.7}$$

where s_- and s_+ are defined by Equation B.5, defines the proper limits.

The azimuthal angle must also be determined by geometry. By examining Figure B.3, it may be seen that the range of the azimuthal coordinate does not

extend from 0 to 2π. The maximum angles that ϕ can obtain would correspond to when the discriminant in Equation B.5 is set equal to zero. Letting ϕ_1 denote the largest possible value for ϕ the relation is

$$\phi_1 = \arcsin\left(\frac{R}{d}\right). \tag{B.8}$$

By symmetry the lowest value for ϕ is $-\phi_1$. Thus the integral for the solid angle for Situation 2 is

$$\int_{-\phi_1}^{\phi_1}\int_{\theta_3(\phi)}^{\theta_2(\phi)} \sin(\theta)\ \mathrm{d}\theta\,\mathrm{d}\phi. \tag{B.9}$$

Finally, everything may be put together to define the solid angle Ω as a function of h,d, and R

$$\Omega(h,d,R) = \begin{cases} \int_0^{2\pi}\int_0^{\theta_1(\phi)} \sin(\theta)\ \mathrm{d}\theta\,\mathrm{d}\phi & \text{for } d \le R \\ \int_{-\phi_1}^{\phi_1}\int_{\theta_3(\phi)}^{\theta_2(\phi)} \sin(\theta)\ \mathrm{d}\theta\,\mathrm{d}\phi & \text{for } d > R \end{cases}. \tag{B.10}$$

The probability of "detection" P for a particle emitted from the point defined by h and d would be the solid angle Ω divided by 2π:

$$P = \begin{cases} \frac{1}{2\pi}\int_0^{2\pi}\int_0^{\theta_1(\phi)} \sin(\theta)\ \mathrm{d}\theta\,\mathrm{d}\phi & \text{for } d < R \\ \frac{1}{2\pi}\int_{-\phi_1}^{\phi_1}\int_{\theta_3(\phi)}^{\theta_2(\phi)} \sin(\theta)\ \mathrm{d}\theta\,\mathrm{d}\phi & \text{for } d \ge R \end{cases}. \tag{B.11}$$

APPENDIX C

NON-ISOTROPIC DISTRIBUTION

If the angular distribution of neutrons emitted from the Moon is not isotropic, then the formula for the geometric probability must be modified. Following the approach outlined in Appendix B, Equation B.11 must be modified to include the angular distribution $f(\theta, \phi)$ and its normalization:

$$P = \frac{1}{Z} \iint f(\theta, \phi) \sin(\theta) \, \mathrm{d}\theta \, \mathrm{d}\phi, \tag{C.1}$$

where Z is the normalization constant obtained by integrating over the emission hemisphere,

$$Z \equiv \int_0^{2\pi} \int_0^{\pi/2} f(\theta, \phi) \sin(\theta) \, \mathrm{d}\theta \, \mathrm{d}\phi. \tag{C.2}$$

A simple estimate may be performed on Equation C.1 if the distance between the detector and neutron emission point is much larger than the radius of the detector. Furthermore, the assumption that the angular distribution does not depend on the azimuthal angle ϕ will be made. With these premises, the angular distribution is approximately constant over the limits of integration. In this case the probability

becomes

$$P = \frac{f(\theta_0)}{Z} \iint \sin(\theta)\ \mathrm{d}\theta\, \mathrm{d}\phi, \tag{C.3}$$

where θ_0 is evaluated in the direction of the detector and defined with respect to the surface normal. Specifically, the angle θ_0 is the angle between the surface normal vector and the vector from the neutron emission point to the aperture center. The latter vector is equivalent to the $\vec{r}$ vector in Section 2.9 but in the opposite direction.

The asymptotic expression for geometric probability (Equation 2.22) is generalized to include the non-isotropic distribution and becomes

$$P \approx f(\theta_0) \frac{\mathcal{A}\cos(\varphi)}{Z|\vec{r}|^2}. \tag{C.4}$$

It is possible that lunar neutrons have a $f(\theta) = \sqrt{\cos(\theta)}$ dependence [30]. If so, the sampled area throughout this work needs to be adjusted. In particular, the scenario considered in Section 2.11 is easily modified to consider the effects of an $f(\theta) = \sqrt{\cos(\theta)}$ angular distribution. Equation 2.25 becomes

$$A_s = \int_0^{2\pi} \int_0^{h\tan(\vartheta_o)} \frac{3\mathcal{A}h}{4\pi\left(s^2+h^2\right)^{3/2}} \frac{h^{1/2}}{\left(s^2+h^2\right)^{1/4}} s\, \mathrm{d}s\, \mathrm{d}\phi, \tag{C.5}$$

where $f(\theta_0) = h^{1/2}/(s^2+h^2)^{1/4}$ and the normalization is $Z = \frac{4\pi}{3}$. Equation C.5 evaluates to

$$A_s = \mathcal{A}\left[1 - \cos\left(\vartheta_o\right)^{3/2}\right]. \tag{C.6}$$

This sampled area is used to obtain count rate estimates for LPNS and LEND in Section 3.10, under the assumption that the $\sqrt{\cos(\theta)}$ angular distribution is appropriate.

REFERENCES

[1] K. Watson, B.C. Murray, and H. Brown. The Behavior of Volatiles on the Lunar Surface. *Journal of Geophysical Research*, pages 3033–3045, 1961.

[2] J. R. Arnold. Ice in the Lunar Poles. *Journal of Geophysical Review*, pages 5659–5668, 1979.

[3] `http://www.diviner.ucla.edu/blog/?p=123`.

[4] C.R. Neal. The Moon 35 Years After Apollo: What's Left to Learn. *Science Direct*, 2008.

[5] R.E. Lingenfelter, E.H. Canfield, and W.N. Hess. The Lunar Neutron Flux. *Journal of Geophysical Research*, pages 2665–2671, 1961.

[6] C.M. Pieters, J.N. Goswami, R. N. Clark, M. Annadurai, J. Boardman, B.Buratti, J. P. Combe, M. D. Dyar, R. Green, G. W. Head, C. Hibbitts, M. Hicks, P. Isaacson, R. Klima, G. Kramer, S. Kumar, E. Livo, S. Lundeen, E. Malaret, T. McCord, J. Mustard, J. Nettles, N. Petro, C. Runyon, M. Staid, J. Sunshine, L. A. Taylor, S. Tompkins, and P. Varanasi. Character and Spatial Distribution of OH/H2O on the Surface of the Moon Seen by M3 on Chandrayaan-1. *Science*, pages 568–572, 2009.

[7] W.C. Feldman, S. Maurice, A. B. Binder, B.L. Barraclough, R. C. Elphic, and D. J. Lawrence. Fluxes of Fast and Epithermal Neutrons from Lunar Prospector: Evidence for Water Ice at the Lunar Poles. *Science*, pages 1496–1500, 1998.

[8] W.C. Feldman, D.J. Lawrence, R.C. Elphic, D.T. Vaniman, D.R. Thomsen, B.L. Barraclough, S. Maurice, and A.B. Binder. Chemical Information Content of Lunar Thermal and Epithermal Neutrons. *Journal of Geophysical Research*, pages 20347–20363, 2000.

[9] O. Gasnault, W.C. Feldman, S. Maurice, I. Genetay, C. d'Uston, T. H. Prettyman, and K. R. Moore. Composition from Fast Neutrons: Application to the Moon. *Geophysical Research Letters*, pages 3797–3800, 2001.

[10] R. G. Sachs. *Nuclear Theory*. Addison-Wesley, first edition, 1953.

[11] E. Segre. *Nuclei and Particles: An Introduction to Nuclear and Subnuclear Physics*. Benjamin-Cummings, second edition, 1977.

[12] O. Gasnault, C. d'Uston, W.C. Feldman, and S. Maurice. Lunar Fast Neutron Leakage Flux Calculation and its Elemental Abundance Dependece. *Journal of Geophysical Research*, pages 4263–4271, 2000.

[13] D. J. Lawrence, W. C. Feldman, R. C. Elphic, J. J. Hagerty, S. Maurice, G. W. McKinney, and T. H. Prettyman. Improved Modeling of Lunar Prospector Neutron Spectrometer Data: Implications for Hydrogen Deposits at the Lunar Poles. *Journal of Geophysical Research*, pages 20,347–20,363, 2006.

[14] G. F. Knoll. *Radiation Detection and Measurement*. John Wiley and Sons, third edition, 2000.

[15] Optical Society of America. *Handbook of Optics*, volume 5. McGraw-Hill Professional, third edition, 2009.

[16] W. C. Feldman, B. L. Barraclough, S. Maurice, R. C. Elphic, D. J. Lawrence, D. R. Thomsen, and A. B. Binder. Major Composition Units of the Moon: Lunar Propsector Thermal and Fast Neutrons. *Science*, pages 1489–1493, 1998.

[17] S. Nozette, C.L. Lichtenberg, P. Spudis, R. Bonner, W. Ort, E. Malaret, M. Robinson, and E. M. Shomaker. The Clementine Bistatic Radar Experiment. *Science*, pages 1495–1498, 1996.

[18] S. J. Ostro and E. M. Shoemaker. The Extraordinary Radar Echoes from Europa, Ganymede, and Callisto: A Geological Perspective. *Icarus*, pages 335–345, 1990.

[19] R. A. Simpson and G.L. Tyler. Reanalysis of Clementine Bistatic Radar Data from the Lunar South Pole. *Journal of Geophysical Research*, pages 3845–3862, 1999.

[20] S. Maurice, D. J. Lawrence, W. C. Feldman, R. C. Elphic, and O. Gasnault. Reduction of Neutron Data from Lunar Prospector. *Journal of Geophysical Research*, 2004.

[21] `http://lunar.arc.nasa.gov/results/neutron.htm`.

[22] W.C. Feldman, B.L. Barraclough, K.R. Fuller, D.J. Lawrence, S. Maurice, M.C. Miller, T.H. Prettyman, and A.B. Binder. The Lunar Prospector Gamma-Ray and Neutron Spectrometers. *Nuclear Instruments and Methods in Physics Research*, pages 562–566, 1999.

[23] I. Genetay, S. Maurice, W.C. Feldman, O. Gasnault, D.J. Lawrence, R.C. Elphic, C. d'Uston, and A.B. Binder. Elemental Content from 0 to 500 keV Neutrons: Lunar Prospector Results. *Planetary and Space Science*, pages 271–280, 2003.

[24] W. C. Feldman, S. Maurice, D. J. Lawrence, R. C. Little, S. L. Lawson, O. Gausnault, R.C. Wiens, B.L. Barraclough, R.C. Elphic, T. H. Prettyman, J.T. Steinberg, and A.B. Binder. Evidence for Water Ice Near the Lunar Poles. *Journal of Geophysical Research*, pages 23,231–23,251, 2001.

[25] http://m3.jpl.nasa.gov/instrument.html.

[26] D. J. Lawrence, D. M. Hurley, W. C. Feldman, R. C. Elphic, S. Maurice, R. S. Miller, and T. H. Prettyman. Sensitivity of Orbital Neutron Measurements to the Thickness and Abundance of Surficial Lunar Water. *Journal of Geophysical Research*, 2011.

[27] A. Colaprete, P. Schultz, J. Heldmann, D. Wooden, M. Shirley, K. Ennico, B. Hermalyn, W. Marshall, A. Ricco, R. C. Elphic, D. Goldstein, D. Summy, G. D. Bart, E. Asphaug, D. Korycansky, D. Landis, and L. Sollitt. Detection of Water in the LCROSS Ejecta Plume. *Science*, pages 463–468, 2010.

[28] P. H. Schultz, B. Hermalyn, A. Colaprete, K. Ennico, M. Shirley, and W. S. Marshall. The LCROSS Cratering Experiment. *Science*, pages 468–472, 2010.

[29] http://lunar.gsfc.nasa.gov/lend.html.

[30] D. J. Lawrence, R. C. Elphic, W. C. Feldman, H. O. Funsten, and T. H. Prettyman. Performance of Orbital Neutron Instruments for Spatially Resolved Hydrogen Measurements of Airless Planetary Bodies. *Astrobiology*, pages 183–200, 2009.

[31] I.G. Mitrofanov, A. B. Sanin, W. V. Boynton, G. Chin, J. B. Garvin, D. Golovin, L. G. Evans, K. Harshman, A. S. Kozyrev, M.L. Litvak, A. Malakhov, E. Mazaric, T. McClanahan, G. Milikh, M. Mokrousov, G. Nandikotkur, G. A. Neumann, I. Nuzhdin, R. Sagdeev, V. Shevchenko, V. Shvetsov, D.E. Smith, R. Starr, V.I. Tratyakov, J. Trombka, D. Usikov, A. Varenikov, A. Vostrukhin, and M. T. Zuber. Hydrogen Mapping of the Lunar South Pole Using the LRO Neutron Detector Experiment LEND. *Science*, pages 483–486, 2010.

[32] G. Arfken and H. Weber. *Mathematical Methods for Physicists*. Academic Press, sixth edition, 2005.

[33] H. de Boer, K. Bennet, H. Bloemen, J.W. den Herder, W. Hermsen, A. Klumper, G. Lichti, M. McConnell, J. Ryan, V. Schonfelder, A. W. Strong, and C. de Vries. Maximum Likelihood Method Applied to Comptel Source Recognition and Analysis. In *Data Analysis in Astronomy IV*. Plenum Press, 1992.

[34] I.G. Mitrofanov, A.B. Sanin, D.V. Golovin, M.L. Litvak, A.A. Konovalov, A.S. Kozyrev, A.V. Malakhov, M.I. Mokrousov, V.I. Tretyakov, V.S. Troshin, V.N. Uvarov, A.B. Varenikov, A.A. Vostrukhin, V.V. Shevchenko, V.N. Shvetsov, A.R. Krylov, G.N. Timoshenko, Y.I. Bobrovnitsky, T.M. Tomilina, A.S. Grebennikov, L.L. Kazakov, R.Z. Sagdeev, G.N. Milikh, A. Bartels, G. Chin, S. Floyd, J. Garvin, J. Keller, T. McClanahan, J. Trombka, W. Boynton, K. Harshman, R. Starr, and L. Evans. Experiment LEND of the NASA Lunar Reconnaissance Orbiter for High-Resolution Mapping of Neutron Emission of the Moon. *Astrobiology*, pages 793–804, 2004.